RF MEMS AND INTEGRATED MANUFACTURING FOR MINIATURIZED MILLIMETER-WAVE SYSTEMS

by

YING CAI

Presented to the Faculty of the Graduate School of

The University of Texas at Arlington in Partial Fulfillment

of the Requirements

for the Degree of

DOCTOR OF PHILOSOPHY

THE UNIVERSITY OF TEXAS AT ARLINGTON

August 2006

ACKNOWLEDGEMENTS

First of all, I would like to express my great acknowledgement to Dr. Jung-Chih Chiao for his invaluable direction, advice, and support. Without his expert-guidance, I could not finish this work. I would especially appreciate him for sharing his industry and academic experiences with me, which make me have a clear idea of how to build my own career after I graduate. Personally I not only take him as an advisor in academy, but also a friend, a great person in life.

This dissertation is dedicated to my parents and my wife for their endless love and support. I would like to thank my brother and sister-in-law. I always keep in mind of their dedication to the family when I pursue my degree overseas.

I would like to show my appreciation to Dr. Liwei Lin, Dr. Y.-C. Su, Dr. Firas Sammoura, and Dr. Yiin-Kuen Fuh at the University of California at Berkeley. They are colleagues of mine on this NSF supported project. And I'd like to thank Dr. Chen-Yu Chi from Agilent Technologies for his help on the measurement of the fabricated devices.

I would like to extend my appreciation to Dr. Ronald L. Carter, Dr. Alan W. Davis, Dr. Jonathan Bredow, Dr. Mingyu Lu, Dr. Weidong Zhou, Dr. Donald Butler, Dr. Zeynep Celik-Butler, Dr. Nasir Basit, Dr. Jeongsik Sin, and Jim Florence for their advice and assistance.

At last, I am especially grateful to my colleagues. They are Huijun Li, Jianqun Wang, Ping Zhang, Suraj K. Patil, Thermpon A. Ativanichayaphong, Po-Sheng Hu, Smitha M. N. Rao, Praveen P. S. Rao, Dr. Kevin Le, Lun-Chen Hsu, Naresh Dhaubanjar, Wen-Ding Huang, Varkey George, and Alan Wei.

This research is supported by NSF, Grant # DMI – 0428884.

July 20, 2006

ABSTRACT

RF MEMS AND INTEGRATED MANUFACTURING FOR MINIATURIZED MILLIMETER-WAVE SYSTEMS

Publication No. _____

Ying Cai, PhD.

The University of Texas at Arlington, 2006

Supervising Professor: Jung-Chih Chiao

Recently millimeter-wave systems have attracted more attentions in applications owing to their short wavelengths, high resolutions, broad bandwidths and high environmental tolerance. However, the great challenges of high fabrication and assembly costs, bulky volume, and heavy weight of millimeter-wave systems call for new integrated manufacturing techniques and novel architectures. The micro hot embossing technique integrated with other microfabrication techniques could address these challenges. In this dissertation, the micro plastic hot embossing technique was presented for the fabrication of miniaturized millimeter-wave systems. The micro hot embossing on plastic materials demonstrated its advantages on significant costs, volume, and weight reduction, while maintaining high performances.

A W-band rectangular waveguide and a W-band iris waveguide filter with integrated plastic flanges using micro hot embossing and selective electroplating have been designed, fabricated and characterized. A horn antenna with a waveguide feed has been fabricated and tested. These prototype devices show a promise for applications in millimeter-wave systems.

RF MEMS devices utilized in millimeter-wave systems can greatly improve system performance. A new multi-step actuator structure for RF MEMS was proposed in this work. Wider capacitance tuning range and higher capacitor ratio were achieved in this structure. With multiple actuation electrodes on steps, discrete levels of capacitances with tunable analog ranges, instead of binary states in the conventional structures, have been achieved. Multi-step structure design, fabrication issues and results have been investigated. The multi-step actuators were further utilized to design distributed MEMS transmission line phase shifters. Multi-level discrete varactors shorten the length of transmission lines and thus reduce insertion losses, while achieving more phase shifts.

Finally, direct and hybrid means are implemented to integrate RF MEMS devices with micro plastic hot embossed components. A three-physical-layer architecture is presented in this work to integrate antenna parts, transmission lines, RF MEMS devices, active components, and other off-chip devices in a millimeter-wave system. BCB (Benzocyclobutene) as a substrate and structure material, and the transition from a CPW (coplanar waveguide) to a waveguide play key roles in the 3-physical-layer structure for integration.

TABLE OF CONTENTS

LIST OF ILLUSTRATIONS

LIST OF TABLES

CHAPTER 1

INTRODUCTION

1.1 Motivations and Objectives

1.1.1 Millimeter-Wave Systems: Advantages and Challenges

The term millimeter-wave refers to alternative current signal with a frequency between 30 GHz and 300 GHz and a corresponding electrical wavelength on the order of millimeters. Compared to radio frequency (300 MHz - 3 GHz) and microwave (3-30 GHz) signals, millimeter-wave signals have shorter wavelengths. Device dimensions are usually directly related to the signal wavelengths; therefore shorter wavelength enables compact sizes and small dimensions of devices. Shorter wavelengths might give the system higher resolution as well. This characteristic has been utilized in many high-resolution imaging systems. Millimeter-waves give broader bandwidths, which is important to broadband communication systems.

Although optical systems have shorter wavelengths, millimeter-waves have the unique spectral characteristics in the atmosphere, affecting the propagation of electromagnetic waves above 10 GHz. Millimeter-waves have the advantages of being able to penetrate smoke, fog, dust, and light rain. Owing to the high environmental tolerance, millimeter-wave systems can provide many sensing functionalities for all-

weather applications, such as automobile crash avoidance systems, airplane radars, astronomy, weather monitoring and soil/moisture sensing [1.1, 1.2].

Although nowadays millimeter-wave systems have attracted much interest, they are facing several challenges. The challenge comes from the high fabrication and assembly costs. Because of the short wavelengths of millimeter-waves, millimeter-wave components are small and compact. They usually require high precision machining. Second, millimeter-wave systems are difficult to be integratively manufactured. The millimeter-wave components have to be fabricated individually before being manually assembled together with other components. This is a time consuming and costly process. Millimeter-wave systems are usually bulky due to the complex connections. They are also heavy, which hampers their further applications such as on portable instruments and satellite applications.

For instance, a single millimeter-wave front-end unit could take up to more than 20 percents of the costs in a defense satellite; and steerable radars that could see through fog, cloud, and dust are too large and heavy to implement in airplanes or automobiles.

1.1.2 Motivations and Objectives

Nowadays, millimeter-wave systems have been facing challenges of bulky volume, heavy weight, and expensive costs. Microstrip structures, coplanar waveguides and printed circuit components had been considered to solve parts of these challenges. However, their high losses at high frequencies hindered their further practical applications.

Recently, micromachining processes have been employed to make components for millimeter-wave systems. Katehi *et al.* demonstrated a transition structure that couples a finite ground coplanar transmission line to a W-band bulk micromachined diamond-shaped silicon waveguide [1.3]. Wallace *et al.* analyzed an octagonal bulk micromachined silicon horn antenna integrated with rectangular waveguide that was fabricated using thick photoresist (SU-8). The antenna operating at 585 GHz had a Gaussian coupling efficiency of 92.5% and low side lobe levels that agreed with the theoretical model [1.4]. Harris *et al.* fabricated a W-band waveguide and horn antenna system using V-grooves formed by using wet etching of a (100) silicon substrate. The wafers were metallized with evaporated gold to form metallic walls. The structures fabricated in two-halves were assembled and tested for radiation patterns at 75 GHz and 94 GHz. Measurement shows good-agreement with FEM simulations [1.5]. Davies *et al.* fabricated and characterized an air filled waveguide. The S-parameters of the waveguide were measured for a frequency sweep of 75-110 GHz and an insertion loss as low as 0.2 dB per wavelength was measured [1.6]. LeDuc *et al.* integrated a Superconductor-Insulator-Superconductor (SIS) tunnel junctions mounted on a nitride membrane with a bulk micromachined rectangular waveguide fabricated using wet etching of a (100)-silicon wafer. Electroless nickel was used to selectively metallize the walls of the waveguides and keep the nitride membrane isolated. The waveguide was tested for a frequency range of 170-260 GHz and a 0.8 dB per wavelength insertion loss was measured, which is comparable to commercially available conventional waveguides [1.7]. Although these micromachined millimeter-wave components have

been successfully demonstrated, they were individual components, and were difficult to integrate with the other parts of the system. However, these recent and on-going efforts indicate the importance of integrated manufacturing for millimeter-wave systems.

All these previously mentioned challenges call for new integration fabrication techniques. Hence, the wide applications and profound technology impacts of millimeter-wave systems are the first motivation of this dissertation. Meanwhile, to overcome the challenges millimeter-wave system facing is the second motivation. In this dissertation, efforts have been made to solve the challenges and implement the following three objectives.

1.1.2.1 Objective I: to Develop a New Manufacturing Process

The first objective of this dissertation is to develop a low-cost, high-productive manufacturing process based on micro plastic hot embossing and selective electroplating for miniaturized, integrated front-end for millimeter-wave systems.

Hot embossing is widely used in conventional machining for its advantages of reproducing products quickly and massively, hence cheaply. Nowadays, the micro hot embossing technique has been attracted a lot of attentions in micro device fabrication owing to its advantages of flexibility, low-cost, high aspect ratios, and time efficiency. The key advantage of this process as compared to other processes, such as stereo-lithography, laser micromachining, and wet etching is that this approach is better suited for millimeter-wave systems, such as antenna, waveguides, and coaxial transmission lines.

1.1.2.2 Objective II: to Develop Novel RF MEMS Components

The RF MEMS (radio frequency microelectromechanical systems) has seen a great growth in the past decades, owing to its advantages of low power consumption, high isolation, high linearity and low losses. RF MEMS can greatly improve the performance of RF/microwave/millimeter-wave systems. Currently RF MEMS are aiming to be widely used in commercial and defense applications.

In this dissertation, the second objective is to develop a novel RF MEMS structure, which will be implemented for RF MEMS phase shifters in a millimeter-wave system, competing to the widely used conventional structure.

1.1.2.3 Objective III: to Develop an Integrated Architecture

The third objective of this dissertation is to develop an integrated architecture for millimeter-wave systems combining plastic micro hot embossed components, RF MEMS devices, and other individual devices together for imaging, sensing, and communication applications. This architecture will help to develop integrated manufacturing for system integration. The dramatic difference as compared to a traditional system is that the batch process can greatly reduce the manufacturing costs and implement the miniaturization of the system.

1.2 Chapters in This Dissertation

This dissertation consists of 5 chapters. Chapter 1 introduces the great development and advanced applications of millimeter-wave systems. The profound impact of millimeter-wave systems is presented. The challenges of the millimeter-wave

system are discussed. Finally, this chapter gives the objectives and motivations of the dissertation.

Chapter 2, Micro Hot Embossed Plastic Millimeter-Wave Devices, describes the low-cost, high productive, front-end manufacturing process based on micro plastic hot embossing and selective electroplating. First, the design and fabrication flow of micro plastic hot embossing is discussed. Following the process, a plastic micro hot embossed W-band rectangular waveguide is presented as an example of using micro hot embossing and selective electroplating to fabricate millimeter-wave devices. Besides waveguides, a W-band iris waveguide filter is fabricated as well to demonstrate the feasibility of using micro hot embossing to fabricate more complex structures other than rectangular waveguides. Finally, a horn antenna with a waveguide feed is presented, which expends the 2-dimentional fabrication capability of micro hot embossing to 3-dimentional manufacturing and integration.

Chapter 3, A Novel RF MEMS Structure and Its Applications, describes the novel multi-step actuator structure, its design, work mechanism, and fabrication. The high power handling characteristic is presented competing with other structures. At last, the application of this novel structure in a distributed MEMS transmission line phase shifter is proposed in this chapter.

Chapter 4, Integrated RF MEMS and Plastic Micro Hot Embossed Devices, and Chapter 5, Future Work, cover the effort to implement the integration of the micro hot embossed component, RF MEMS devices, and other devices. Two integration mechanisms are dressed. One is to directly integrate RF MEMS with the plastic micro

hot embossed devices. As an example, a W-band tunable iris waveguide filter prototype is designed, fabricated, and characterized. A MEMS bilayer cantilever actuator is designed and fabricated, which is proposed to be installed in an iris waveguide filter to obtain desired band shifting. Another way to integrate RF MEMS devices with micro hot embossed components and other off-chip devices is to utilize a three-physical-layer architecture. Benzocyclobutene (BCB) as a good substrate material, and the transition from a CPW to a waveguide are utilized in this 3-physical-layer architecture to integrate the antenna layer (micro hot embossed devices), transmission line layer (transmission lines and RF MEMS devices), and circuit layer (circuit, active components, and off-chip devices) together.

CHAPTER 2

MICRO HOT EMBOSSED PLASTIC MILLIMETER-WAVE DEVICES

Millimeter-wave systems are widely used in commercial and defense applications. However, their high manufacturing cost, bulky size, and heavy weight become the challenges. Micro hot embossing on plastic materials with selective electroplating technique provides a low cost and compact approach to these problems as one possible solution. In this chapter, several micro hot embossed plastic devices are demonstrated.

2.1 Micro Plastic Hot Embossing

Hot embossing, as one of the replication technologies, has been widely used in industry for many years for its advantages of reproducing products quickly and massively, hence, cheaply. Recently hot embossing has attracted a lot of attentions in applications besides conventional machining due to its advantages of flexibility, low costs, high aspect ratios, and time efficiency. Currently, the emerging applications mainly focus on micro reactors [2.1], micro fluidic systems [2.2] (mixers), micro optical devices [2.3] (optical waveguide, switches), and biochips [2.4]. In these applications, the devices have characteristic dimensions in the submicrons to hundreds of microns range. Micro hot embossing techniques are sufficiently flexible to achieve such a wide range of tolerance. In this dissertation, extension of using the hot embossing technique

in the range of hundreds of microns to millimeters for high-frequency electromagnetic-wave components has been demonstrated on plastic materials.

A wide variety of polymer materials can be used in hot embossing. They provide flexibility for process design, environmental requirement specifications and RF performance considerations. With selective electroplating to make electrical parts, the integrated platform offers light weights compared to the conventional brass platform. Moreover, most of the polymer materials provide low dielectric constants and high resistivity at high frequencies [2.5], which makes interconnects and down-conversion integration on the same substrate easier.

Micro hot embossing on plastic material demonstrates its advantages on greatly cutting down the costs, volume and weight, while retaining high performance. Building the micro hot embossed front-end system includes electrical and mechanical designs and fabrications. A standard W-band rectangular waveguide is chosen to demonstrate the electrical and mechanical design and fabrication.

A standard W-band rectangular (WR-10) waveguide is defined with an opening of 2.54 mm by 1.27 mm. Although determining the single-mode waveguide dimensions is straightforward, special considerations have to be taken into account with some particular requirements in hot embossing. For instance, in a conventional ridge waveguide, the sidewalls of the ridge are vertical. However, for the convenience of easy de-embossing, a small angle is designed in the sidewalls. In the electrical design, the effects by the sidewall tilt angle on performance have to be carefully checked and compensated.

The mechanical design first is carried out with making the embossing molds. The mold shape is basically complementary to the desired device shape with machining tolerance and thermal effect considerations. Comparing the designed dimensions to the replica dimensions, the mold is fined-tuned to meet the requirements. For the fabrication process, first, upper and lower aluminum molds are manufactured by traditional mechanical machining such as EDM (electro discharge machining). The mold's dimensions are in millimeter scale yet the tolerances require micron-scale accuracy. For higher frequency applications, the device critical dimensions become smaller. The molds might need to be fabricated by bulk micromachining on silicon.

The hot embossing process begins with heating the aluminum molds and plastic substrate to 160˚C. Uniformly distributed forces are applied on both the upper and lower molds. After the complementary structures are transferred from the molds to the plastic substrate, the plastic replica is retrieved by cooling both the molds and the plastic substrate. Then the plastic replica could be easily detached from the molds. Next, a thin composite layer of 200 Å/6000 Å Cr/Pt is sputtered as the seed layer for the electroplating on both the plastic substrate and a prepared silicon cover. The silicon cover is clamped on top of the plastic substrate to form a closed cavity for the rectangular waveguide. Two flange adaptors are separately fabricated using the same hot embossing process. On the flanges, screw threads and pinholes are drilled at the precise locations, which make the flanges compatible commercial W-band rectangular waveguides. The clamped combination of plastic substrate and silicon cover is fitted into the flanges and glued by epoxy. The surfaces of the flanges and waveguide are

planarized by lapping with silicon carbide paper. Finally, the whole device is immersed into a gold electroplating solution to deposit an 8-μm thick gold layer.

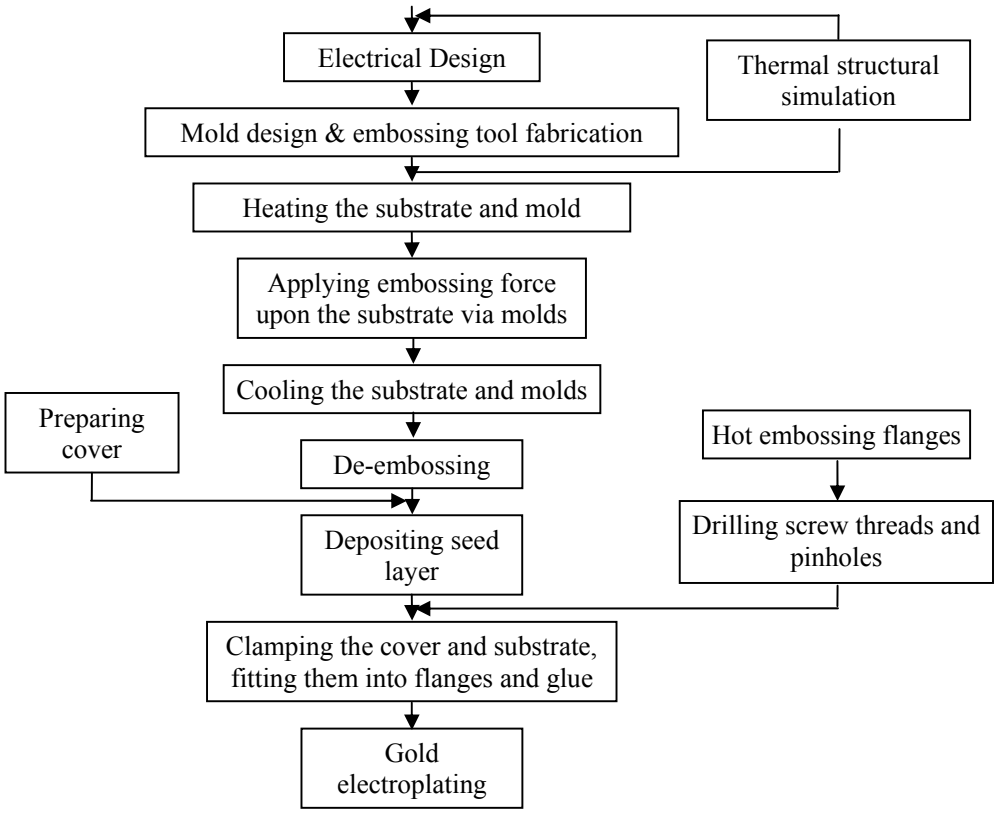

Figure 2.1 Design and fabrication flow of micro plastic hot embossing.

Figure 2.1 illustrates the design and fabrication flow of micro hot embossing millimeter-wave devices. In various applications, the processes would need some minor changes.

For instance, in order to fabricate a rectangular waveguide, only one plastic part is hot embossed. But in some cases, two plastic pieces might be hot embossed separately. These two parts will be aligned and bonded together to form some complex

structures. With this approach, the fabrication capability of micro plastic hot embossing is extended. However, the main steps follow the same process.

In the following sections, different millimeter-wave devices are designed and fabricated. These include a waveguide, a waveguide filter, and a horn antenna, which are designed and fabricated with the mentioned design and fabrication flow.

2.2 Rectangular Waveguide

Rectangular waveguides are typical transmission lines used in microwave and millimeter-wave applications. The advantages of the rectangular waveguides include wide bandwidths of operation for single-mode transmission, low attenuation, and good mode stability for the fundamental mode of propagation. Even though these days a lot of microwave circuits are fabricated using planar transmission lines such as microstrip lines and coplanar waveguides, rectangular waveguides are still required in many applications for their low losses and high power handling capability.

2.2.1 Manufacturing of Rectangular Waveguide

Rectangular waveguides have a very simple structure. It has rectangular cross section all along the wave path. A large variety of microwave components can be designed in rectangular waveguides, such as resonators, couplers, detectors, isolators, attenuators, phase shifters, and filters. These devices are traditionally manufactured by precision machining and electro-forming techniques. However, these techniques are difficult, time consuming, and costly. People have done a lot of work and tried to fabricate light weight and low cost rectangular waveguides for easy integration and high-volume production. However, they only partially solved the challenges.

Tai *et al*. fabricated a WR-10 waveguide by using bulk micromachining of a silicon wafer with (110) surface orientation and polyimide bonding [2.6]. The fabrication process is briefly described in Figure 2.2. Many other works followed the same idea.

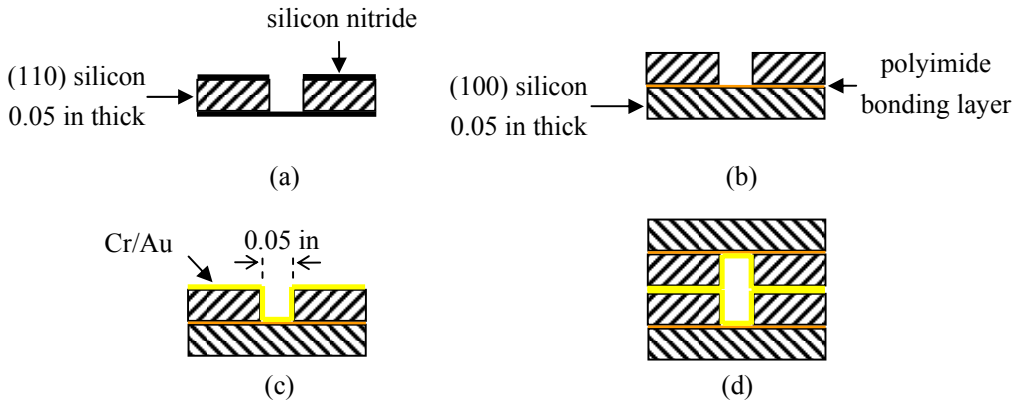

Figure 2.2 Cross-section view of the fabrication process in [2.6]. (a) A silicon wafer is completely etched through. (b) Etched wafer is bonded to an un-etched wafer by polyimide to form a half-closed cavity. (c) Gold plating on the completed half-section waveguide walls. (d) Bonding two completed half-sections to form a whole rectangular waveguide.

Davies *et al*. have demonstrated a surface micromachined reduced-height air-filled rectangular waveguide for 70-110 GHz [2.7]. In the fabrication of reduced-height waveguide, a thick photoresist layer (about 100 μm) is used as the sacrificial layer to define the hollow cavity of the waveguide. Compared to the original size of a standard W-band rectangular waveguide (2.54 mm x 1.27 mm), this micromachined waveguide has a greatly reduced height.

Harriss *et al.* have presented the results of the fabrication of finned diamond-shaped waveguides and horn antennas by EDP (ethylene-diamene-pyrocatechol) anisotropic etching of (100) silicon wafers [2.8]. Because of the anisotropic wet etching

characteristic of EDP on silicon wafers as shown in Figure 2.3, the cross section of manufactured waveguide is not a rectangle but a diamond shape. Therefore, a special jib is fabricated and provides a transition from standard rectangular waveguide to this diamond-shaped waveguide.

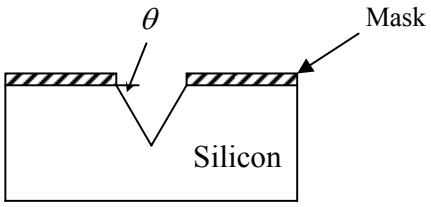

Figure 2.3 A V-shaped groove fabricated by KOH or EDP wet etching on a (100) silicon wafer.

Katehi *et al*. have fabricated and measured low-loss diamond-shape micromachined waveguides, which were developed in (001)-oriented silicon wafers through anisotropic wet etching of 25 wt.% tetramethyl ammonium hydroxide (TMAH) at 80°C [2.9].

In this dissertation, a new technique using micro hot embossing on plastic material has been developed, which takes the low loss advantage of metallic cavity waveguide yet overcomes its demerits of high costs and heavy weight.

2.2.2 Micro Hot Embossed Plastic Waveguide

The cut-off frequency of a hollow metallic, air-filled rectangular waveguide could be found as [2.10]:

$$f_{c,mn} = \frac{1}{2\sqrt{\mu_0 \varepsilon_0}} \sqrt{\left(\frac{m}{a}\right)^2 + \left(\frac{n}{b}\right)^2} \tag{2-1}$$

where $f_{c,mn}$ is the cutoff frequency, μ_0 and ε_0 are the permeability and permittivity of the free space, respectively, a is the width of the rectangular waveguide, b is the height of the waveguide, and m, n are integer numbers for the propagating modes. The desired fundamental mode in a rectangular waveguide is the transverse electric TE_{10} mode (m=1 and n=0). It is desirable to have the operating frequency higher by 60% than the cutoff frequency of the mode and lower by 25% of the cut-on frequency of the next mode. For 95 GHz systems, the design conditions are:

$$1.6 f_{c,10} = 95 \text{ GHz and } 0.8 f_{c,10} = 95 \text{ GHz} \tag{2-2}$$

and the dimensions of a W-band waveguide become 2.54 mm x 1.27 mm (WR-10 rectangular waveguide).

To manufacture such dimensions of a part for conventional millimeter-wave systems, the fabrication process of the waveguide and flanges is typically done by precision machining on a metallic block followed by brazing a metallic cover to enclose a waveguide.

Figure 2.4 shows the main fabrication processes of hot embossing. An aluminum mold (insert) is first manufactured by traditional mechanical machining. The hot embossing process begins with heating the aluminum mold and plastic substrate to 160˚C. Uniformly distributed forces are applied on both the mold and plastic piece as shown in Figure 2.4 (a). After the complementary structure is transferred from mold to the plastic piece, the plastic replica is retrieved by cooling the mold and plastic substrate and detaching the molds as shown in Figure 2.4 (b). Next, in Figure 2.4 (c), a layer of 200 Å/6000 Å Cr/Pt is sputtered as the seed layer for the following gold electroplating

on both the plastic substrate and a prepared silicon cover. Figure 2.4 (d) illustrates that the prepared silicon cover is clamped on top of the plastic replica to form a closed cavity for the rectangular waveguide.

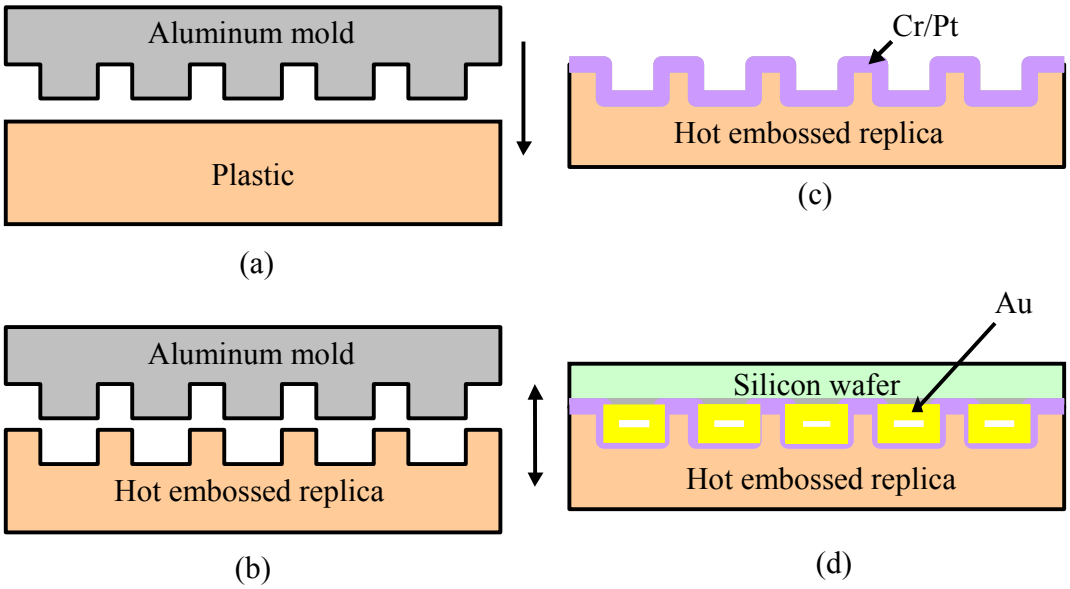

Figure 2.4 Fabrication process of a rectangular waveguide. (a) Hot embossing of the plastic part by applying uniformly distributed force. (b) Detaching the mold and retrieving the hot embossed plastic replica. (c) Sputtering 200 Å/6000 Å Cr/Pt as the seed layer. (d) Waveguide is formed by adding a silicon wafer cover.

Two flange adaptors are separately fabricated using the same hot embossing process. On the flanges, screw threads and pinholes are drilled at the precise locations, which make the flanges able to connect to any commercial standard W-band rectangular waveguide (shown in Figure 2.5). The clamped combination of plastic substrate and silicon cover is fitted into the flanges and glued by epoxy. The surfaces of the flanges and waveguide are planarized by lapping with silicon carbide paper. Finally, the whole device is immersed into a gold electroplating solution to deposit an 8-μm thick gold layer.

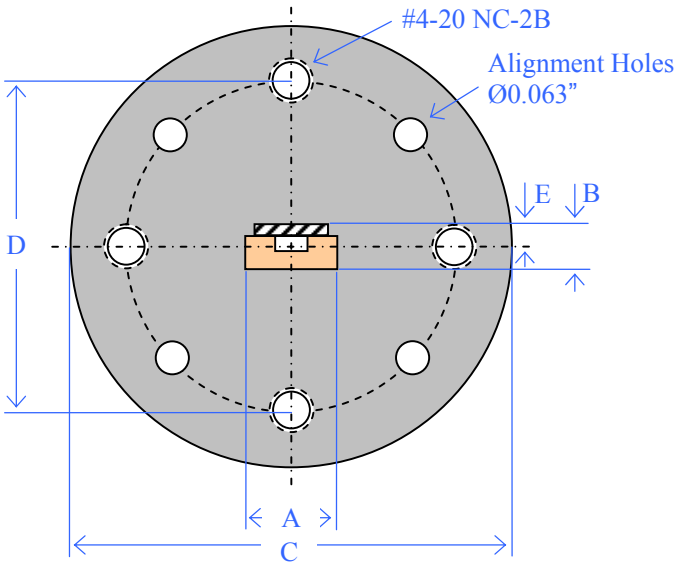

Figure 2.5 A schematic drawing of the flange which the hot embossed plastic replica and silicon cover are fitted and glued to. The dimensions A, B, C, D, and E are 10mm, 3mm, 19.1mm, 14.3mm, and 1.15mm, respectively.

Figure 2.6 and Figure 2.7 show the fabricated results. Figure 2.6 is a SEM photo of the lower left corner of the rectangular waveguide. The height of the opening is around 1.27 mm. Figure 2.7 is a SEM photo of a close view of the lower right corner of the rectangular waveguide. Both Figure 2.6 and Figure 2.7 illustrated that the selective electroplating process [2.11] metallically bonds and seals the waveguide well. The electroplated gold layer is smooth with an estimated average surface roughness of 1350 Å and which could be enhanced by improving the electroplating process.

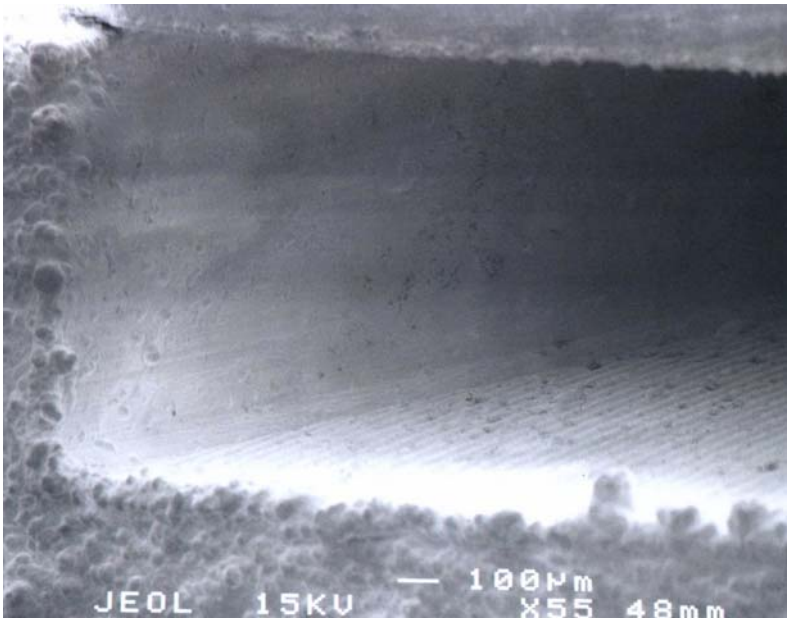

Figure 2.6 SEM photo of the lower left corner of the rectangular waveguide.

Figure 2.7 SEM photo of a close view of the lower right corner of the rectangular waveguide.

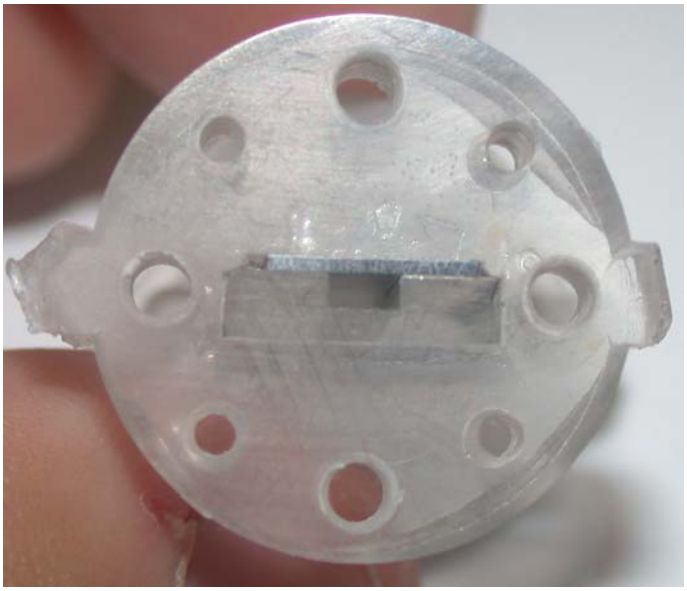

Figure 2.8 A photograph showing the close up view of the waveguide with an integrated flange adaptor.

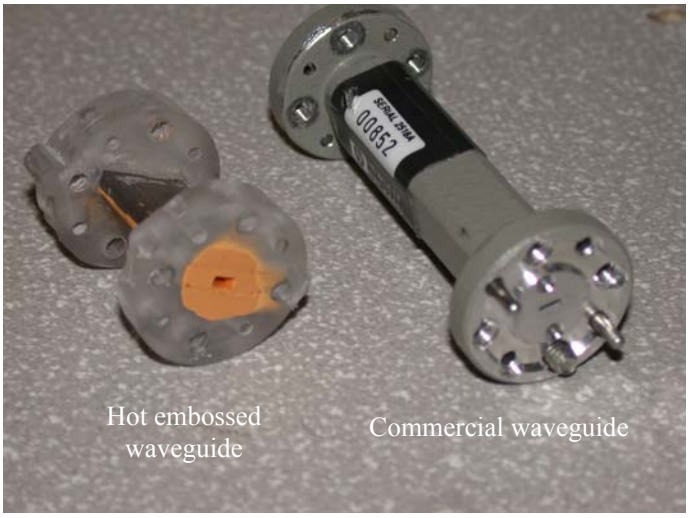

Figure 2.9 The fabricated waveguide (whole component is 2.54 cm in length) and an *Agilent* standard W-band waveguide.

A standard W-band rectangular waveguide has an opening of 2.54 mm by 1.27 mm. The tolerance of a standard WR-10 waveguide is ±0.03 mm. For the tested

waveguide, the width and height of the waveguide are 2.515 mm and 1.295 mm respectively. The variances are -0.025 mm and 0.025 mm, which fall within the acceptable tolerance.

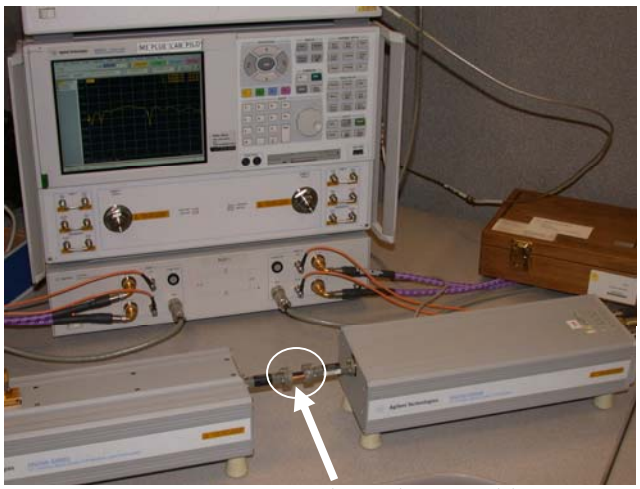

Figure 2.10 A photograph of the measurement setup. An *Agilent* PNA 5250 is used to measure the S-parameters of the hot embossed rectangular waveguide.

Figure 2.10 shows the measurement setup of the micro plastic hot embossed W-band rectangular waveguide. And Figure 2.11 and Figure 2.12 show the measured frequency domain and time domain data derived from the S-parameters respectively. The scattering parameters of the waveguide are measured from 75 GHz to 110 GHz, which covers the whole W-band. The insertion loss varies between -1.79 dB at 75 GHz to -1.06 dB at 110 GHz. And at 95 GHz, the loss is -1.35 dB. The standing wave pattern in the return loss data is due to the mismatch between the DUT (device under test) ports and the connectors.

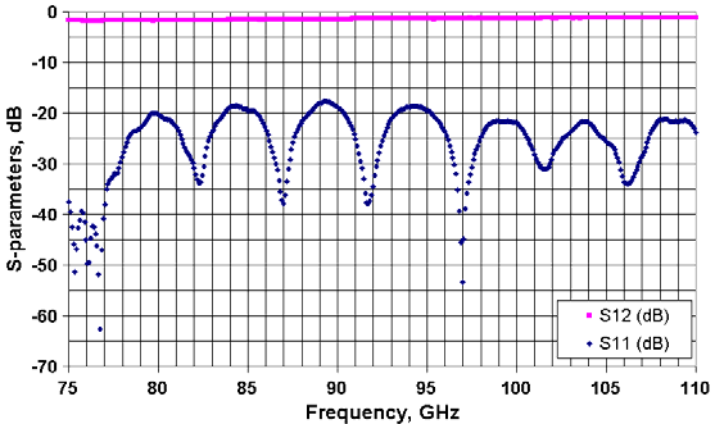

Figure 2.11 Measured S-parameters. The return loss is better than -17.7 dB across the entire W-band with the majority of the band better than -20 dB.

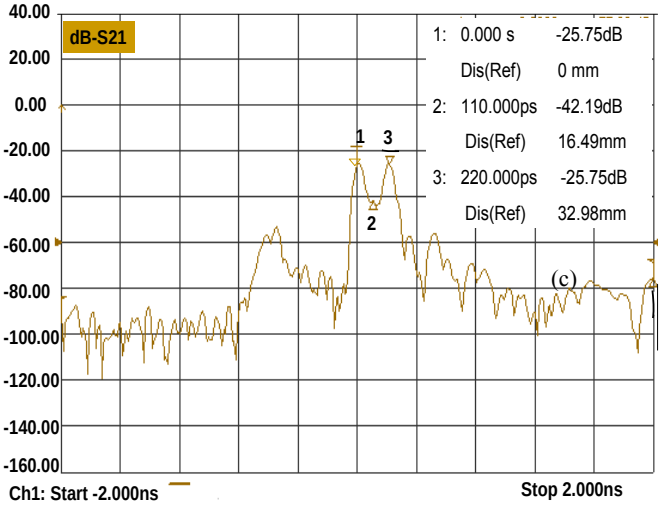

Figure 2.12 A time domain plot shows that the reflections are mainly produced at the interfaces between the DUT and the network analyzer adaptors.

In Figure 2.12, the time domain data show how the reflection varies with respect to time. At marker 1, the waves enter port1 of the waveguide at 0 sec. Then waves are transmitted along the waveguide. At port2, the other end of the waveguide, some waves are reflected back to the port1 at 110 ps. After almost the same period of time, the reflected waves arrive at the original port, which is highlighted as the marker 3 in the

figure. This shows that the reflections are mainly at the interfaces between the waveguide and the network analyzer's adaptors; instead of inside the waveguide.

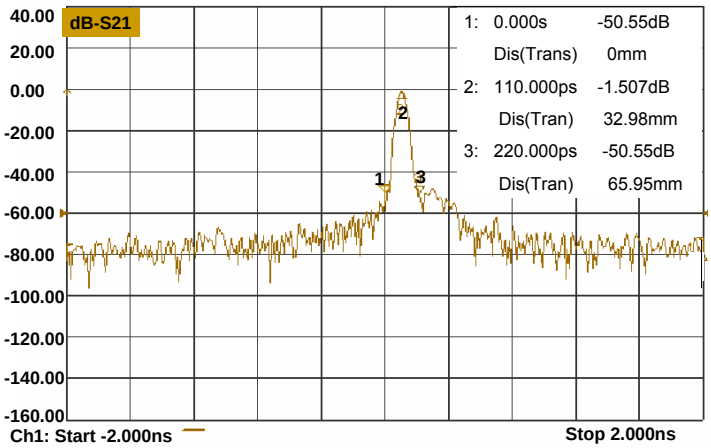

Figure 2.13 A time domain log-scale plot of the insertion loss parameter, S21, shows the maximum transfer of energy occurred at point 2 after 110ps (when the wave arrives at port 2).

At the interfaces, the reflections might be caused by two main reasons: mis-alignment and small air gap between the waveguide and adaptor. Although guiding pins and screws can help to get good alignment, there's still mis-alignment. The losses at the interfaces include the wave leaking caused by the small air gap as well.

The mis-alignment can be corrected by more precision machining of the flanges, and the air gap can be minimized by better planarization of the flange surfaces. Integrated manufacturing will be the final solution, in which alignment of adaptors will be elliminated. A horn antenna integrated with rectangular waveguide feed will be presented in Chapter 2, section 2.4. In the horn antenna, there is no flange connection between the horn aperture and the waveguide feed, thereby avoiding reflections caused by mis-alignment and air gaps.

Attenuation in a rectangular waveguide occurs mainly because of conductor losses. The measured conductivity of the electroplated gold layer using a four point probe is 1.5×10^6 /Ωm, which is much smaller than that of copper (5.96×10^7 /Ωm).

The measured scattering parameters of the plastic micro hot embossed W-band rectangular waveguide from 75 GHz to 110 GHz show minimum insertion loss of -1.06 dB at 109.6 GHz, which corresponds to 0.129 dB/λ_g. It is found that the performance is predicted and could be further improved by fixing the discontinuity between the waveguide itself and the network analyzer cable adaptors. An attenuation of 5.2 Np/m was measured at 95 GHz. It is envisioned that this new class of waveguides could facilitate the integration of other millimeter-wave components such as antennas, filters, and phase shifters toward an integrated system.

2.3 Iris Waveguide Filter

Filters are one of the most significant components in microwave systems. In terms of the frequency response, there are low-pass, high-pass, bandpass, and bandstop filters. With respect to the pass-band and stop-band responses, filters can be classified as maximum flat filters, equal ripple filters, and elliptic filters. A bandpass equal ripple (Chebyshev) filter was designed, fabricated, and tested to demonstrate the ability of plastic micro hot embossing technique to fabricate microwave filters.

In many applications, wide pass bands or wide stop bands are required. In these cases, strip-line and coaxial filters are usually preferable. However, one of the important considerations in choosing a type of microwave filter is the unloaded quality factor, *Q*. In strip-line and coaxial filters, owing to the presence of dielectric materials,

which are required for mechanical supporting purpose, they tend to have lower unloaded Q's. Waveguide and cavity filters give higher unloaded Q's that result in minimum insertion losses for a given fractional bandwidth.

An iris waveguide filter is constructed in a rectangular waveguide. It has the potential advantages of low losses, high Q-factors, and high power handling capability. A series of irises are designed in the cavity of a rectangular waveguide. With respect to the orientation of these irises, they are classified as E-plane and H-plane iris waveguide filters.

To fabricate an H-plane iris waveguide filter, one solution is to fabricate two identical parts then bond them together (shown in Figure 2.14 and Figure 2.15). Obviously, this method requires precise alignment at bonding.

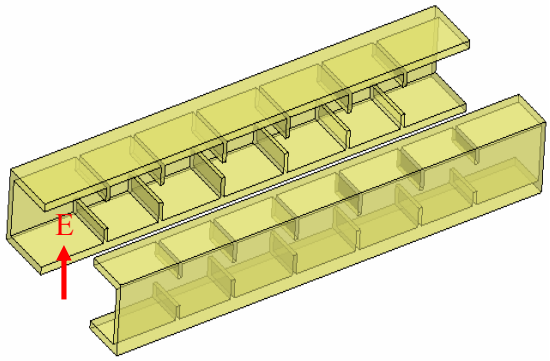

Figure 2.14 One solution to fabricate an H-plane iris waveguide filter. Two identical parts are fabricated then bonded together. In this way, it has an appropriate aspect ratio, but with stringent requirement for alignment.

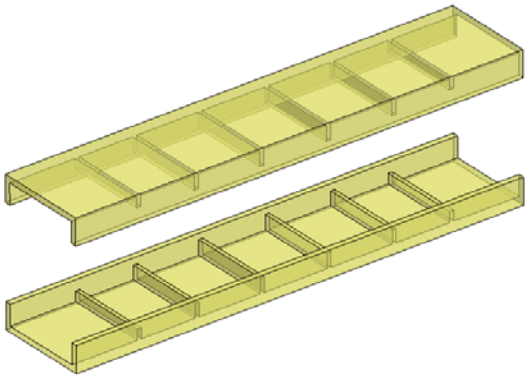

Figure 2.15 Similar to the process in Figure 2.14, two identical parts are fabricated then bonded together. Stringent requirement for alignment exists as well.

If hot embossing is applied along the H-plane direction, another way to fabricate the H-plane iris waveguide filter is shown in Figure 2.16. However, the aspect ratio required to make vertical walls will increase resulting in a thicker iris design. Hence, E-plane irises are chosen to form the iris waveguide filter because an appropriate aspect ratio and a process without aligned-bonding as shown in Figure 2.17 could be implemented.

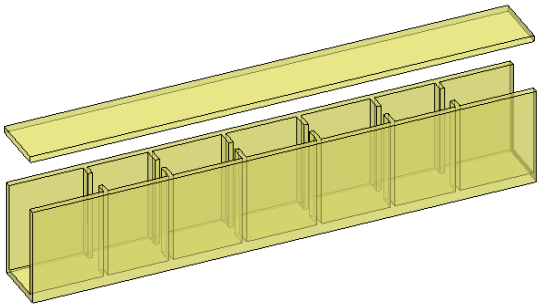

Figure 2.16 Hot embossing is done along H-plane. The requirement for aspect ratio is doubled compared to that in Figure 2.16.

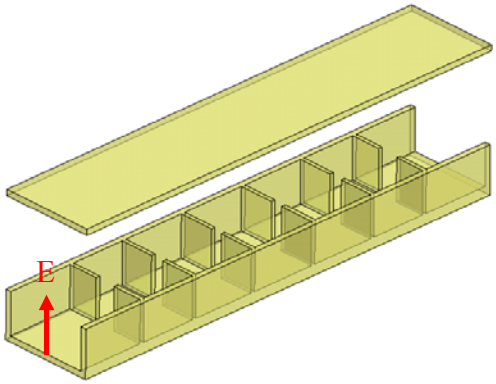

Figure 2.17 Hot embossing is done along E-plane.

2.3.1 Design

The process of filter design by the insertion loss method follows the sequence of filter specifications, low-pass prototype design, scaling and conversion, and implementation.

The center frequency of the filter is designed at 95 GHz. In order to obtain enough attenuation at the stop-band, the order of filter is chosen as 5.

For a 5-order equal ripple (Chebyshev) filter, if the ripple is defined to be within 0.1 dB, the low-pass prototype filter is designed as shown in Figure 2.18 (a) according to [2.12] in which g1=g5=1.1468, g2=g4=1.3712, and g3=1.9750. After filter transformation, a lumped-element bandpass filter is obtained, as shown in Figure 2.18 (b).

The lumped-element filter only works for low frequencies. Hence, in order to convert the lumped element model to a high frequency model, impedance inverters are used in the procedure of filter implementation to convert the lumped-element filter to a new microwave circuit model. The converted model is demonstrated in Figure 2.19.

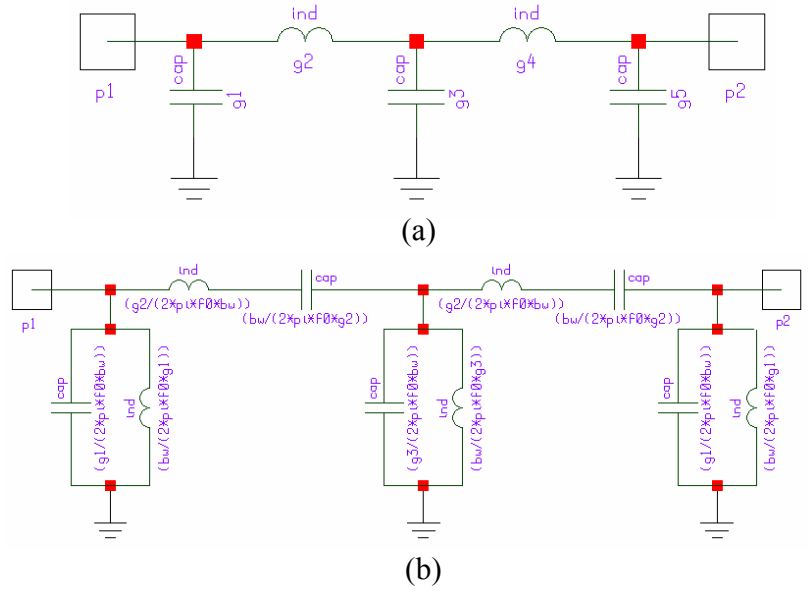

Figure 2.18 (a) A 5-order Chebyshev filter prototype and (b) its corresponding bandpass filter after filter transformation.

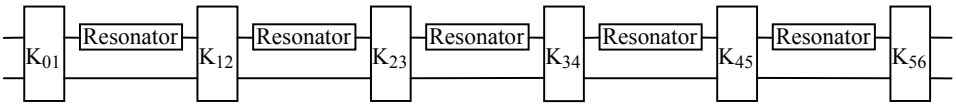

Figure 2.19 The bandpass filter model after using impedance inverters. $K_{01}=K_{56}=0.1868$, $K_{12}=K_{45}=0.0319$, $K_{23}=K_{34}=0.0243$. The resonators are all resonant at center frequency 95 GHz.

Then irises with different openings and spacings are designed to match these *K* values of the inverters and implement the resonators.

2.3.1.1 Design of an Iris Filter with Zero-Thickness Irises

If the iris thickness is so small that it can be considered as zero, according to [2.13], the iris forming a symmetrical window in a rectangular waveguide can be

modeled as a parallel inductor along a transmission line as shown in Figure 2.20. In Figure 2.20, $K = Z_0 \tan|\theta/2|$, $X = \dfrac{K}{1-(K/Z_0)^2}$, and $\theta = -\tan^{-1}\dfrac{2X}{Z_0}$.

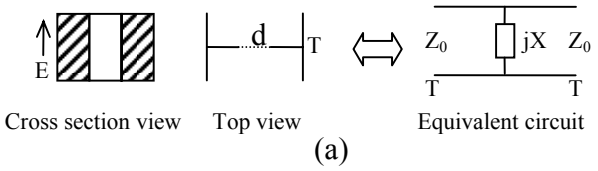

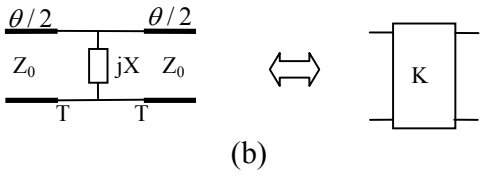

Figure 2.20 (a) An equivalent circuit for inductive irises in a rectangular waveguide. (b) Illustration of how the inductive iris implements an impedance inverter.

The only undetermined dimension for an iris is the window opening *d*. Eq. (2-3) gives the approximate relationship between *d* and inductive susceptance.

$$B = \frac{2\pi}{\beta a}\cot^2\frac{\pi d}{2a}\left(1+\frac{a\gamma-3\pi}{4\pi}\sin^2\frac{\pi d}{a}\right) \tag{2-3}$$

In Eq. (2-3), $\beta = [k_0^2 - (\pi/a)^2]^{1/2}$, and $\gamma = [(3\pi/a)^2 - k_0^2]^{1/2}$. By solving this equation, *d* can be obtained to corresponding inductive susceptance. Because the length of adjacent irises can be calculated by θ's, all dimensions of an iris waveguide filter are determined.

Adjacent irises can form a cavity. Waves are reflected back and forth in the cavity. For a desired cavity length, the cavity can resonate at the center frequency as

required in Figure 2.19. The *k*-th cavity length, *i.e.* the distance between adjacent irises, can be obtained by $l_k = \frac{\lambda_g}{2\pi}(\pi + \frac{1}{2}|\theta_{k-1} + \theta_k|)$.

2.3.1.2 Design of an Iris Filter with Finite-Thickness Iris Model

In many cases, the thickness of an iris is not small enough and cannot be neglected. A different model and design method were utilized.

For an iris physical geometry, there are two undetermined dimensions, *t* (the thickness of iris) and *d* (the window opening width). For the equivalent circuit model, there are 3 parameters (unknowns): X_s, X_p, and θ as shown in Figure 2.21. In Figure 2.21, $K = Z_0\left|\tan[\theta/2 + \tan^{-1}(X_s/Z_0)]\right|$, and $\theta = -\tan^{-1}\left(\frac{2X_p}{Z_0} + \frac{X_s}{Z_0}\right) - \tan^{-1}\frac{X_s}{Z_0}$.

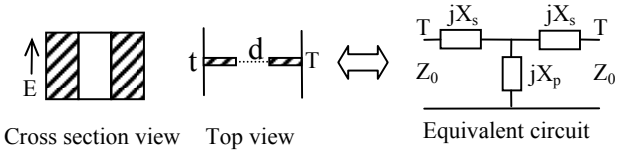

(a)

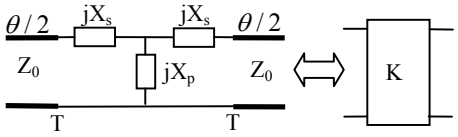

(b)

Figure 2.21 (a) An equivalent circuit for inductive irises in a rectangular waveguide. (b) An iris with two sections of waveguide and the respective impedance inverter.

For the impedance inverter model, K values are known from Figure 2.19. It is difficult to solve t and d, X_s, X_p, and θ from equations to match the K values. A full-wave simulation is utilized to find the desired iris geometry.

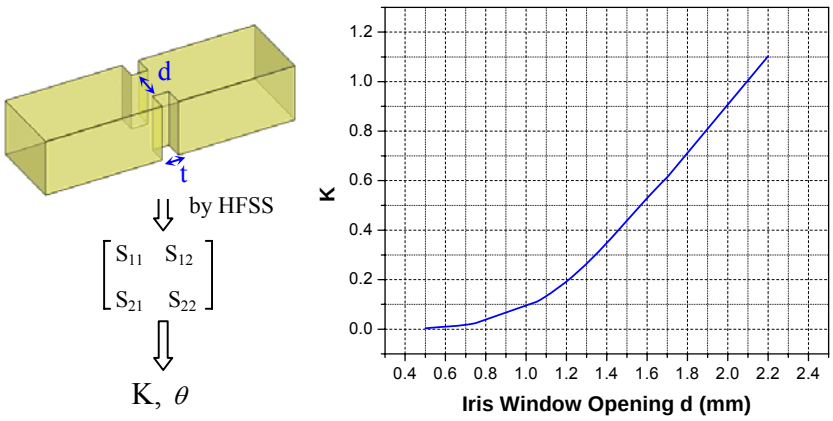

Figure 2.22 A HFSS model is used to determine the window opening d. For a given iris thickness, full-wave simulations are carried out to obtain S-matrices. Using these S-parameters, K and θ can be computed. The relationship between iris window opening d and impedance inverter K is shown graphically.

The thicknesses of the irises were chosen to produce a desirable aspect ratio from fabrication point of view. A full wave simulator HFSS (High Frequency Structure Simulator) is used to get the scattering parameters of a waveguide section containing an iris as shown in Figure 2.22.

The scattering parameters are used to compute the shunt and series reactances X_s and X_p. By transforming the fundamental-mode S-matrix elements of iris section into the impedance matrix of the circuit, the shunt and series reactances can be calculated as:

$$jX_s = \frac{1 - S_{21} + S_{11}}{1 + S_{21} - S_{11}}$$

$$jX_p = \frac{2S_{21}}{(1 - S_{11})^2 - S_{21}^2}.$$

For a standard W-band rectangular waveguide, the width, a, of the waveguide is 2.54 mm and the height, b, is 1.27 mm. The iris window openings are 1.192 mm, 0.795 mm, and 0.749 mm, according to K, which equals 0.1872, 0.03195, and 0.0243, respectively. The iris thickness is chosen as 0.50 mm. The k-th cavity length, the distance between adjacent irises, can be obtained by $l_k = \frac{\lambda_{g0}}{2\pi}(\pi - \frac{1}{2}|\theta_k + \theta_{k+1}|)$, which are 1.616 mm, 1.796 mm, and 1.809 mm, respectively.

After individual design of the iris opening and cavity length, all parameters are determined. A HFSS model was built to simulate the performance of the whole device as shown in Figure 2.23. The simulation results of the whole iris waveguide are shown in Figure 2.24.

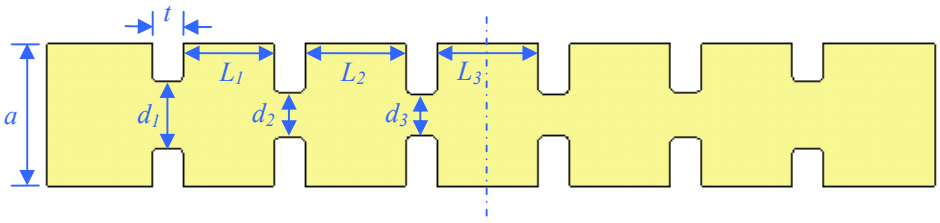

Figure 2.23 A HFSS model of the designed whole iris waveguide filter. a=2.54 mm, t=0.56 mm, d_1=1.192 mm, d_2=0.795 mm, d_3=0.749 mm, L_1=1.616 mm, L_2=1.796 mm, and L_3=1.809 mm.

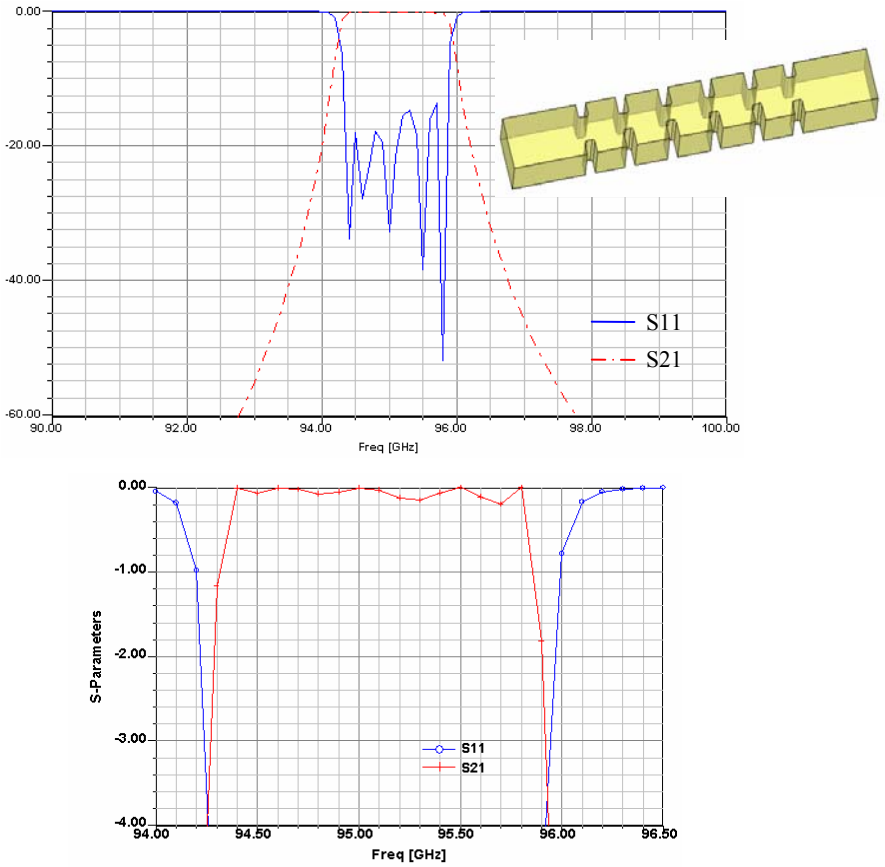

Figure 2.24 HFSS simulation results of an iris waveguide filter. Because of design errors of *K* (theory: 0.1868, 0.0319, 0.0243; designed: 0.1872, 0.03195, 0.0243), the ripple is larger than 0.1 dB.

2.3.2 Fabrication and Results

The micro hot embossing fabrication procedure is very similar to the fabrication of a rectangular waveguide. The whole process can be divided into five main steps as shown in Figure 2.25 to Figure 2.29.

The fabrication process begins with hot embossing the plastic piece by pressing two mold inserts together and then detaching the molds. Next, a thin layer of Cr/Pt is sputtered on both the hot embossed open waveguide and a silicon cover as the seed

layer for the following electroplating procedure. Meanwhile two identical flange adaptors are separately fabricated using the similar hot embossing process. Screw threads and pinholes are machined according to the *Agilent* precision circular flange data for W-band. The clamped open waveguide and silicon cover are fitted into the flanges and glued by epoxy. The surfaces of the flanges are planarized to get better connection and avoid wave leaking from large air gaps. At last, the whole device is immersed into a gold electroplating solution to deposit an 8-μm thick gold layer.

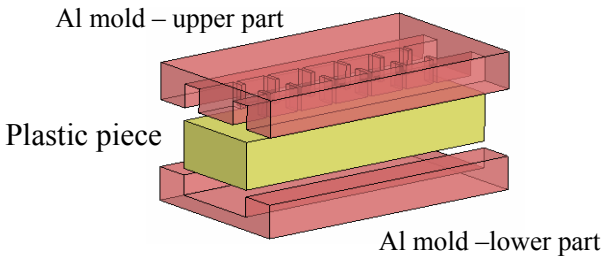

Figure 2.25 The plastic piece is hot embossed by pressing the two aluminum molds together.

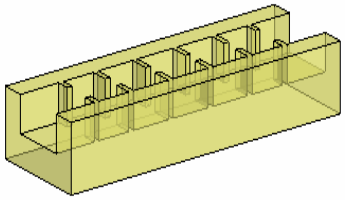

Figure 2.26 The hot embossed plastic piece is detached. Then Cr/Pt is sputtered on both the hot embossed plastic piece and the silicon cover.

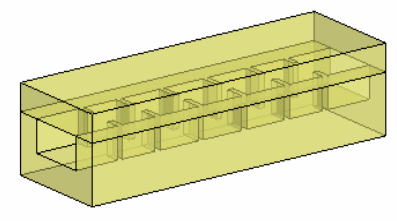

Figure 2.27 The silicon cover is clamped on top of the open waveguide to form closed cavity.

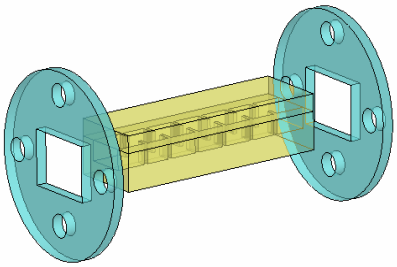

Figure 2.28 Two identical flanges are fabricated.

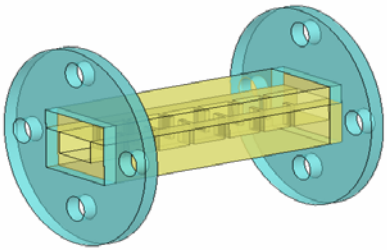

Figure 2.29 The clamped open waveguide and silicon cover are fitted into the flanges and glued.

Following the fabrication process illustrated from Figure 2.25 to Figure 2.29, a W-band iris waveguide filter has been manufactured by micro plastic hot embossing. Figure 2.30 shows the results of fabricated iris waveguide filter.

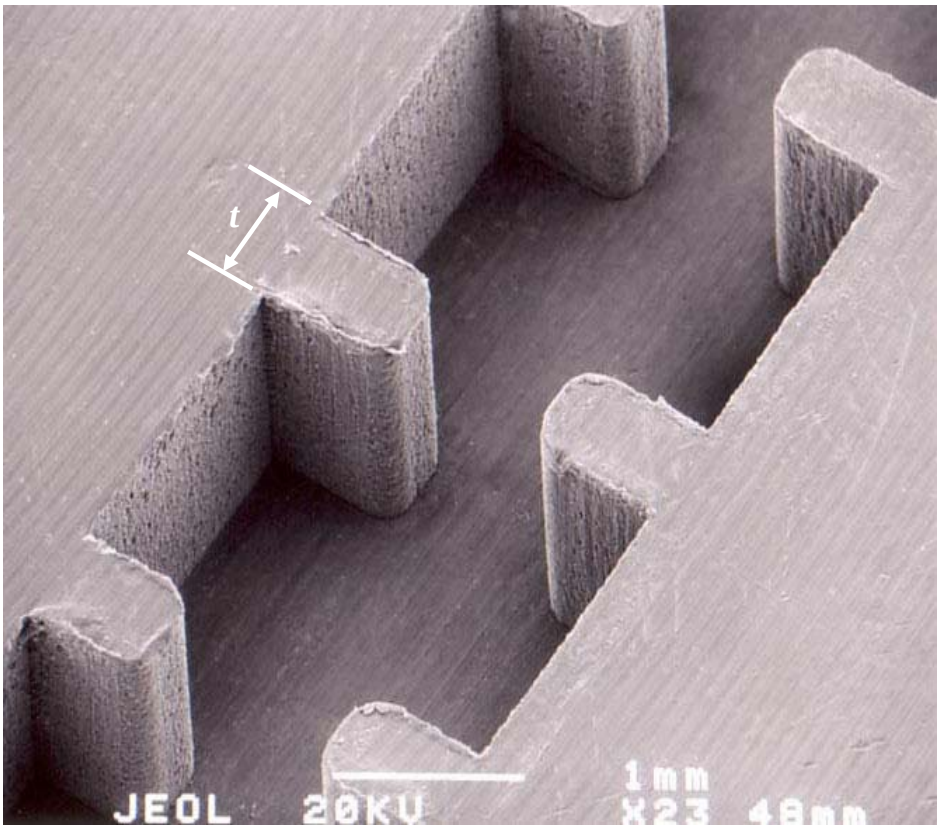

Figure 2.30 A SEM photo of the irises. The iris thickness, *t*, is 0.56 mm.

The plastic replica shapes are the complementary of the mold used in hot embossing. EDM (electrical discharge machining) was applied to manufacture the mold with a high aspect ratio (1.27 mm/0.56 mm). As a result of the limited machining capability of using a 125 μm EDM thread, the irises corners are rounded as shown in Figure 2.31.

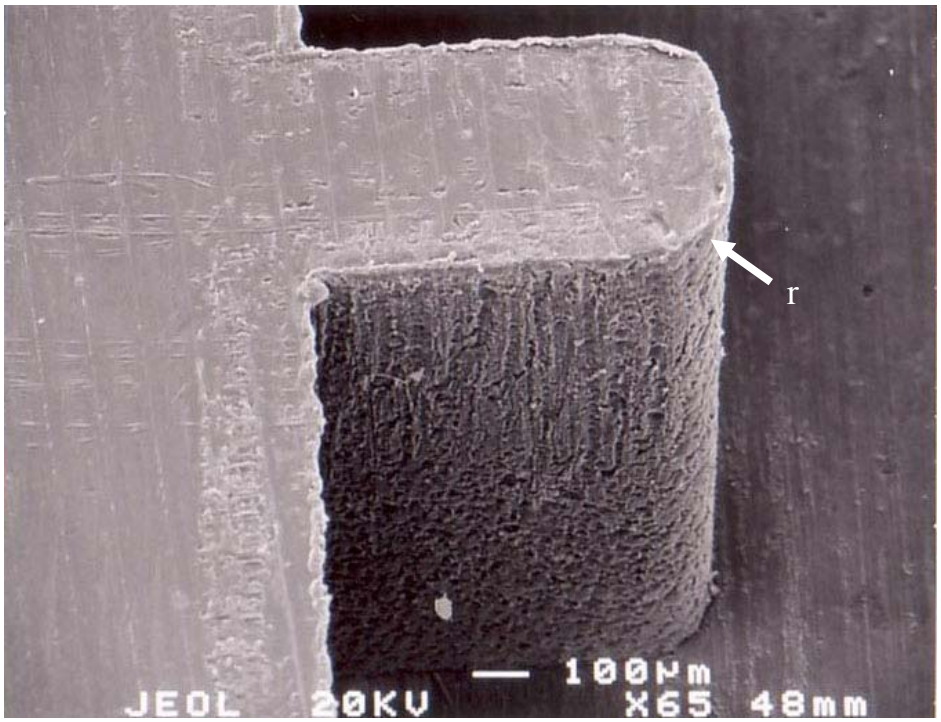

Figure 2.31 A close view of the round corners of an iris with 125 μm radius, *r*, due to using the EDM machining to manufacture the mold.

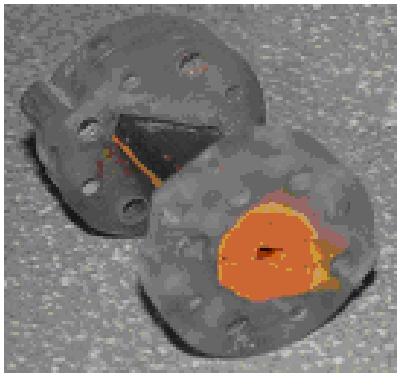

Figure 2.32 A photograph of the iris filter with integrated flanges.

The fabricated filter is design by the method presented in section 2.3.1. The iris filter is designed for a ripple level of 0.01 dB. The filter order is chosen as 5. The calculated *K*'s in Figure 2.19 are: $K_{01}=K_{56}=0.6503$, $K_{12}=K_{45}=0.3219$, and

K_{23}=K_{34}=0.2229. The iris window openings are: d_1=d_6=1.520 mm, d_2=d_5=1.066 mm, and d_3=d_4=0.912 mm. The resonant lengths are: L_1=L_5=1.851 mm, L_2=L_4=2.138 mm, and L_3=2.207 mm.

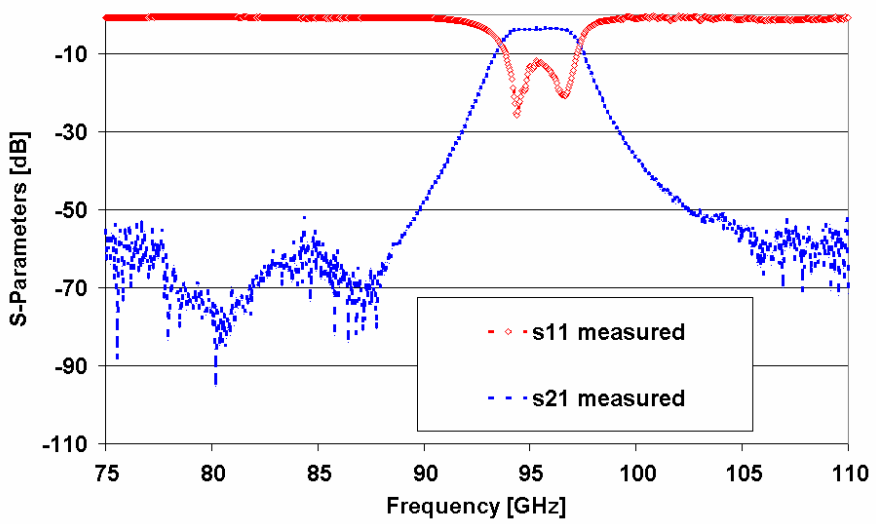

Figure 2.33 Measured S-parameters of the fabricated iris waveguide filter.

Figure 2.33 shows the measured S-parameters with a pass-band between 93.7 and 97.2 GHz. The measured results show a 3-dB bandwidth of 3.5 GHz (3.68%) and a 20-dB bandwidth of 6.2 GHz (6.53%). The insertion loss and return loss at 95 GHz are -3.49 dB and -18 dB, respectively, and the rejection loss in stop band is better than –50 dB.

According to $IL(dB) = 4.343\frac{Q_{bw}}{Q_u}\sum g_i$ given by [2.12], where IL is the average filter insertion loss in dB, Q_{bw} is the filter's center frequency divided by the ripple bandwidth, Q_u is the unloaded quality factor, $\sum g_i$ is the sum of N g-values used to

design the filter, Q_u can be calculated. From the measured iris waveguide filter data, the average insertion loss is about 3.5 dB. Q_{bw} =27.14. $\sum g_i = 7.011$. Hence, $Q_u = 236$. As explained in the Section 2.2.2, the mis-alignment and air gaps at the connections result in some reflections at the connection interfaces. Therefore, if loss issues with the two waveguide interfaces are subtracted from the insertion loss equation, the calculated Q_u should be much higher.

2.3.3 Temperature Effect on Plastic Iris Waveguide Filter Performance

Plastic micro hot embossing technique has the advantages of reproducing millimeter-wave devices quickly, massively, and cheaply. The manufactured devices are light and the material cost is low, compared to the heavy and expensive metal materials such as copper, brass, and aluminum. However, there is a thermal expansion issue on the plastic devices. When the ambient temperature of the plastic micro hot embossed device is changes, due to the thermal expansion of the plastic material, the physical dimensions of the device will be altered. As a result, the electrical performance of the device will be changed.

At the room temperature, the CTE (coefficient of thermal expansion) of copper, brass, and aluminum are $17\times10^{-6}/K$, $19\times10^{-6}/K$, and $23\times10^{-6}/K$, respectively. However, the CTE of plastic materials is much larger. For example, for BCB (Benzocyclobutene), its CTE is $42\times10^{-6}/K$ at 27°C. Hence, compared to the metal manufactured millimeter-wave devices, the plastic micro hot embossed components are more sensitive to the temperature change.

Table 2.1 lists the dimension changes of the iris waveguide filter illustrated in Figure 2.23 at the room temperature, 80°C, and -40°C.

Table 2.1 Dimension changes due to temperature variance.

Dimention Name	**Values (mm)**		
	27°C	**80°C**	**-40°C**
a	2.54	2.546	2.533
b	1.27	1.273	1.266
L_1	1.616	1.620	1.611
L_2	1.796	1.800	1.791
L_3	1.809	1.813	1.804
t	0.56	0.561	0.558
d_1	1.192	1.195	1.187
d_2	0.795	0.797	0.793
d_3	0.749	0.751	0.747

Figure 2.34 and Figure 2.35 shows the iris waveguide filter performance changes due to the altered dimensions under different temperature.

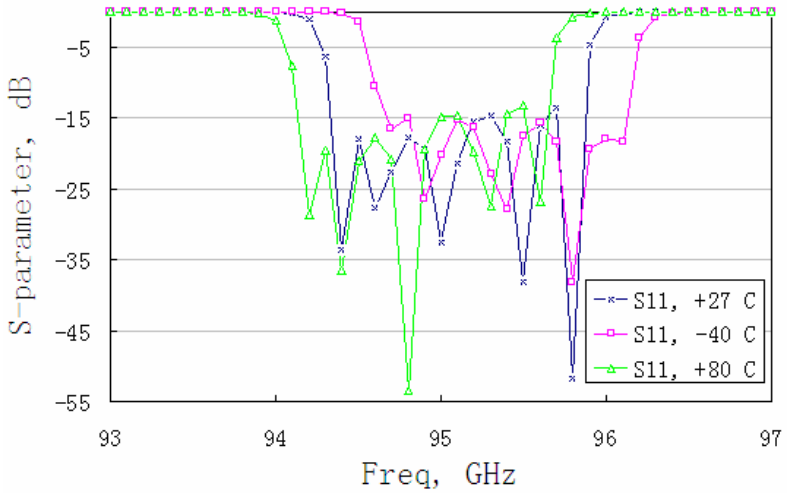

Figure 2.34 Return losses at different temperature.

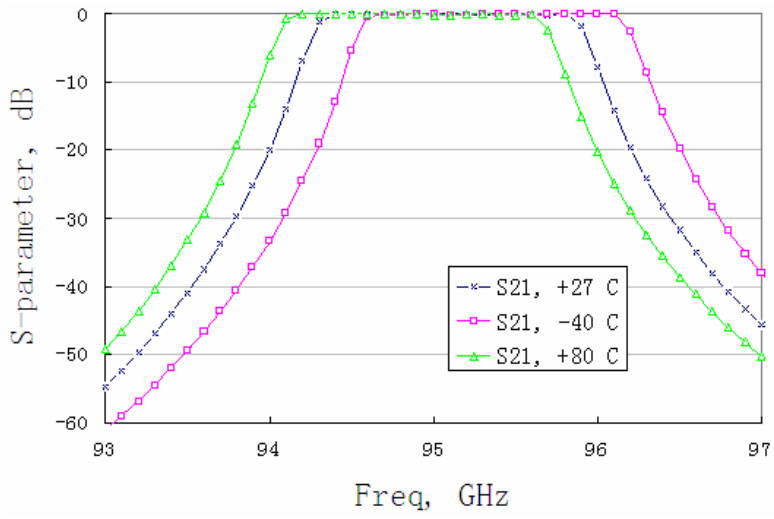

Figure 2.35 Insertion losses at different temperature.

Figure 2.34 and Figure 2.35 illustrate the effect of temperature change on the iris waveguide filter performance. The pass-band of the filter is shifted. At -40°C, the 3-dB pass-band is from 94.5 GHz to 96.2 GHz. At the room temperature, the pass-band is from 94.2 GHz to 95.9 GHz. At 80°C, the pass-band is from 94 GHz to 95.7 GHz. Although the pass-band is shifted at different temperature, the 3-dB bandwidth is almost unchanged as 1.7 GHz.

2.4 Micro Hot Embossed Horn Antenna

Horn antennas have been widely used in many applications because of their advantages of simplicity in construction, ease of excitation, versatility, large gain, and preferred overall performance. The most widely used horn is the one which is flared in both directions, referred as a pyramidal horn. Its radiation characteristics are essentially a combination of the E- and H-plane sector horns.

For a horn antenna, a longer horn or a smaller horn angle will achieve a more uniform aperture distribution. However, in practice, there is usually a limitation on the length of the horn due to the limited system space. In many applications, the dimensions of the horn antenna are very small and difficult to be precisely manufactured. Hence, the production cost is high. People have tried to manufacture the horn antennas by alternative manufacturing techniques found in IC industry. IC fabrication techniques offer the opportunity to fabricate millimeter-wave parts with lower costs and higher reliability than those manufactured by conventional machining techniques.

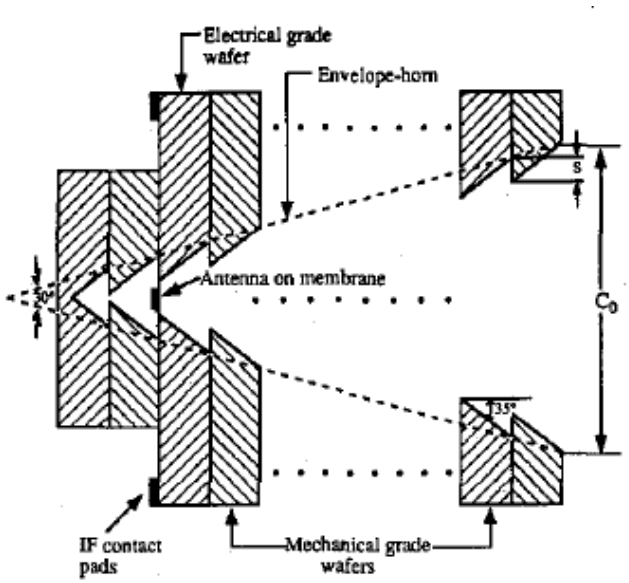

Figure 2.36 A horn antenna formed by a stack of silicon wafers. Each silicon wafer is wet etched to get desired apertures [2.14].

Rebeiz *et al.* presented a horn antenna fabricated by anisotropic wet etching of several silicon wafers and bonding them together [2.14], as shown in Figure 2.36. This

step-profile horn antenna reduced the effective flare angle of the horn to around 30° and allowed for gains in the region of 17 dB to 20 dB to be achieved.

Bassem presented his work on fabrication of W-band horn antennas by anisotropic wet etching silicon substrates [2.15], as shown in Figure 2.37. The silicon wafer was etched using EDP (Ethylene-diamine-pyrocatechol) solution. The horn flare angle was controlled with the mask used for etching the wafer. The resultant structures had a diamond-shape cross section. A metal transition had to be machined and utilized to provide smooth transition from the diamond-shaped cross section to a rectangular waveguide.

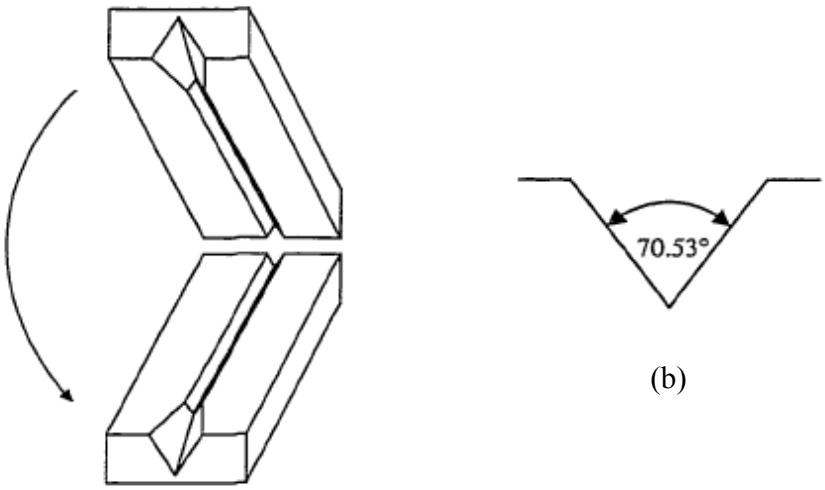

Figure 2.37 (a) Two identical halves of clamshells are bonded together to form a V-shape waveguide and a horn antenna. (b) Depiction of the cross-section of the waveguide as dictated by the anisotropic wet etching of (111) crystal planes in silicon.

In this dissertation, a horn antenna has been designed and fabricated to demonstrate the feasibility of micro plastic hot embossing for radiation components.

The demonstration extends the hot embossing capability from a "2-dimentional" manufacturing to a complex "3-dimentional" one.

The working frequency of the horn is chosen to be 95 GHz. The rectangular feed waveguide is a standard W-band waveguide (WR-10) with a=2.54 mm and b=1.27 mm. Other dimensions shown in Figure 2.38 are L_b=1.61 mm, L_f=1.41 mm, H=7.13 mm, a_1=10.11mm, and b_1=7.69 mm. Hence, θ_E =56°, and θ_H =48.5°, H/λ=2.26, where θ_E and θ_H are E-plane flare angle and H-plane flare angle, λ is the wavelength.

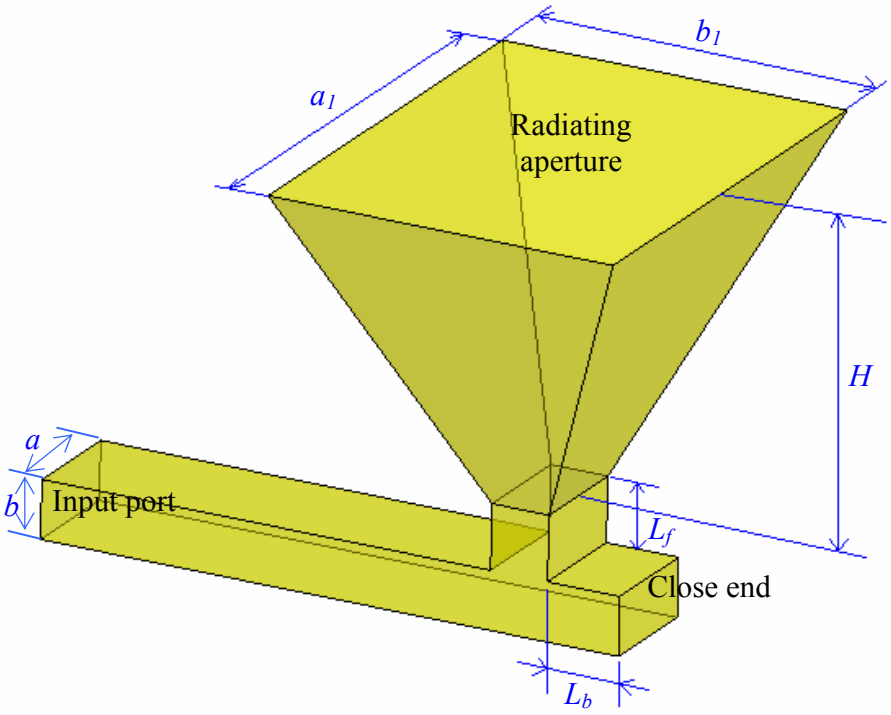

Figure 2.38 The pyramidal horn antenna with integrated waveguide feed.

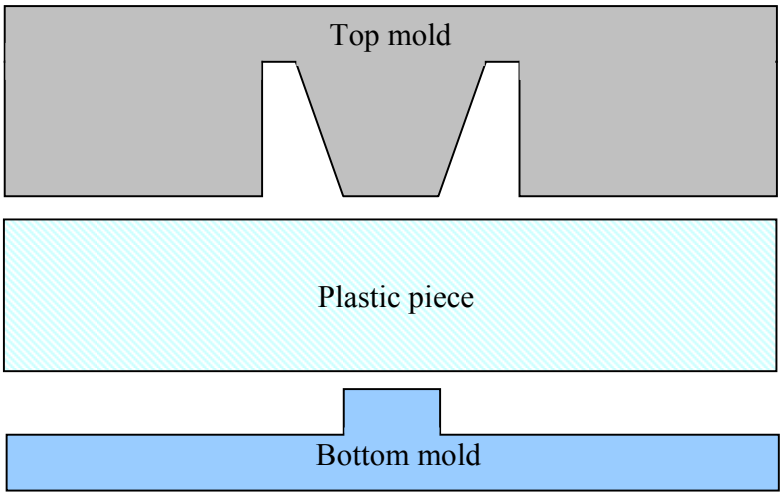

Figure 2.39 Two molds are used to fabricate the horn antenna and its integrated waveguide feed.

In order to fabricate the horn and its waveguide feed structure integratively, two molds were used in the micro hot embossing technique as shown in Figure 2.39. Figure 2.40 shows the fabrication result after de-embossing. In the following processes, first a seed layer of Cr/Pt is deposited as the seed layer for gold electroplating process. After the cover is clamped to the plastic, both the cover and plastic piece are fit into a plastic flange. Then the whole device is electroplated an 8-μm thick gold layer. Figure 2.41 shows the micro hot embossed plastic horn antenna and its waveguide feed.

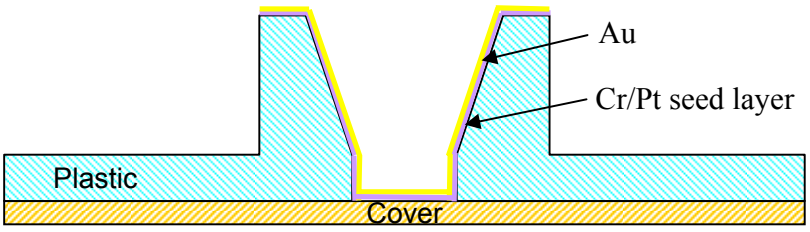

Figure 2.40 The plastic replica and its cover. After the plastic substrate is detached from the molds, a cover is clamped to the plastic to close the waveguide cavity.

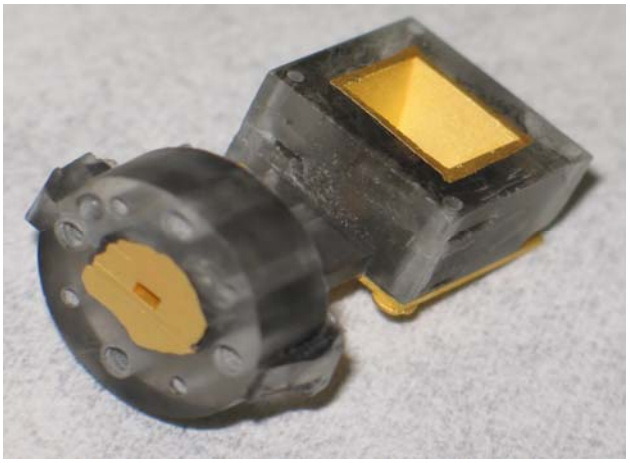

Figure 2.41 A photograph of an integrated horn antenna and its waveguide feed.

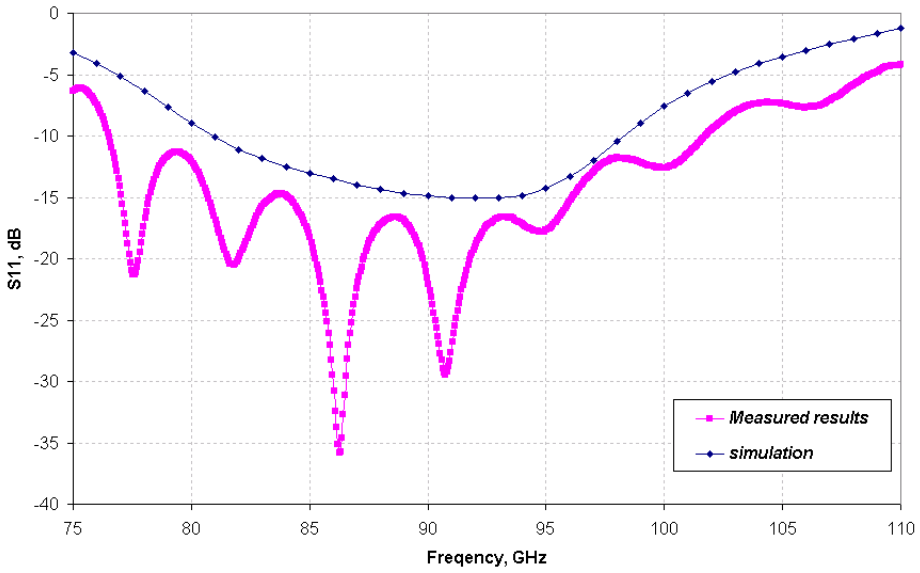

Figure 2.42 The simulated and measured reflection coefficients in W-band.

The antenna parameter is directly measured by a vector network analyzer. Figure 2.42 shows the measured S11 and simulation results. The return loss is lower than -17.6 dB at 95 GHz. The 15 dB bandwidth is 12.6 GHz (83.5 GHz to 96.1 GHz). The outline of the measured data curve matches the simulation results. The resonant

nulls are believed due to the mis-alignment and air gap at the connection between the flange and the standard waveguide feed. This phenomenon has been previously observed at the waveguide and iris waveguide filter measurements.

Figure 2.43 shows the antenna radiation pattern measurement set up. A standard horn antenna is used as a transmitter in the measurement. The under-testing micro hot embossed horn antenna is configured as a receiver connected to a standard waveguide port by flanges, which has been illustrated in the section 2.2.2.

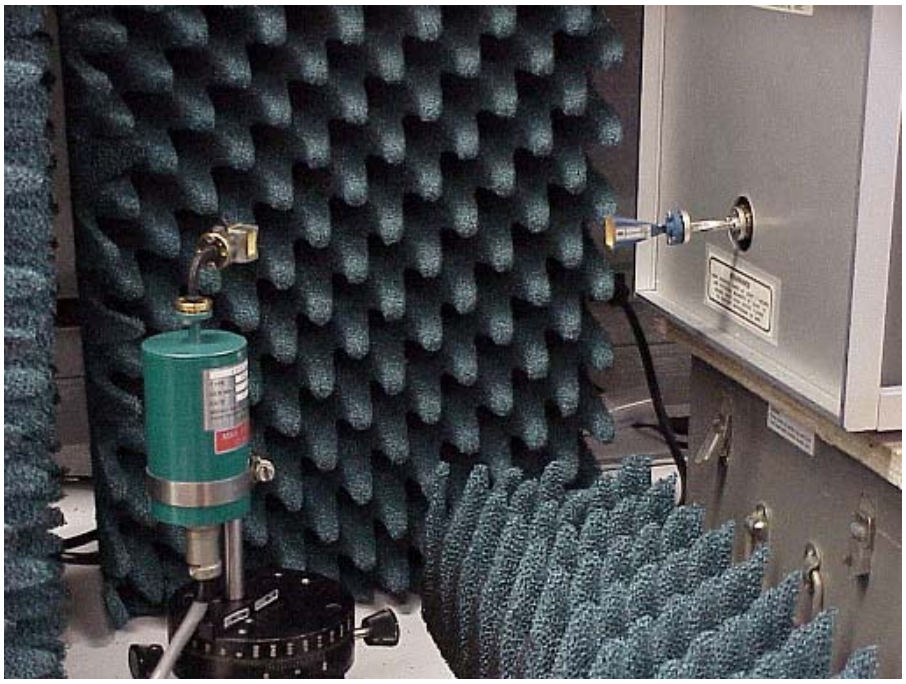

Figure 2.43 The micro hot embossed horn antenna measurement set up.

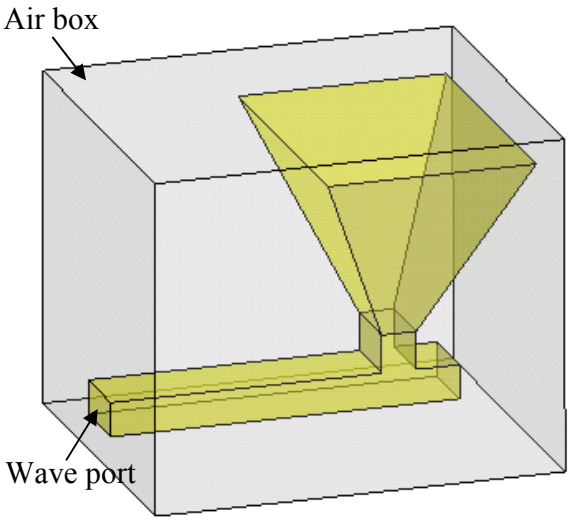

Figure 2.44 The HFSS model used to simulate the horn antenna and its waveguide feed.

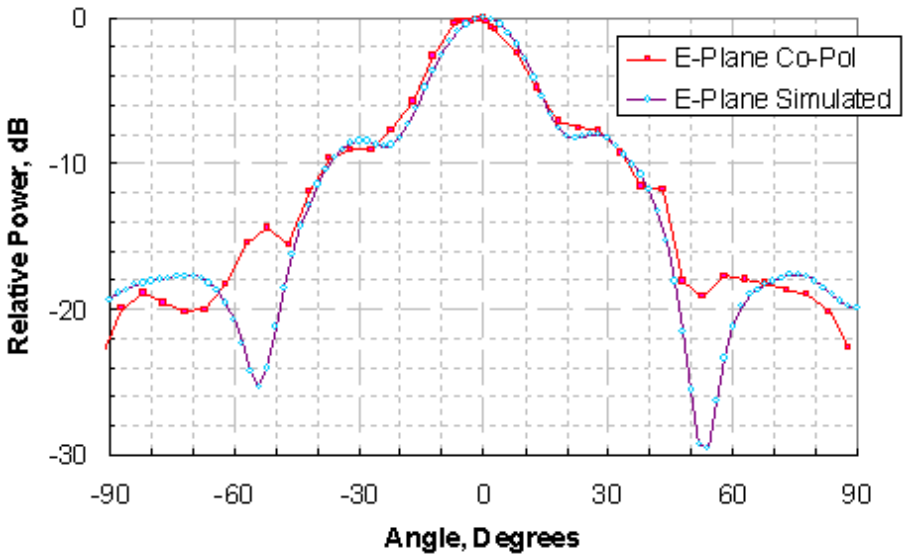

Figure 2.45 The measured and simulated horn antenna E-plane pattern.

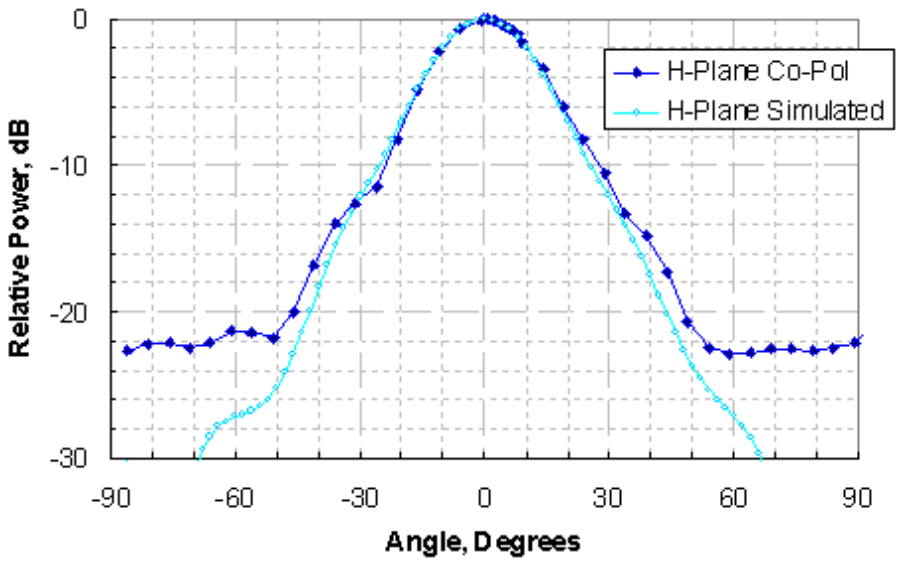

Figure 2.46 The measured and simulated horn antenna H-plane pattern.

A HFSS model is used to simulate the horn antenna and its waveguide feed as shown in Figure 2.44. The excitation port is defined at the input of the rectangular waveguide. All walls of rectangular waveguide and horn are defined as perfect E boundaries. The horn aperture is defined as a perfect H boundary. And an air box is built to surround the whole horn antenna. The surfaces of air box are defined as radiation boundaries for the antenna model.

From the measured E-plane and H-plane patterns shown in Figure 2.45 and 2.46, the 3 dB beamwidth of E-plane and H-plane are 21.7° and 25.4°, respectively. From [2.16], $D \approx \frac{32{,}400}{\theta_1 \theta_2}$, where θ_1 and θ_2 are the E-plane and H-plane beamwidths, in degrees. Hence, the directivity, D, is approximately equal to 58.8. If it is assumed that the horn antenna is lossless ($\eta = 1$), then $G = 10\log(\eta D) = 17.7$ dB.

2.5 More Designs for Micro Hot Embossing

To date, a rectangular waveguide, an iris waveguide filter, and a horn antenna have been successfully fabricated by plastic micro hot embossing technique. The feasibility of using the micro hot embossing technique to manufacture millimeter-wave components at low cost and light weight has been demonstrated.

Besides waveguides, filters, and horn antennas, other millimeter-wave devices such as coupler and slotted waveguide antenna are feasible to be fabricated by micro hot embossing on plastic materials as shown in Figure 2.47, Figure 2.48, and Figure 2.50.

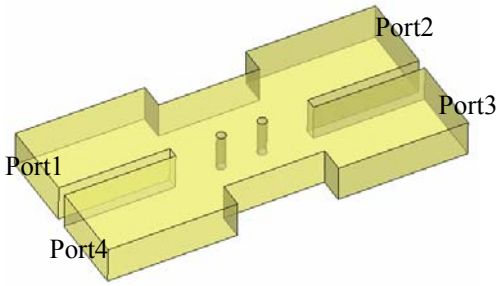

Figure 2.47 A Riblet directional coupler model.

Figure 2.47 shows the structure of a directional coupler. Compared to a conventional Riblet short-slot coupler, this design has two posts arranged in the center of waveguide axis in the coupling region. These two posts are used to suppress reflections. In the coupling region, the waveguide is narrowed, which can help to restrain the TE_{30} and higher modes from propagating.

However, for this design, the two posts are very difficult to manufacture by micro hot embossing. A new design is illustrated in Figure 2.48. This design is based

on a Riblet short-slot coupler structure as well. However, in the coupling range, the waveguide is narrowed in multiple steps.

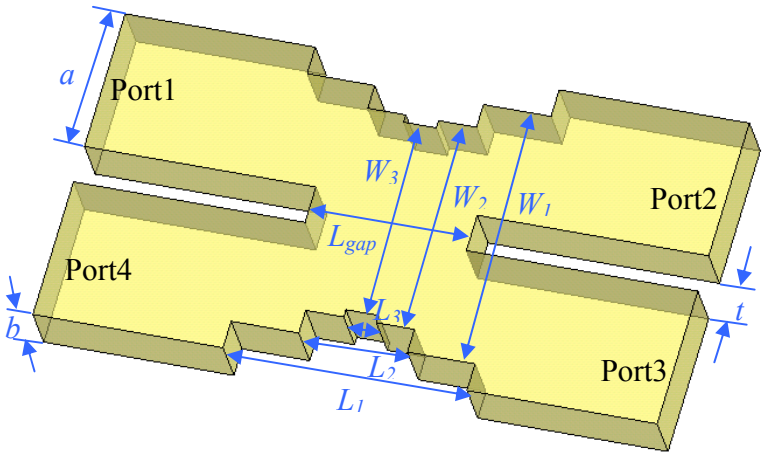

Figure 2.48 A Riblet directional coupler model without posts inside waveguide.

In Figure 2.48, the dimensions are a=0.1 in, b=0.05 in, which are corresponding to a standard W-band rectangular waveguide, t=0.027 in, L_1=0.171 in, L_2=0.076 in, L_3=0.023 in, L_{gap}=0.114 in, W_1=0.187 in, W_2=0.152 in, and W_3=0.141 in.

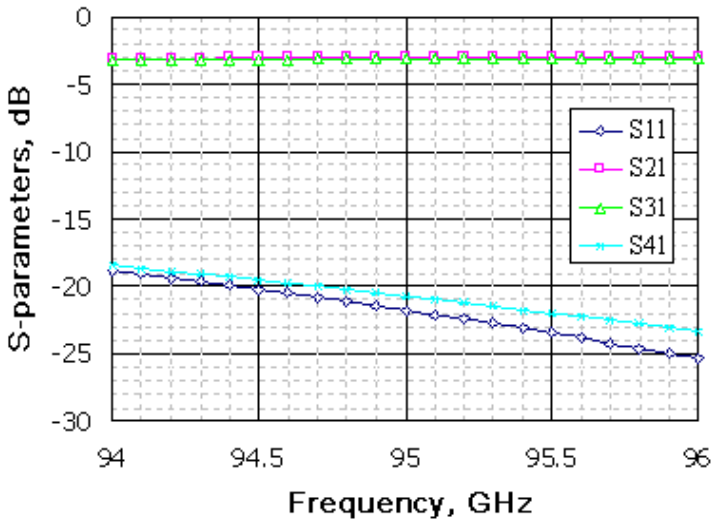

Figure 2.49 Simulation results of the quadrature hybrid directional coupler.

Figure 2.49 shows the simulation results of this hybrid directional coupler. At 95 GHz, S21=-3.03 dB, S31=-3.12 dB. The simulated results show that after waves are excited into the input port, they are almost evenly distributed into the two output ports, and the phase shift between the two output ports is 88.92˚.

Horn antennas have the advantages of simple structure, high directivity, and high gain. However, the big size of the horn antenna is a great challenge. Compared to horn antenna, a slotted waveguide antenna is flat and relatively thin as shown in Figure 2.50. Hence, slotted waveguide antennas could be gimbaled over wide angles in a small volume such as an aircraft nose radome.

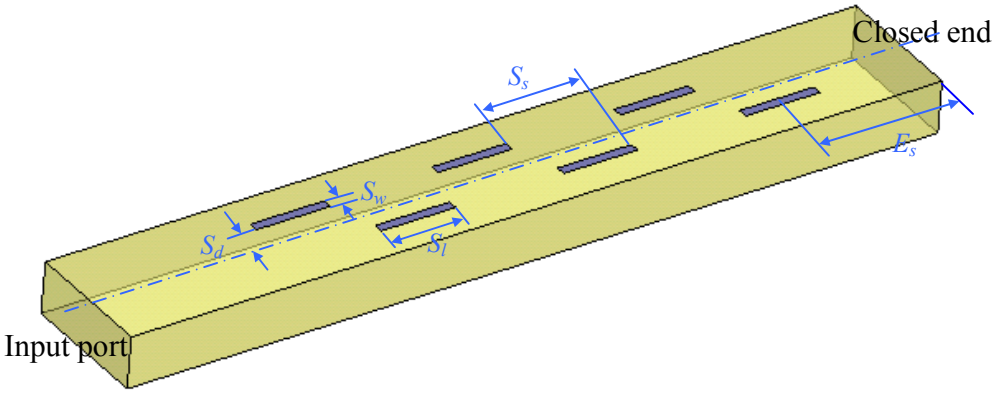

Figure 2.50 A slotted waveguide antenna model.

A slotted waveguide antenna has been designed at K-band as shown in Figure 2.50. The working frequency is chosen at 24.15 GHz. The waveguide is WR-42, with an opening of 10.67 mm x 4.32 mm. S_d=2.12 mm, is the slot displacement from the center axial of the waveguide. S_w=0.74 mm and S_l=6.09 mm, are slot width and length, respectively. S_s=7.64 mm, is the spacing between adjacent slots. E_s=3.82 mm, is the

end spacing between the closed end of waveguide and the last slot. The simulated the antenna pattern is depicted in Figure 2.51.

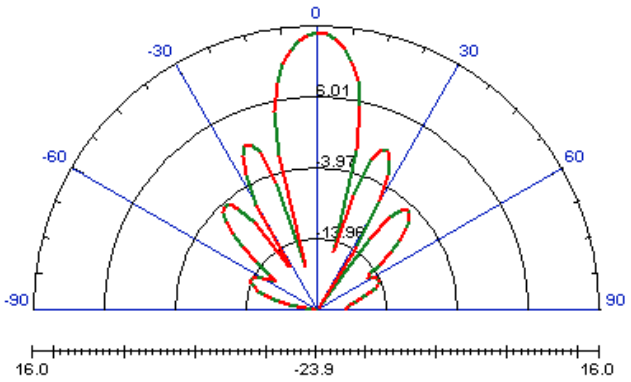

Figure 2.51 Simulated radiation pattern of a 6-slot waveguide antenna.

CHAPTER 3

A NOVEL RF MEMS STRUCTURE AND ITS APPLICATIONS

RF MEMS devices have been demonstrated with great promises in commercial and defense applications, including satellite communications systems, wireless communication systems, aerospace, instrumentation, automobile, and radar systems *etc*. RF MEMS devices in millimeter-wave systems often greatly improve system performance and expand applications of millimeter-wave systems into new applications [3.1].

The applications of RF MEMS can be divided into four distinct areas according to [3.1]. The first area includes micromachined transmission lines, high-Q resonators, filters and antennas, which are static and do not have any movable parts. The second area is based on thin film bulk acoustic resonators and filters, which use acoustic vibrations in thin films. The third area covers RF micromachined resonators and filters, in which the mechanical movements are only of the order of tens of angstroms. The last area is focused on RF MEMS switches, varactors, and their applications in filters and phase shifters. In this area, a large number of RF MEMS devices use the parallel plate actuator structure or similar structures. In this chapter, a novel RF MEMS multi-step parallel plate structure is presented. Its high power handling capability is discussed. Finally, the applications of this novel actuator structure in phase shifters are introduced.

3.1 Novel Multi-Step Actuator Structure

The electrically actuated parallel plate structure, widely used in MEMS devices, is composed of two parallel metal plates separated in air, as shown in Figure 3.1. Usually one plate is fixed while the other one is suspended. When a voltage potential is applied to the plates, the suspended plate will move towards the fixed one until the electrostatic and spring forces reach equilibrium.

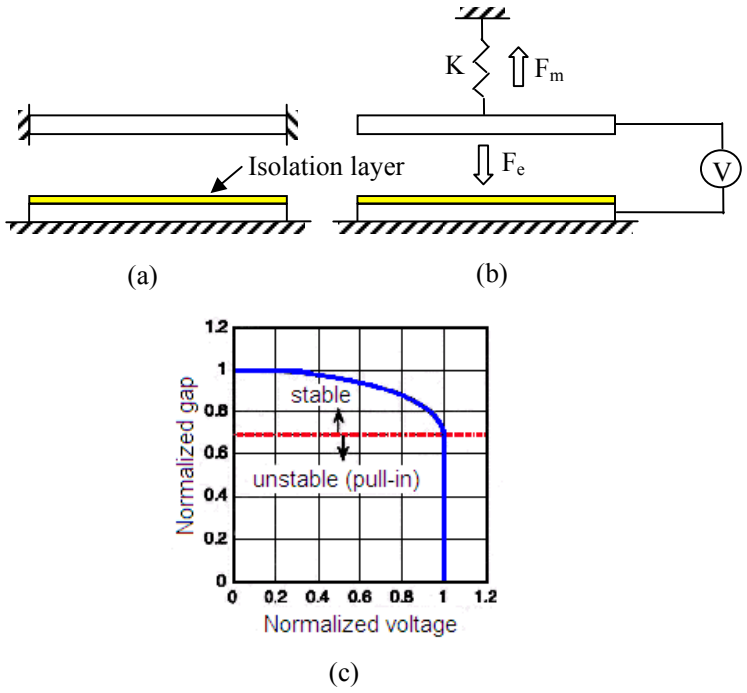

Figure 3.1 (a) A parallel plate structure. The top plate is clamped at the two ends. The bottom plate is fixed on the ground. (b) An equivalent model of electrically actuated parallel plate structure. (c) The pull-in effect and the stable tuning range.

If the bias voltage keeps increasing, the top plate will go on to move down because of the increasing electrostatic force. The electrostatic force increases much faster than the restoring mechanical force. Hence, at a certain voltage, $V_{pull\text{-}in}$, the top plate will suddenly be pulled down until it touches the dielectric layer on top of the

bottom electrode. This process is shown in Figure 3.1 (c). For a binary operation, there are two discrete capacitances, the initial state and the state after pull-in. For a continuous tuning operation, there is one stable controllable tuning range.

This actuation structure has been applied in many MEMS devices. Young and Bover [3.2] first presented the design of a micromachined varactor using electrostatically actuated plates. Efforts to increase the varactor tuning ranges by adding separated electrodes [3.3, 3.4], employing an array of capacitors [3.5], or composing several discrete-position varactors [3.6] have been made.

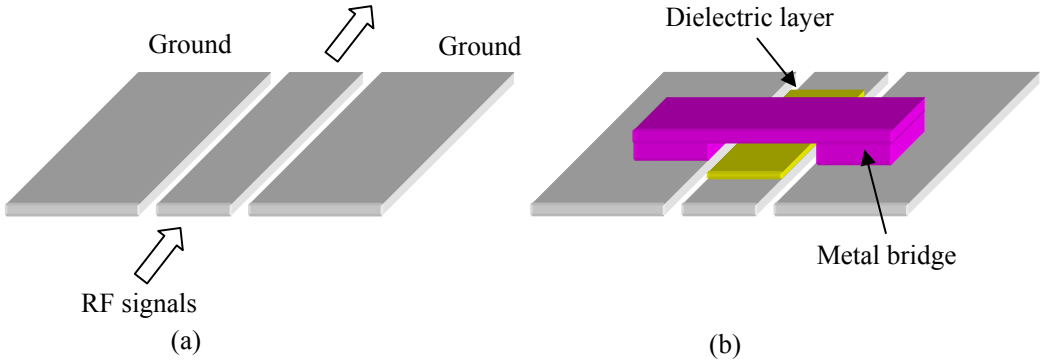

Figure 3.2 (a) A CPW transmission line. (b) A metal bridge over the CPW changes the electromagnetic field distribution in the air.

MEMS switches based on electrostatic actuators in a coplanar waveguide (CPW) have been developed and widely used. They consist of a thin metal membrane or beam, which can be electrostatically actuated by a DC voltage, across the center conductor. As shown in Figure 3.2, the membrane is suspended over the center conductor of a CPW and anchored at both ends on the ground plane. A thin dielectric layer is deposited on top of the center conductor for DC insulation. The balance between the stress of membrane and the electrostatic forces decides the air-gap height. When the air

gap is changed with different bias voltages, the signals passing through the CPW line are changed.

Although the parallel plate structure and its corresponding MEMS switch are well developed and widely used, there are issues and related technical challenges. The stress of the membrane is difficult to control as it depends on the materials, mechanical configurations and temperatures. The thermal expansion of metal film results in variations of air-gap heights at different ambient temperatures producing variation of phase shifts and noises. To overcome the problems, one could design the membrane configuration to be overcompensated with a high stress. This, however, requires high actuation voltages to bend the membrane. The high voltage therefore causes charging effects on the dielectric layer, contact stiction problems and signal power handling limitation [3.7, 3.8]. The limited capacitor ratios and tuning ranges become a bottleneck and hinder applications of the varactors.

In this dissertation, a new multi-step actuator structure is presented. Figure 3.3 illustrates its configuration. Micro structures are constructed on a high-resistivity silicon wafer. A CPW line lies on the bottom level. On each side of the ground conductors, multiple layers are constructed to form membrane-constraining steps. Electrodes are deposited and patterned on these steps. Thin dielectric layers are sputtered on top of the electrodes for insulation. A metal membrane is suspended over the whole structure.

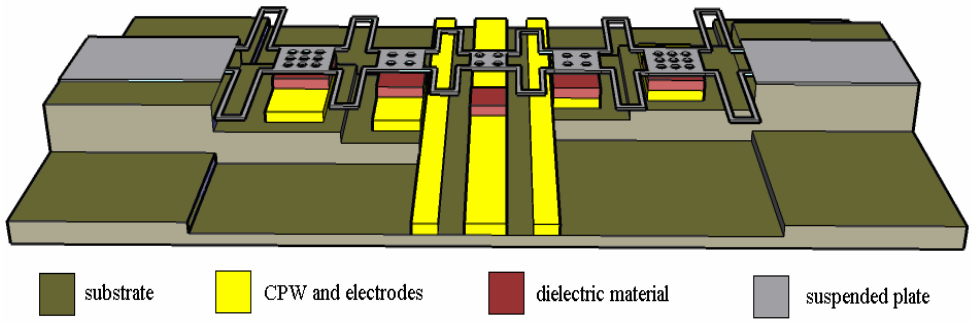

Figure 3.3 A 3-D drawing of the multi-step actuator structure (not to scale).

When voltage is applied across the membrane and specific electrodes, the membrane will experience electrostatic forces and be dragged down. If voltage keeps increasing up to the pull-in voltage, the membrane will be pulled down and stopped by the steps where the electrodes are. By design, the rest of the membrane remains stiff and the certain air-gap height to the CPW line is achieved. By applying biasing voltages on different electrodes, different air-gap heights can be reached.

This multi-step actuator structure can be applied for varactors and RF capacitive switches with several advantages. As an example in one of the designs, it increases the capacitor ratio to 355, in three states. Similar single step varactors have been reported in [3.4, 3.5] as 1.7 – 1.9 and in [3.6] as 3. It also increases the tuning resolution from binary states to 3 states. The reactance resolution could be more if more steps are constructed. This provides multiple discrete capacitance values instead of on/off two-stable values. Using multiple steps and electrodes, it helps to increase power handling

capability [3.9, 3.10]. The device configuration also benefits from the complex, yet compact, control mechanism as well.

3.1.1 Design and Simulation

Conventionally, the actuator is modeled as a first-order approximation system consisting of two parallel plates separated by a gap g_0, with one plate fixed and the other suspended as shown in Figure 3.1 (b). When a bias voltage V is applied across the plates, neglecting the thin dielectric film thickness, the force balance is given by:

$$0 = F_m + F_e = Kw - \frac{1}{2}\frac{\varepsilon A}{(g_0 - w)^2}V^2$$

$$\frac{\varepsilon A V^2}{2(g_0 - w)^2} = Kw \tag{3-1}$$

where K is the equivalent spring constant, A is the area of the suspended plate, ε is the electric permittivity of free space, g_0 is the initial gap, and w is the displacement.

When the bias voltage applied on the plate increases slowly, the suspended plate will be dragged down gradually. The mechanical force F_m increases proportionally to the first order of w according to $F_m = Kw$. Meanwhile, owing to the second order of w in the denominator of F_e, the electrostatic force F_e increases much faster than F_m with the changing of plate displacement. As the bias voltage increases to a certain value and the plate moves down 1/3 of the total gap, then the mechanical force becomes less than the increasing of electrostatic force. As a result, the plate will suddenly move down until it touches the dielectric layer. Taking the differential of Eq. (3-1) on both

sides, the equation can be solved to obtain $w = \frac{2}{3} g_0$, which matches the observation. The voltage at this moment is called pull-in voltage. The pull-in voltage can be derived as

$$V_{pull-in} = \sqrt{\frac{8K}{27\varepsilon A} g_0^3} \tag{3-2}$$

when the system becomes unstable and the movable plate suddenly collapses. This formula gives the static pull-in condition and a further developed dynamic model for the parallel-plate actuator can be found in [3.11].

However, for the multi-step actuator, the suspended plate shape is more complex. The linear approximation for 1-D model to calculate the pull-in voltage is not accurate for the 3-D structure of the multi-step actuator. So a numerical simulation method is employed by using the finite-element method software ANSYS to simulate the design. An iterative methodology is utilized to model the mechanical and electrical behaviors as shown in Figure 3.4.

The process begins with applying a voltage to an electrostatic field model. The electrostatic forces are calculated with the electrical field components. These forces are taken as loads to the mechanical structure model. Then the deformation of the suspended plate is solved. The deflected plate changes the gap between the electrodes, consequently changes the distribution of the electrical fields. So the electrical field model is re-built sequentially. Electrostatic forces are solved again. After the forces are updated, they are applied on the mechanical structure as loads again. The analysis iterates until equilibrium is reached.

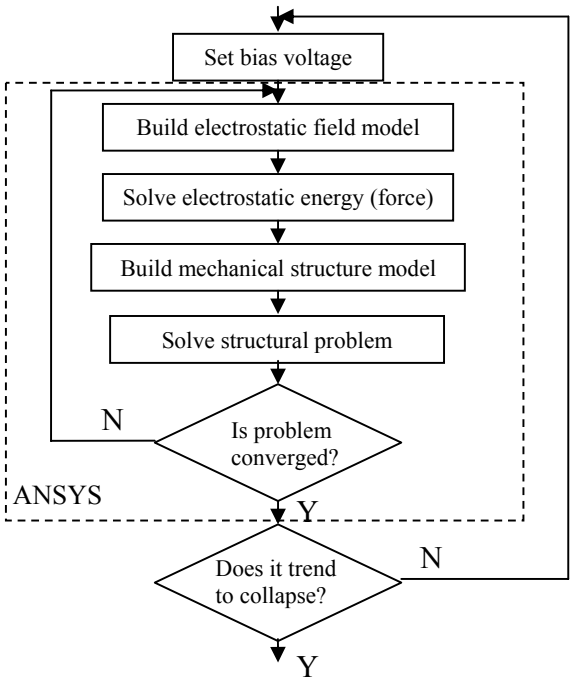

Figure 3.4 Multi-step actuator modeling flow chart.

With increasing voltage, the gap decreases until roughly close to 2/3 of g_o (the pull-in condition). The algorithm becomes divergent resulting from the pull-in condition. Hence, the simulation is stopped and the mechanical model is rebuilt.

Figure 3.5 shows the models and simulation results of (a) a multi-step actuator design, compared to (b) a single-step air gap actuator. The parameters of the designed structure are listed in Table 3.1. In this design, the step number is chosen as 2. A CPW line is designed on the bottom level of the substrate. On each side of the CPW line, a 2-step structures are designed. On the first step, 2 more electrodes are placed. On the top step, a metal membrane is deposited and patterned. The displacements are shown in Figure 3.5 (a). Figure 3.5 (c) shows the different deflections as a function of the applied voltage at different operations.

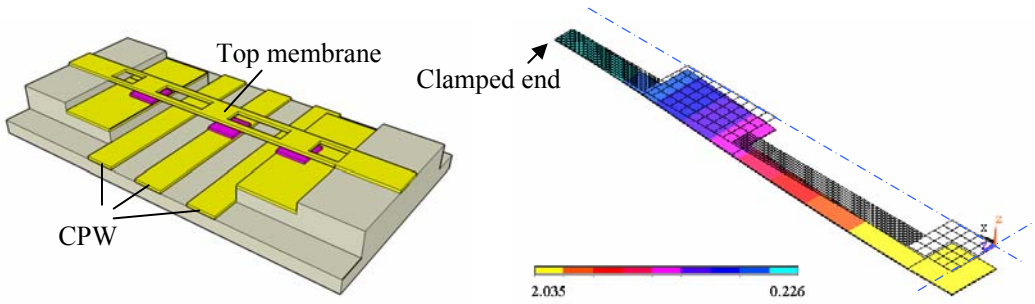

(a)

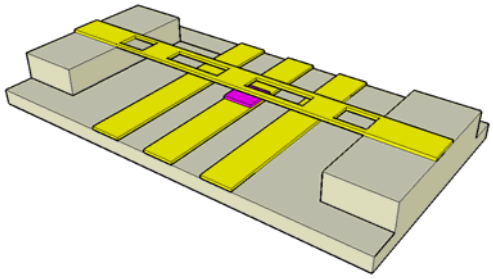

(b)

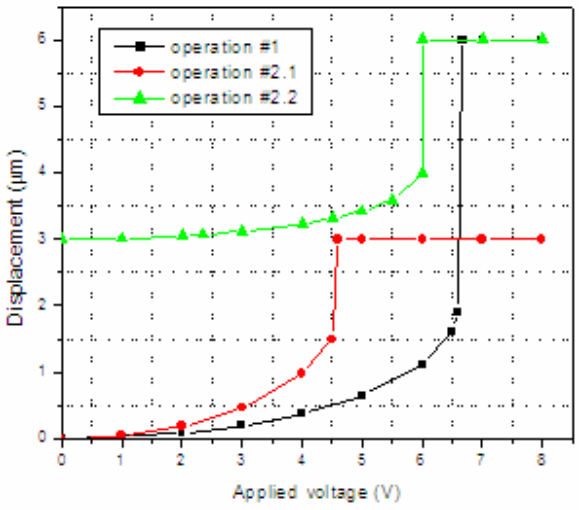

(c)

Figure 3.5 (a) 3-D drawings of multi-step actuators and simulation results for a 2-step actuator with 3 electrodes (a quarter of the plate is modeled due to symmetry) and (b) its counterpart sing-step actuator. (c) Deflections as a function of applied voltage curves for a 2-step actuator with different operations.

Table 3.1 Parameters for the actuator design in Figure 3.5.

Parameter name	Values
Electrode area	100 x 100 μm^2
Meander width	15 μm
Beam width	20 μm
Suspended plate thickness	1 μm
Step width	200 μm
Upper step height	3 μm
Lower step height	3 μm
Dielectric layer thickness	0.1 μm
Effective dielectric constant	6
CPW trace width	100 μm
CPW gap width	100 μm

The multiple electrodes and step structures give flexibility of operations to demonstrate the advantages of step actuators. First, if the bias voltage is only applied on the center electrode, the actuator behaves as a conventional single-step air-gap actuator, as shown in Figure 3.5 (b) and Figure 3.6. The displacement and voltage relationship is shown as the operation #1 curve in Figure 3.5 (c). The tuning range is less than 2 μm with a pull-in voltage about 6.5 V.

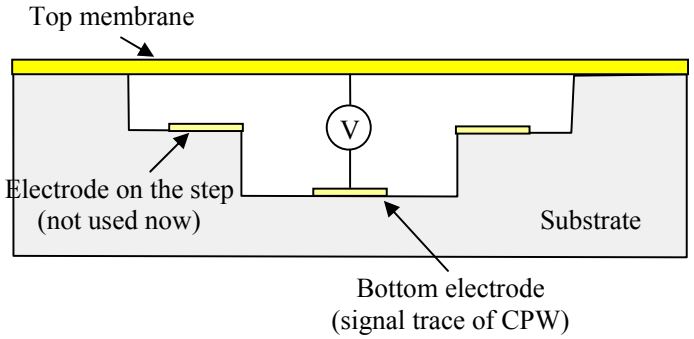

Figure 3.6 Single-step air gap operation mode. The bias voltage V is only applied across the top membrane and bottom electrode. The actuator works in the same behavior like a single step air gap actuator. The dielectric layers are not shown in this drawing.

For the 2-step operation, first a bias voltage V_1 is applied on the step electrodes and the top metal membrane as shown in Figure 3.7. Compared with the curve of operation #1 in Figure 3.5 (c), with the same bias voltage value, the curve operation #2 has larger deflection and smaller pull-in voltage, around 4.5 V. This is because that the facts that the air gap between the top electrode and the electrode on the step is smaller than that between the top and bottom electrode. The membrane is pulled at the both sides, so the two electrodes work simultaneously now.

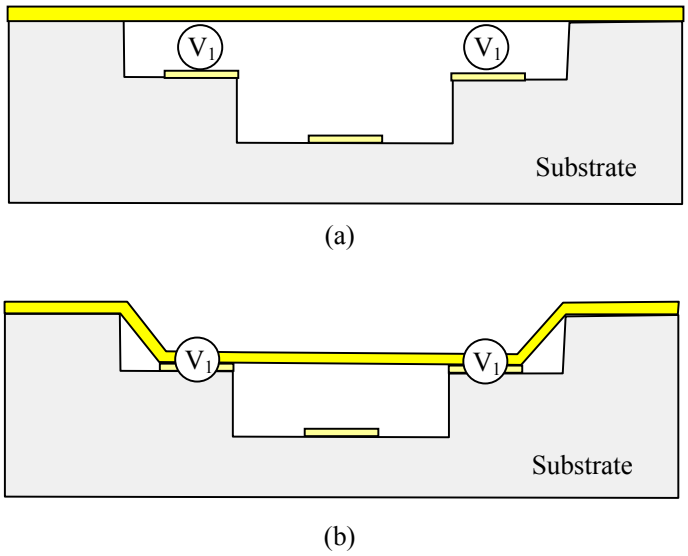

Figure 3.7 (a) Bias voltage V_1 is only applied on the top electrode and the electrodes on the first step. (b) After the bias voltage V_1 is larger than pull-in voltage, the membrane is fully pulled down onto the step. The dielectric layers are not shown.

When the first section of the membrane reaches the pull-in condition and settles on the steps, another actuation voltage V_2 is applied on the center electrode. The membrane reaches the pull-in condition with a voltage of 6 V, as shown by the curve operation #2.2 in Figure 3.5 (c).

The side parts of the top membrane rest on the steps. Only the center part of the membrane is deformable. Now the center part of the top metal electrode and the bottom electrode can be considered as a single step air gap actuator. Hence, the shape of the curve operation #2.2 is quite similar as that of curve operation #1, because they both behave like a single step air gap actuator. The pull-in voltage now is higher than 4.5 V and less than 6.5 V, since the stiffness of the membrane is higher due to the shorter length of the beam and the air gap is only half of that in Figure 3.6.

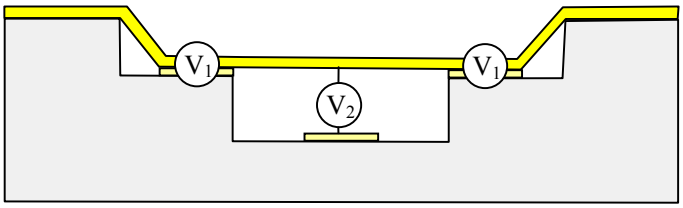

(a)

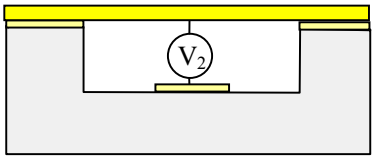

(b)

Figure 3.8 (a) The second bias voltage V_2 is applied on the center electrode. This bias voltage moves the center part of the membrane. (b) An equivalent mode of the structure in (a).

Figure 3.5 to Figure 3.8 demonstrate the advantages of a multi-step actuator because they bring added flexibility of operation, more tuning ranges and more discrete capacitances than the single step actuator.

The parallel plate capacitance of the air gap actuator can be calculated by:

$$C = \frac{\varepsilon_0 A}{g + \frac{t_d}{\varepsilon_r}}$$

where A is the area of the parallel plate, g is the height of air gap, t_d is the thickness of the thin dielectric layer, ε_r is the dielectric constant of the dielectric layer. In this design (Table 3.1), the capacitor ratio can reach a maximum of 355.

The example shown here is simplified to clarify the advantages. For practical applications, actuators with more than two steps and complex structures can be designed. And the operation will be more complex than the example here. Here, the electrodes on the steps are controlled symmetrically. If bias voltage is only applied on one of the electrodes on the steps, say, the left one, the behavior of the actuator will be different and the varactor reaches different values. Hence, the multi-step actuator structure makes system operation more flexible and capable.

3.1.2 Fabrication and Results

The fabrication sequence for a 3-step actuator is shown in Figure 3.9. The process starts with a high resistivity (greater than 3000 Ω-cm) silicon substrate. The step structure is fabricated by iterative dry etch in reactive ion etch (RIE) with CF_4:O_2 (30:5) at 100 W RF power. A layer of aluminum is sputtered and patterned to define the transmission line and electrodes on steps. A thin layer (<2000 Å) of dielectric (plasma sputtered silicon nitride, at 10 mTorr, 150 W RF power) is deposited and patterned to insulate the CPW central conductor and electrodes from membrane. With

spin-on polymer as a sacrificial layer, an aluminum membrane layer is sputtered and wet etched. After the sacrificial layer was removed, the air-gap is formed.

The fabrication process is compatible with the CMOS fabrication. It can be integrated with conventional MEMS fabrication process as well. To demonstrate feasibility, we designed the mechanical structure with higher geometrical tolerances to reach high yield without optimization of processes.

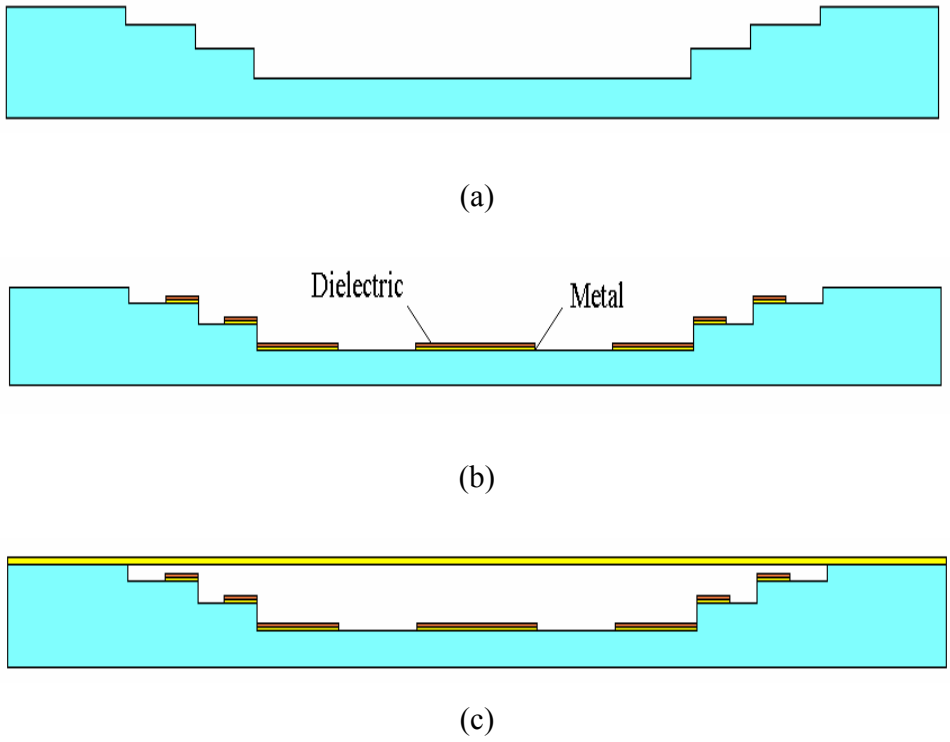

Figure 3.9 Main fabrication processes of the multi-step actuator. (a) Iteratively dry etched steps. (b) A CPW line, electrodes and dielectric layers. (c) Membrane formed after removal of sacrificial materials.

Figure 3.10 shows the microphotograph and profile of iteratively dry etched steps. The step heights are 1.24 μm, 1.16 μm and 0.95 μm. The aspect ratio of the step height to the step patio in this case is 1:200.

From the profiler, the second step surface seems rough. This was verified with scanning electron microscopic (SEM) photo, as shown in Figure 3.11. The rough surface may be due to the quality of photomasks therefore over-etching and iterative dry etch. This will introduce uncertainty in the nitride thickness required for the DC-insulation layer. To be safe, a thicker layer of nitride is deposited resulting in a high electrostatic actuation voltage.

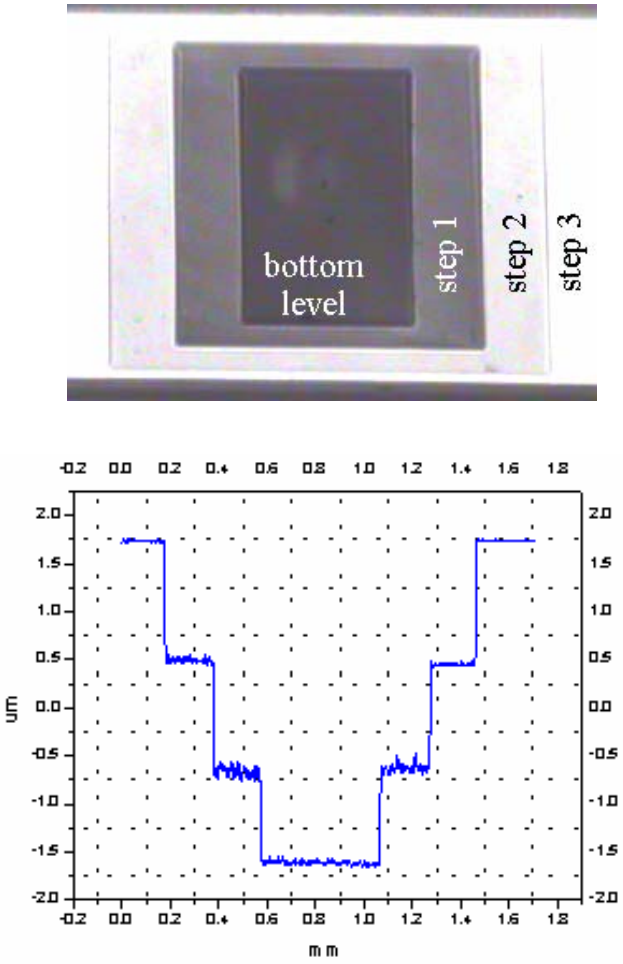

Figure 3.10 Microphotograph of an iteratively dry etched step structure and its profile measured by a surface profiler.

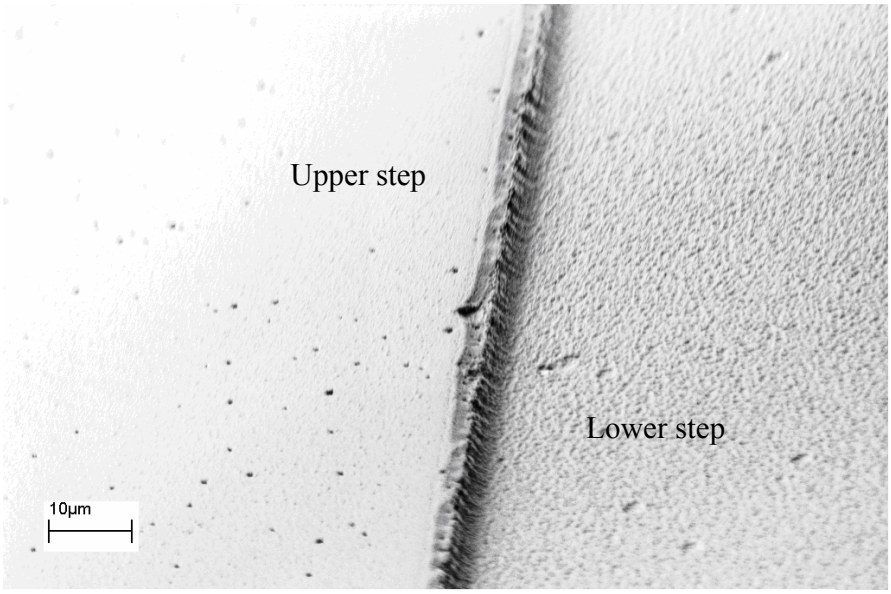

Figure 3.11 A SEM photo of the steps.

3.2 Enhanced Power Handling Capability of Multi-Step Actuator

Although RF MEMS capacitive membrane switches have shown excellent performance through DC to 40 GHz, there are still several challenges for these electro-mechanical structure based devices. Reliability and power handling capability of RF MEMS capacitive switches have been the main concerns [3.8, 3.9, 3.12].

RF power handling of capacitive RF MEMS switch is defined as the power at which the MEMS devices fails to operate properly. The failure results from the situation in which the high RF power actually creates enough potential to pull the membrane down into the actuated position even without applying a DC bias across the air gap.

A harmonic RF signal with a rms voltage of V_{RFrms} causes the membrane to deflect in a similar manner as an applied DC bias. Therefore, when applying this RF signal $V_{RFrms}\sqrt{2}\cos(\omega t)$ simultaneously to the DC bias signal, V_{DC}, the resultant electrostatic force can be written as:

$$F_e = F_{DC} + F_{RF} = -\frac{1}{2}\frac{\partial C}{\partial x}(V_{DC}^2 + V_{RFrms}^2) = \frac{\varepsilon A}{2x^2}(V_{DC}^2 + V_{RFrms}^2) \tag{3-3}$$

where C is the RF capacitance of the parallel plate capacitor and x the displacement of the suspended membrane. Hence, it is obviously that even if there is no DC bias voltage (*i.e.* V_{DC}=0) but V_{RFrms} is large enough, the RF signal can provide enough force to drag the membrane down then make the switch in malfunction.

Especially if the V_{RFrms} keeps increasing, it might be equal to or higher than the pull-in voltage given by Eq. (3-2), *i.e.*

$$V_{RFrms} = \sqrt{\frac{8Kg_0^3}{27\varepsilon A}} \tag{3-4}$$

In the real application, RF signals pass through the center trace of the CPW line underneath the membrane (switch). In a RF model, the input power can be considered as:

$$P_i = \frac{V_0^2}{2Z_0} \tag{3-5}$$

where Z_0 is the characteristic impedance.

It is assumed in this case that almost no power is reflected, because the membrane is still in the up state. Therefore, the minimum power to pull down the membrane is derived as

$$P = \frac{1}{Z_0}\frac{8Kg_0^3}{27\varepsilon A} \tag{3-6}$$

This power is referred as the minimum self-actuation power.

By increasing the total stiffness of the membrane (K), the self-actuation due to high RF power can be diminished, but cannot be completely overcome. However, higher K will induce other problems. Increasing K means increasing the pull-in voltage. It requires high bias voltage to control the switch, which is not permitted in many applications.

An alternative solution is to increase the gap height between the two parallel plates. However, this faces the same problem as increasing the stiffness K, since a larger air gap increases the pull-in voltage and requires a higher control voltage.

A lot of work have been pursued to try to solve this challenge of power handling capability limitation. Peroulis *et al*. designed a novel RF MEMS switch with a top electrode to increase the RF power handling capability [3.6] as shown in Figure 3.12. This extra electrode is electrically isolated from the switch and the CPW line underneath. The purpose of fabrication this top electrode is to introduce extra forces into the original electrostatic force and mechanical force balance system. This extra electrode can provide a pull-up force on the switch to compensate the effect by the RF input power. For example, it is assumed that the switch is initially in the down-state

position because of large RF power, i.e. the RF power is large enough to counteract the restoring force generated by the membrane. At this time, if a DC voltage is applied between the switch and the top electrode, the membrane will move up if this voltage is sufficiently high. Hence when large RF power passes through the CPW line, an extra bias voltage will be applied on the top electrode to counteract the force generated by the RF power. The RF power handling capability is increased then. Similar work has been done by Girbau *et al.* [3.13] based on the same idea of adding a third parallel plate and a second control voltage.

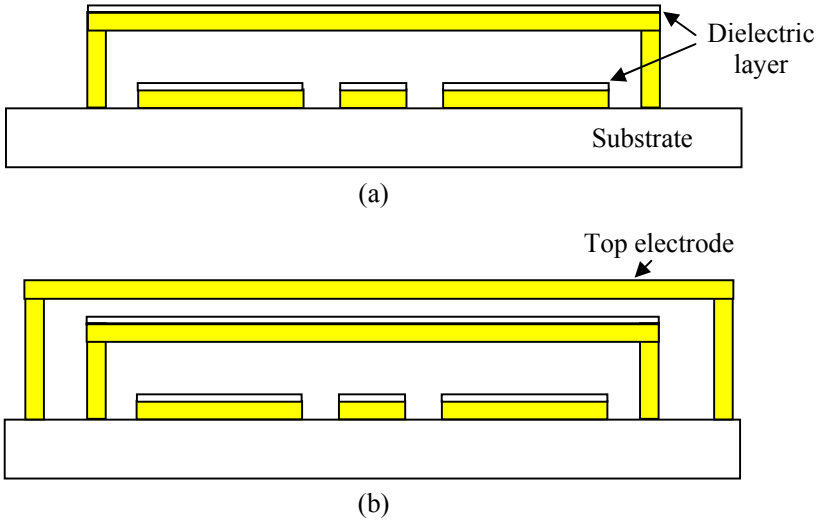

Figure 3.12 (a) A conventional RF MEMS capacitive switch design. (b) A top electrode is fabricated over the conventional design in [3.9].

The special structure of multi-step actuator makes it greatly improve the power handling capability of a capacitive RF MEMS switch. The air gap in a multi-step actuator is several times that in a single air gap actuator. Eq. (3-6) shows that the minimum self-actuation power is proportional to the cubic of air gap. Therefore, the

power handling capability of a multi-step actuator is much higher than that of a conventional single step air gap actuator. Meanwhile, the electrodes on the steps enable the pull-in voltage keep the same level as illustrated in Figure 3.5.

As shown in the literature [3.9, 3.13], the multi-step actuator is as well a more complex structure and has more bias control voltages than the single step actuator. However it wins by the advantages of more tuning ranges, wider tuning band, more discrete capacitances, higher capacitance ratio, and higher power handling capability.

3.3 Application of Multi-Step Actuator in Phase Shifter

3.3.1 RF MEMS Phase Shifters

Phase shifters are widely found in microwave systems. They play significant roles in communication, sensing, and defense applications. Novel RF MEMS devices have been developed for applications in phase shifters for years. Currently three major types of MEMS based phase shifters are widely used.

The first type is a MEMS based transmission-type phase shifter. Figure 3.13 shows a schematic of a transmission-type phase shifting network.

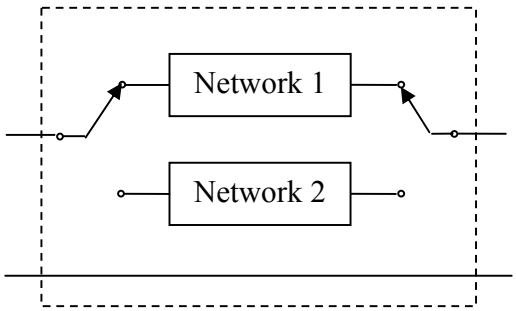

Figure 3.13 Schematic of a transmission-type phase shifter.

The commonly used devices as switches shown in Figure 3.13 are p-i-n diodes and MESFETs (metal-semiconductor Field Effect Transistors). MEMS switches compete with these solid state switches with their low power consumption, low loss, and high isolation. Pillans *et al.* have presented a 4-bit Ka-band phase shifter with insertion loss of 1.8 – 3 dB at 34 GHz [3.14]. Kim *et al.* have demonstrated a 4-bit switched-line phase shifter working from DC to 40 GHz [3.15]. Tan *et al.* have developed a 2-bit phase shifter working at X-band for 180° [3.16].

Another type of MEMS-based phase shifter is based on reflection phase shifting. An example of a reflection-type phase shifter is shown in Figure 3.14. For example, Malczewski *et al.* have developed such kind of phase shifters using MEMS switches for switching the lengths of terminated transmission lines connected to a Lange coupler [3.17].

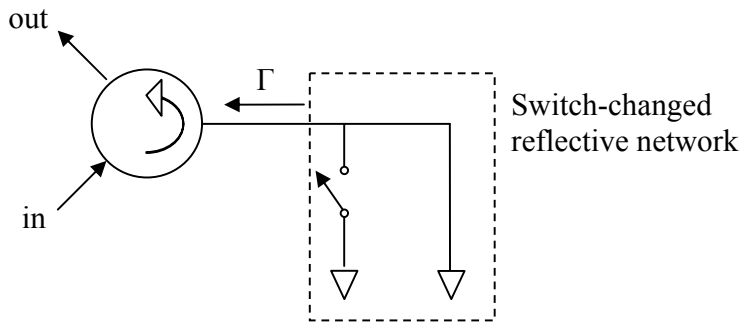

Figure 3.14 Schematic of a reflection-type phase shifter.

The third type of MEMS-based phase shifters is based on distributed MEMS transmission line (DMTL) phase shifting. This kind of phase shifter deploys a number of MEMS capacitive switches periodically along a transmission line, typically a

coplanar waveguide or a microstrip line, as shown in Figure 3.15. Barker *et al.* first presented a DMTL phase shifter with an insertion loss of 2.1 dB and a maximum phase shifting of 118° at 60 GHz [3.18]. Hayden *et al.* developed a CPW DMTL composed of 18 bridges and achieved a 0.7 dB insertion loss and a 123° phase shifting at 10 GHz [3.19]. Kim *et al.* presented a 2-bit DMTL phase shifter for V-band applications with an insertion loss of 2.2 dB at 60 GHz [3.20].

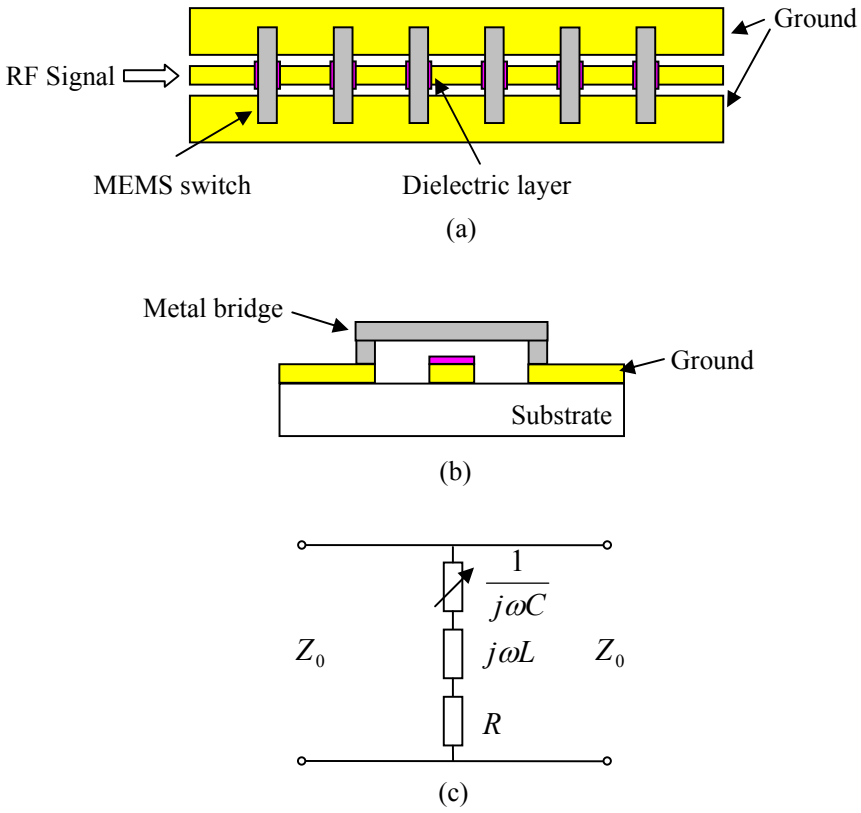

Figure 3.15 Distributed MEMS transmission line phase shifter. (a) Schematic of the DMTL. (b) Section view of a MEMS capacitive switch. It's obviously a single-step air gap actuator structure. (c) Circuit model for a MEMS capacitive switch over CPW line.

3.3.2 DMTL Phase Shifter with Single-Step Air Gap Actuator

The DMTL phase shifter can be modeled as a distributed circuit [3.21], incorporating a set of lumped elements into a transmission line. A wider bandwidth can be obtained by the distributed structure. The periodically loaded transmission line can be modeled as shown in Figure 3.16.

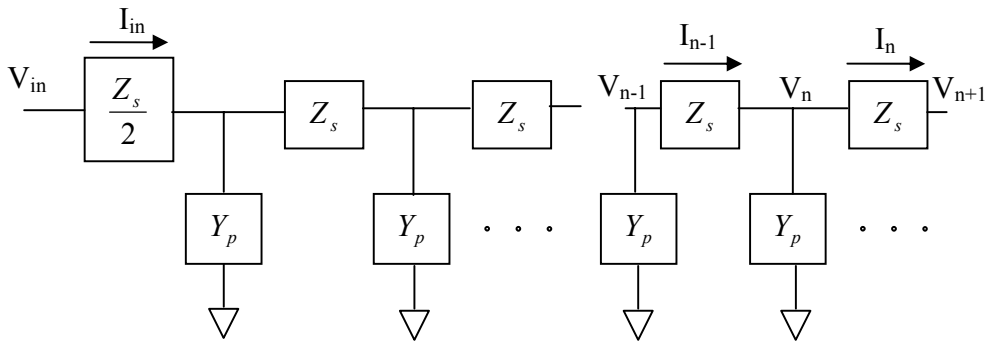

Figure 3.16 The periodically loaded transmission line is modeled as an ideal L-C synthetic (periodic) line.

A complex propagation constant is assumed as $\gamma = \alpha + j\beta$, where α and β are the attenuation per section and phase per section, respectively. Then a forward traveling wave can be presented by

$$V_{n+1} = V_n e^{-\gamma} \tag{3-7}$$

Meanwhile,

$$V_n = \frac{I_{n-1} - I_n}{Y_p},\ I_{n-1} = \frac{V_{n-1} - V_n}{Z_s},\ \text{and}\ I_n = \frac{V_n - V_{n+1}}{Z_s}$$

Hence, the equation that relates to propagation constant γ can be obtained

$$\cosh(\gamma) = \frac{e^{\gamma} + e^{-\gamma}}{2} = \frac{V_{n-1} + V_{n+1}}{2V_n} = 1 + \frac{Z_s Y_p}{2} \tag{3-8}$$

Next, the characteristic impedance at a point of symmetry is defined in order to obtain the correct impedance value. Hence, the characteristic impedance of the transmission line is defined at the input port or the middle of the line as

$$Z = \frac{V_{in}}{I_{in}} = \frac{V_{n+1/2}}{I_n} = \frac{V_{n-1} - 2V_n + V_{n+1}}{V_n - V_{n+1}} \frac{1}{Y_p} - \frac{Z_s}{2} = \frac{z_s e^{\gamma/2}}{2\sinh(\gamma/2)} - \frac{Z_s}{2} \tag{3-9}$$

Finally, the characteristic impedance of the periodically loaded transmission line is found by using the half-angle formula for the hyperbolic sine as

$$Z = \sqrt{\frac{Z_s}{Y_p}} \sqrt{1 + \frac{Z_s Y_p}{4}} \tag{3-10}$$

The characteristic impedance can be derived as

$$Z = \sqrt{\frac{L_t}{C_t}} \sqrt{1 - \frac{\omega^2 s^2 C_t L_t}{4}} = \sqrt{\frac{L_t}{C_t}} \sqrt{1 - \left(\frac{\omega}{\omega_B}\right)^2} \tag{3-11}$$

where $C_t = \sqrt{\varepsilon_{eff}}/(cZ_0)$ and $L_t = C_t Z_0^2$ are the length capacitance and inductance per unit length, respectively, s is the length of a section of unloaded transmission line with characteristic impedance Z_0 and effective dielectric constant ε_{eff}, $Z_s = j\omega s L_t$, $Y_p = j\omega s C_t$, and $\omega_B = 2/\left(s\sqrt{L_t C_t}\right)$ is the Bragg frequency, which is defined as the frequency at which the characteristic impedance goes to zero, indicating that no power transfer can occur at this frequency.

Baker [3.22] continued the work with transferring the distributed semiconductor devices along a transmission line [3.21] to the distributed MEMS switches on a CPW line.

In a DMTL phase shifter structure, a CPW line is periodically loaded with MEMS capacitive switches as shown in Figure 3.15. The MEMS switches can be modeled as shunt capacitors as shown in Figure 3.17, in which C_s is the shunt capacitance due to the MEMS capacitive switch, and s is the periodic spacing of adjacent switches.

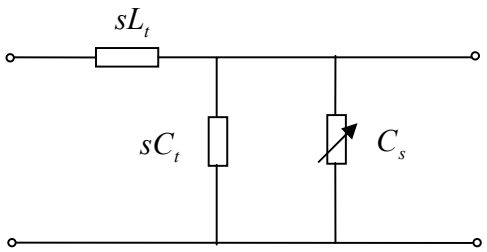

Figure 3.17 A schematic lumped element model of a DMTL unit section.

Now the characteristic impedance is derived as

$$Z = \sqrt{\frac{sL_t}{sC_t + C_s}} \sqrt{1 - \left(\frac{\omega}{\omega_B}\right)^2} \tag{3-12}$$

If Z=0, the Bragg frequency can be obtained as

$$\omega_B = \frac{2}{\sqrt{sL_t(sC_t + C_s)}} \tag{3-13}$$

Hence, the phase velocity is

$$\begin{aligned} \upsilon &= \frac{s}{\tau} = \frac{\omega s}{\beta} \\ &= \frac{\omega s}{\cos^{-1}(1 - 2\omega^2 / \omega_B^2)} \\ &= \frac{s}{\sqrt{sL_t(sC_t + C_s)}\left(1 + \frac{\omega^2}{6\omega_B^2} + \ldots\right)} \end{aligned} \tag{3-14}$$

where τ is the time delay per section. Finally, the phase shift per unit length is calculated from the change in the phase constant and is obtained by

$$\Delta\phi = \beta_1 - \beta_2 = \omega\left(\frac{1}{\upsilon_1} - \frac{1}{\upsilon_2}\right) \tag{3-15}$$

Eq. (3-14) and (3-15) illustrate how the distributed MEMS transmission line phase shifts. Once a bias voltage is applied to the MEMS capacitive switches, the switches will actuate and the air gap between the metal membrane and the CPW center conductor will be changed. By this method, the equivalent shunt capacitance C_s varies with the bias voltage. Hence, the bias voltage can control the phase velocity of the transmission line and thereby the phase shift.

3.3.3 Applications of Multi-Step Actuator Structure in DMTL Phase Shifters

From Eq. (3-14) and Eq. (3-15), a conclusion can be made that by varying the MEMS switch equivalent shunt capacitance, C_s, the phase velocity of the transmission line can be varied resulting in a variable delay line or true-time delay phase shifter. Obviously, the larger the variance of C_s, the larger the change of phase velocity, the larger phase shifting the DMTL can achieve.

In the previous section, the advantages of the multi-step actuator have been discussed. It can achieve a large capacitance ratio while keeping the pull-in voltage lower than a single air gap actuator. Hence, if a multi-step actuator is applied in the DMTL design, with the same control bias voltage, larger phase shift with a shorter transmission line will be achieved. Therefore, the insertion loss of the transmission line will be greatly reduced as well.

Since each MEMS capacitive switch can only provide binary phase shift, in a conventional digital phase shifter, the cascading method was used to increase phase shift over 360°. To reach higher resolution, more sections are required. However, dividing the transmission line into sections results in high reflection losses due to the impedance mismatch between sections.

The multi-step actuator enables multiple phase shifts with a single bridge and low actuation voltage. This novel structure reaches multiple levels of reactance with multiple steps. Therefore, resolution can be increased without generating excessive reflection losses, since the impedance does not change significantly along the transmission line. Compared to the DMTL phase shifter using single air gap actuator, the multi-step actuator makes the DMTL phase shifter compact with fewer bridges, which reduces transmission losses.

For example, an X-band DMTL phase shifter using a multi-step actuator structure is designed. It operates at the center frequency of 10 GHz. The designed X-band phase shifter has four 60 μm-wide bridges deployed along a CPW line, as shown in Figure 3.18. The spacing between adjacent bridges is 1000 μm. The center conductor of the CPW line is 100 μm wide. The bridge height varies from 3 μm to 2 μm, 1 μm, 0.7 μm and 0.5 μm. The simulation results are shown in Figure 3.19 and Figure 3.20. At 10 GHz, the insertion loss is less than -1 dB, and the return loss is less than -9 dB. With 4 bridges, a 64° phase shift is achieved. More phase shift can be achieved by simply adding more bridges.

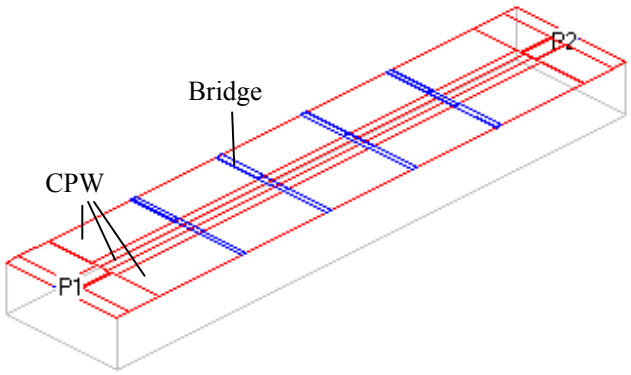

Figure 3.18 A FDTD model of the X-band DMTL phase shifter. 4 bridges are deployed along the CPW line.

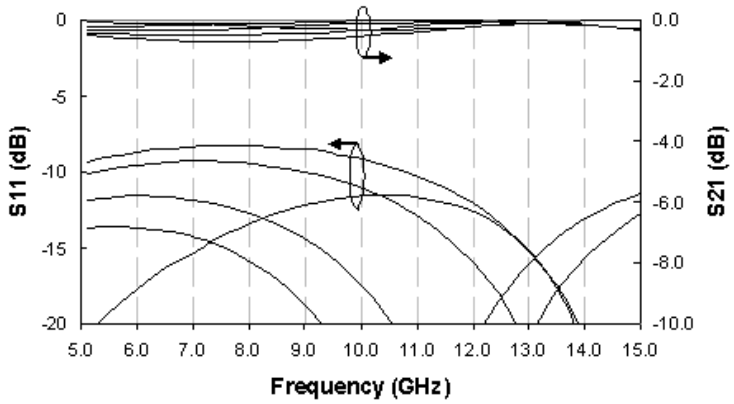

Figure 3.19 S-parameters of a X-band phase shifter using multi-step actuator based MEMS capacitive switches.

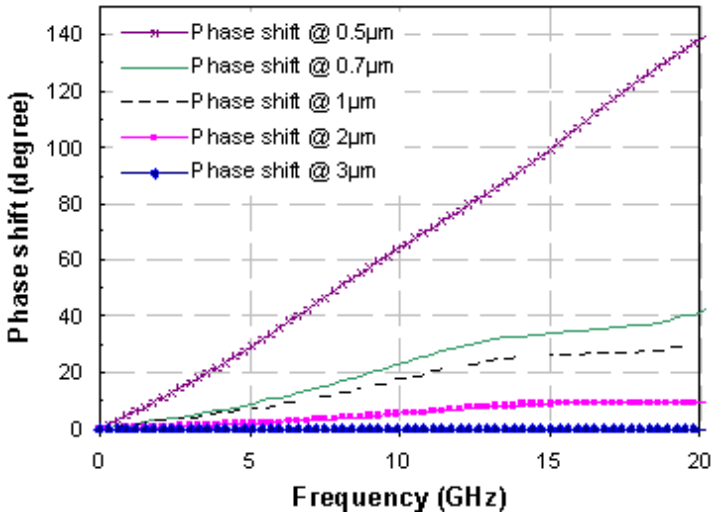

Figure 3.20 Phase shifting with the changes of all four MEMS capacitive switches' air gap heights.

As another example, in a discrete millimeter-wave beam steering application, a Ka-band 2-bit phase shifter was designed.

This Ka-band phase shifter has six 60-µm wide bridges distributed periodically over a CPW line with a spacing of 320 µm between the adjacent switches. The center conductor of the CPW line is 70 µm wide. The levels of bridge height are chosen to be 2.7, 1.7, 1.1 and 0.7 µm. The results are shown in Figure 3.21 and Figure 3.22. At the 35 GHz, S21 is less than 0.5 dB and S11 is less than -10 dB. The phase shift states at 35 GHz are 0°, 20°, 42° and 68° for a 2-bit four-level operation. If the number of switches is increased to 24, a total phase shift over 360° could be achieved.

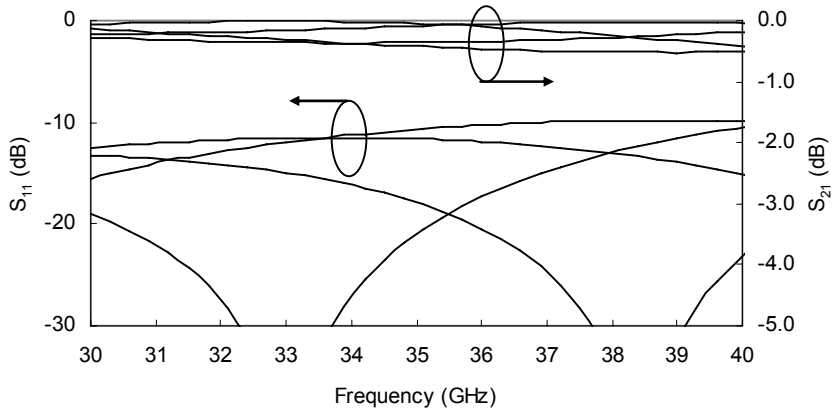

Figure 3.21 S-parameters for a 2-bit Ka-band phase shifter using multi-step actuator based MEMS capacitive switches.

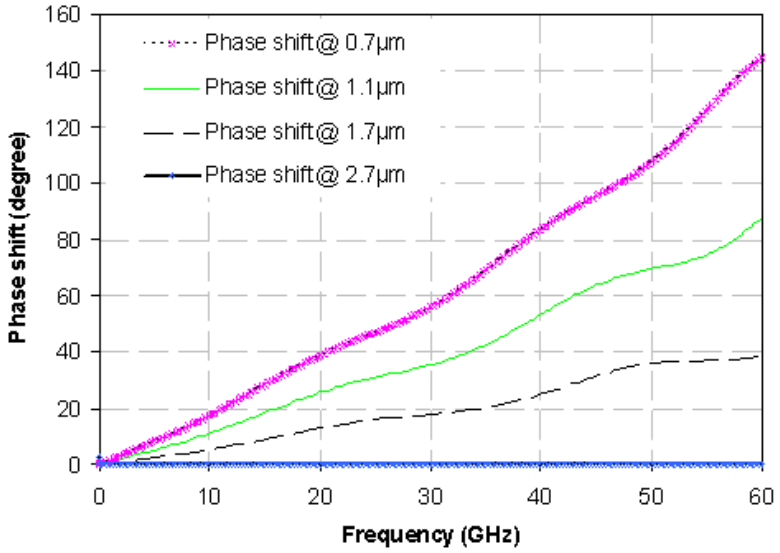

Figure 3.22 Phase shifting with the changes of all six MEMS capacitive switches' air gap heights.

Generally speaking, a multi-step actuator applied to a distributed MEMS phase shifter can greatly improve system performance, get bigger phase shift, and reduce

system loss, while keeping a lower pull-in voltage compared with conventional single air gap structure.

In this chapter, a novel multi-step actuator structure is presented. It can be used in RF MEMS switch designs, where they can be applied to millimeter-wave systems, such as distributed MEMS transmission line phase shifters. The multi-step structure enables the design of RF MEMS device with lower pull-in voltage, higher power handling capability, shorter transmission line length, lower losses, and larger phase shift.

CHAPTER 4

INTEGRATED RF MEMS AND MICRO HOT EMBOSSED DEVICES

The plastic micro hot embossing technique can be used to fabricate millimeter-wave components at light weight, low cost, and large production. RF MEMS devices developed in the past decades have proven their merits in competing with solid state semiconductor active devices. However, integration of the plastic micro hot embossed components and RF MEMS devices has not been demonstrated. This chapter covers the effort to implement the third objective of this dissertation of developing an integrated millimeter-wave system combining plastic micro hot embossed components, RF MEMS devices, and other individual devices together in a system for imaging, sensing, and communication applications.

First, a direct integration mechanism is dressed to combine the RF MEMS devices and micro hot embossed components. A W-band tunable iris waveguide filter prototype has been implemented. A MEMS bilayer cantilever switch has been designed and fabricated, which can be installed in an iris waveguide filter to get a desired band shift.

However, in many applications, it is difficult to directly integrate micro hot embossed components, RF MEMS devices, and other components together. Hence, a three-physical-layer architecture is presented. Benzocyclobutene (BCB) as a good

substrate material and transition from a CPW to a rectangular waveguide are utilized in this 3-physical-layer architecture to help to integrate all the antenna layer (micro hot embossed devices), transmission layer (RF MEMS devices), and circuit layer (active components, and off-chip components).

4.1 Direct Integration of RF MEMS and Plastic Micro Hot Embossed Devices

In the previous chapters, the advantages of using the plastic hot embossing technique to fabricate millimeter-wave components have been demonstrated. The rapid development of RF MEMS in the past decades has shown a promising future of applying RF MEMS in millimeter-wave applications. Naturally, a question emerges: can RF MEMS devices be integrated with the plastic micro hot embossed components?

A prototype W-band tunable filter has been developed [4.1] to demonstrate how actuators can directly integrate with plastic micro hot embossed iris waveguide filter. For real applications, PolyMUMPs zipper actuators have been fabricated to be installed in a plastic micro hot embossed iris waveguide filter.

4.1.1 A Prototype of Integrated W-Band Tunable Filter

In millimeter-wave applications, tunable filter plays a key role, especially for multi-channel systems. The state-of-art tunable filters are usually implemented with solid-state varactors [4.2]. However, high losses, low signal-to-noise ratios, and limited linearity of this approach hindered their further applications. The emerging technique, RF MEMS, shows its potential capability to solve these challenges.

Liu *et al.* have designed and fabricated a tunable bandpass filter using distributed MEMS transmission lines (DMTL) [4.3]. The DMTL is a coplanar

waveguide periodically loaded with continuously-variable MEMS capacitors as introduced in the previous chapter. In [4.3], the DMTL sections are designed as resonators coupled together to form a bandpass filter as shown in Figure 4.1. The tunable filter had a 3.8% tuning range at 20 GHz and a minimum insertion loss of 3.6 dB.

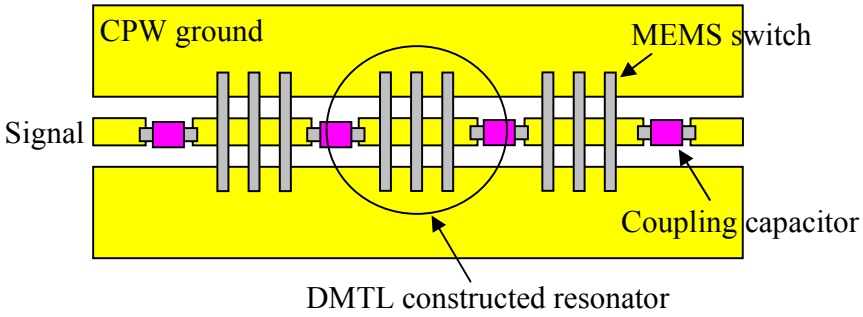

Figure 4.1 Layout of a 3-section tunable filter based on a distributed MEMS transmission line.

Entesari *et al.* demonstrated RF MEMS wide-band miniature tunable filters using a digital capacitor bank and microstrip lines for 6.5~10 GHz and 12~18 GHz ranges with a variable insertion loss in the range of 4.1 dB ~ 8.2 dB [4.4, 4.5].

Lee *et al.* reported a new type of RF MEMS tunable filter realized by reconfigurable inductors based on the reconfiguration of slow-wave coplanar waveguide (CPW) lines using multiple-contact switches, and RF MEMS capacitive shunt switches. The measured 3-dB cut-off frequency of the reconfigurable low-pass filter changes from 53 GHz to 20 GHz while maintaining Chebyshev low-pass prototype characteristics [4.6].

These tunable filters have demonstrated the feasibility of utilizing RF MEMS techniques to implement millimeter-wave tunable filters at the lower frequency ranges. However, they are based on microstrip lines or coplanar waveguide structures. Hence, they all suffer from high insertion losses and low power handling capability at higher frequencies.

Rectangular waveguide has the advantages of low attenuation and high power handling capability. A micromachined W-band iris waveguide filter with 3.5% bandwidth at 95 GHz using plastic hot-embossing technologies has previously been demonstrated [4.7], which inherits the high power handling capability. Therefore, integrated RF MEMS components with plastic micro hot embossed iris waveguide filter can be used to implement a continuous millimeter-wave tunable filter operating at 95 GHz. A prototype has been developed to demonstrate that air pressure actuated actuators can be directly integrated with a plastic micro hot embossed iris waveguide filter to implement a tunable filter.

Figure 4.2 shows an electrical model of a common 2-cavity iris waveguide filter and its corresponding equivalent circuit using impedance inverters and resonators. Based on this structure, deformable membranes on the top wall of the waveguide have been fabricated as shown in Figure 4.3. The membrane locates at the center of the resonator. The radius and height of the membrane can be altered.

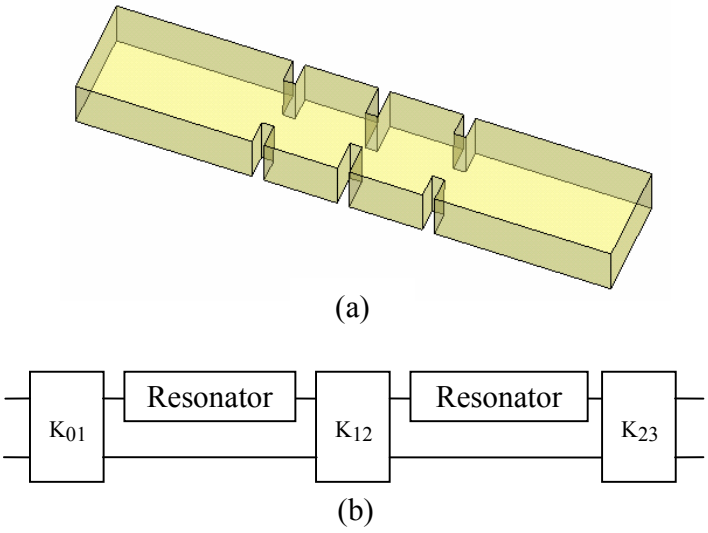

Figure 4.2 (a) An iris waveguide filter, and (b) its equivalent circuit using impedance inverters and resonators.

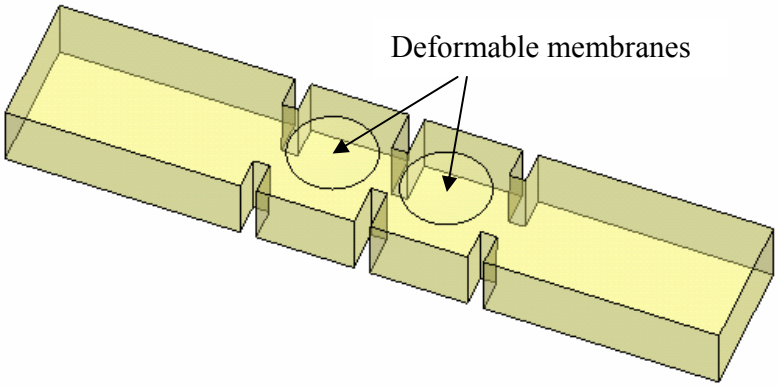

Figure 4.3 Deformable membranes are fabricated on the top wall of the waveguide.

In the prototype design, the deformable diaphragm is controlled by an external pump and this could be further improved by using built-in MEMS actuators, which will be discussed in the following section.

The fabrication process is very similar to the previous iris waveguide filter fabrication process. Figures 4.4 to 4.8 illustrate the main processes of the manufacturing steps. First the conventional iris waveguide filter cavity was hot embossed using two aluminum molds. The plastic replica was detached after hot embossing (Figure 4.4). A seed layer of 100 Å/1000 Å Cr/Pt was sputtered on the internal surfaces of the plastic iris waveguide filter cavity (Figure 4.5).

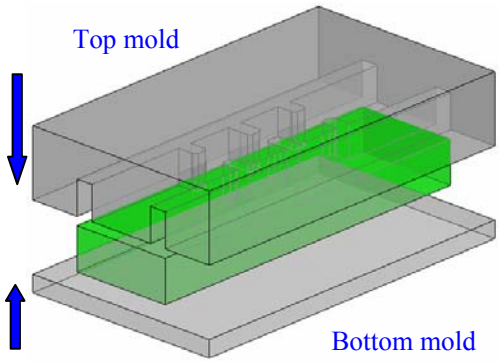

Figure 4.4 A plastic piece is hot embossed by two molds to define iris structures.

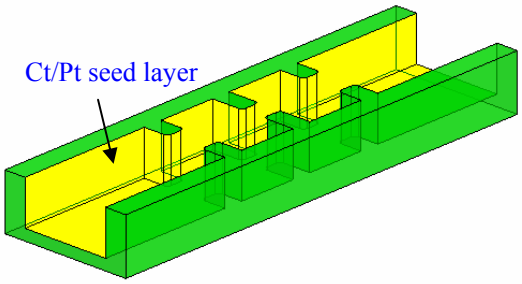

Figure 4.5 A Ct/Pt seed layer is sputtered on the inner surfaces of the plastic replica.

An aluminum thin shell was machined and two 1.6 mm diameter holes were drilled (Figure 4.6). The distance between two holes was determined by the two iris

waveguide filter resonators' lengths. Next a 25 μm-thick Kapton tape was bonded on the aluminum substrate to form the deformable membranes at the holes in the prototype. The same seed layer of 100 Å/1000 Å Cr/Pt was sputtered on the Kapton tape (Figure 4.7).

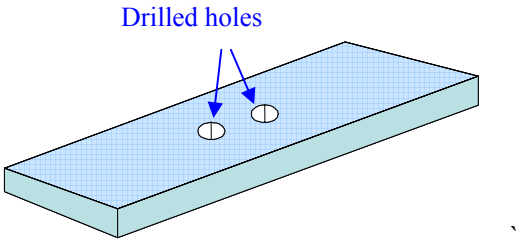

Figure 4.6 Two holes are drilled on a thin aluminum shell. This aluminum piece will be used as the top wall of the iris waveguide filter.

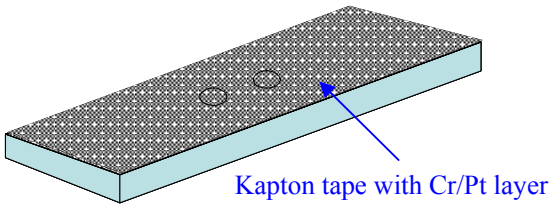

Figure 4.7 A piece of Kapton tape is coved on the aluminum shell. A Cr/Pt seed layer is sputtered on the Kapton tape.

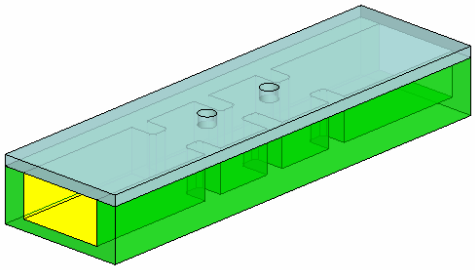

Figure 4.8 The aluminum shell is covered on the plastic replica. The surface with Kapton tape becomes the top wall of the waveguide now.

The aluminum substrate with a Kapton tape was put on top of the plastic replica to form a close cavity of the waveguide filter (Figure 4.8). Following assembly with 2 plastic flanges, a 3 μm-thick gold layer was selectively electroplated to seal and metallize the tunable iris waveguide filter.

When the pressure on the deformable membranes is changed, the shape of the membranes is altered. As a result, the electromagnetic wave distribution in the waveguide is disturbed as well. Finally, the original band-pass filter shape is changed and the pass band is shifted.

Figure 4.9 Measurement set up of the prototype tunable filter [4.1].

Figure 4.9 shows the testing setup of the tunable iris waveguide filter prototype. The tunable filter is connected to the standard W-band rectangular waveguides by

flanges connecting to a network analyzer. A pressure tube is connected to the top of the waveguide. A syringe pump is used to control the pressure on the membranes, then control the shape of the membrane in the cavity.

When a vacuum is applied, the deflection of the membrane is about +150 μm. When a pressure of 0.25 atm is applied, membrane deflection of -50 μm is expected. The deflection is measured by the microscope focusing and defocusing method. The measurement error is within ±10 μm. The measured insertion loss data in Figure 4.10 show an insertion loss of 2.36dB, 2.37dB, and 2.4dB when the membrane deflections are +150 μm, 0 μm, and -50 μm, respectively.

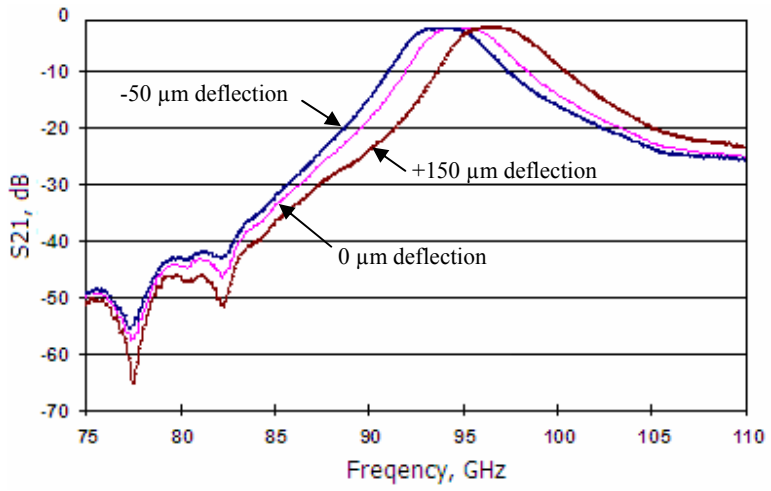

Figure 4.10 Measured insertion loss of the tunable filter.

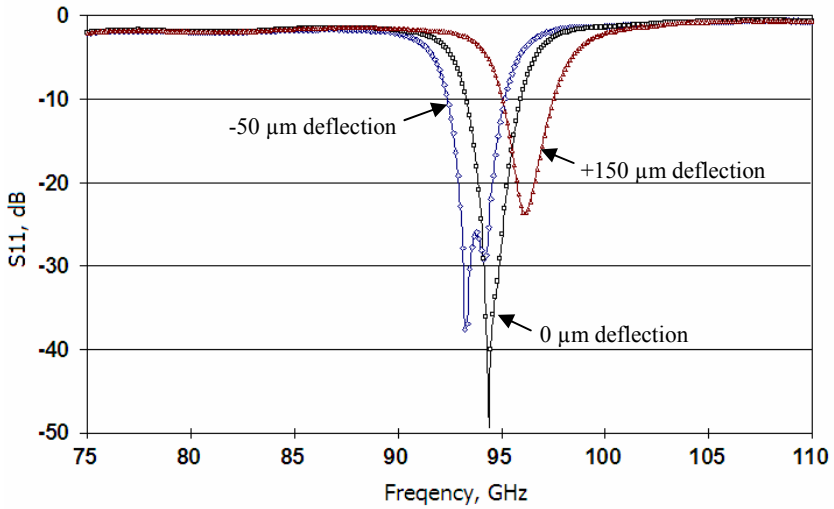

Figure 4.11 Measured return loss of the tunable filter.

The return loss shown in Figure 4.11 is always better than -15 dB and the center frequency shifts from 96.59 GHz to 94.79 GHz and then to 94.00 GHz. Therefore, the tuning range is 2.76% of the center frequency. The extra insertion loss is attributed to the gap between the devices under test (DUT) and the network analyzer adaptors as observed previously from a time domain plot [4.8], which has been discussed previously.

4.1.2 A W-band Tunable Filter Using MUMPs Fabricated MEMS Actuators

In the prototype of the tunable iris waveguide filter, the deformable membrane actuators are driven by air pressure. When the pressure is changed, the height and radius of the diaphragm is altered. This kind of actuation is not convenient in most systems. This section discusses the feasibility to implement an electrically controlled MEMS actuator tunable iris waveguide filter. The fundamental idea behind the operation is direct. MEMS actuators are installed on the top or bottom wall of the iris

waveguide filter. When applying a bias voltage on the MEMS actuators, they will change their shapes, as a result the electromagnetic field distribution inside the waveguide filter will be changed simultaneously. Therefore, the shape of the pass-band filter will be altered and shifted.

MUMPs® (Multi-User MEMS Processes) is a MEMS foundry service by MEMSCAP. In this dissertation, PolyMUMPs, a part of MUMPs, is applied to fabricate a MEMS zipper actuator as a prototype component used in the iris waveguide filter.

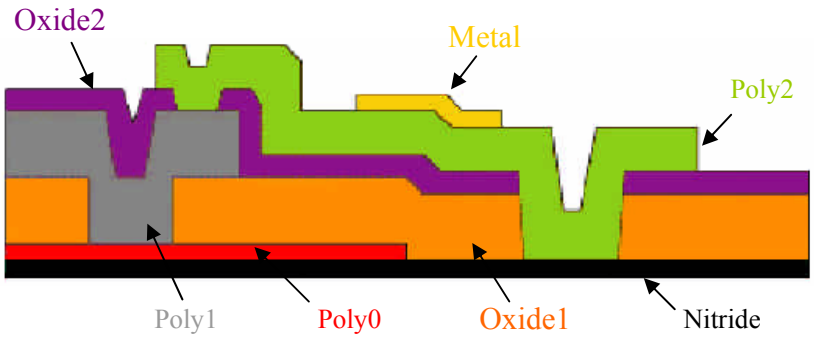

Figure 4.12 Cross section view of all seven layers of PolyMUMPs processing (not to scale).

MUMPs is a surface micromachining process composed of one metal layer, three structure layers (polysilicon), two sacrificial layers (silicon dioxide), and one dielectric layer (silicon nitride). Figure 4.12 shows the schematic cross section view of all MUMPs layers.

Utilizing PolyMUMPs standard micromachining processes, a MEMS actuator is designed and fabricated [4.9]. Figure 4.13 depicts the principle how the actuator has been fabricated and how it works.

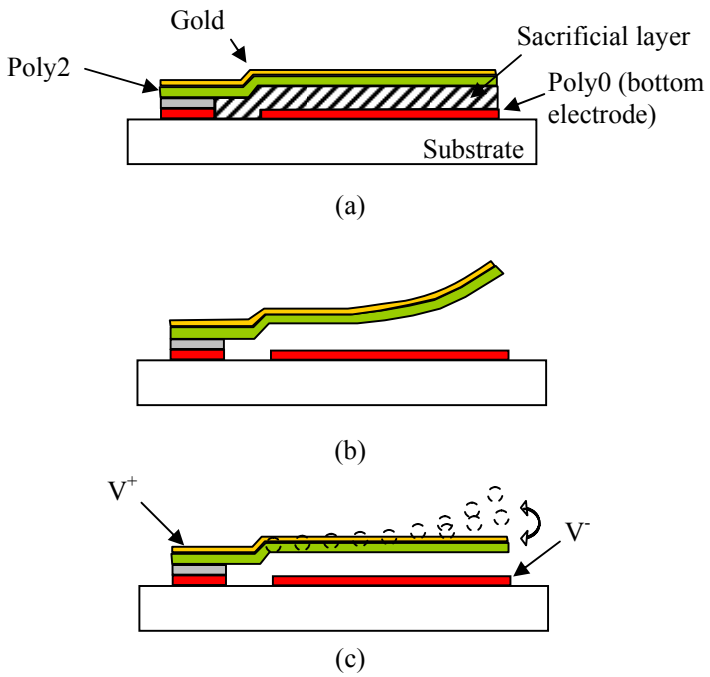

Figure 4.13 Fabrication and operation of a PolyMUMPs fabricated MEMS actuator. (a) A schematic structure of the actuator before releasing. (b) After releasing the chip, cure it in an oven at 200 °C for 10 minutes. At the room temperature, the cantilever will bend up. (c) Applying a bias voltage upon the cantilever and bottom electrode, the switch can move up and down with the voltage change.

First, the Poly0 layer is patterned as a bottom electrode of the actuator. A composite bilayer cantilever is patterned on top of the sacrificial layer over the bottom electrode. The composite bilayer structure is fabricated by the Poly2 layer and gold. Due to the different coefficients of thermal expansion of polysilicon and gold, during the fabrication, stresses will be induced. After releasing the sacrificial layer, the cantilever will naturally curve up owing to the residual stresses inside the bilayer cantilever. If a bias voltage is applied across the cantilever and bottom electrode, the

cantilever will actuate in behavior like a parallel plate air gap actuator. With changing the bias voltage, the beam will bend up and down.

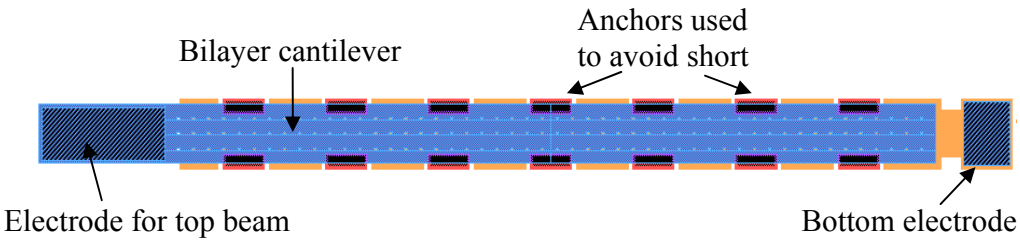

Figure 4.14 Top view of the layout design of a zipper actuator for PolyMUMPs fabrication.

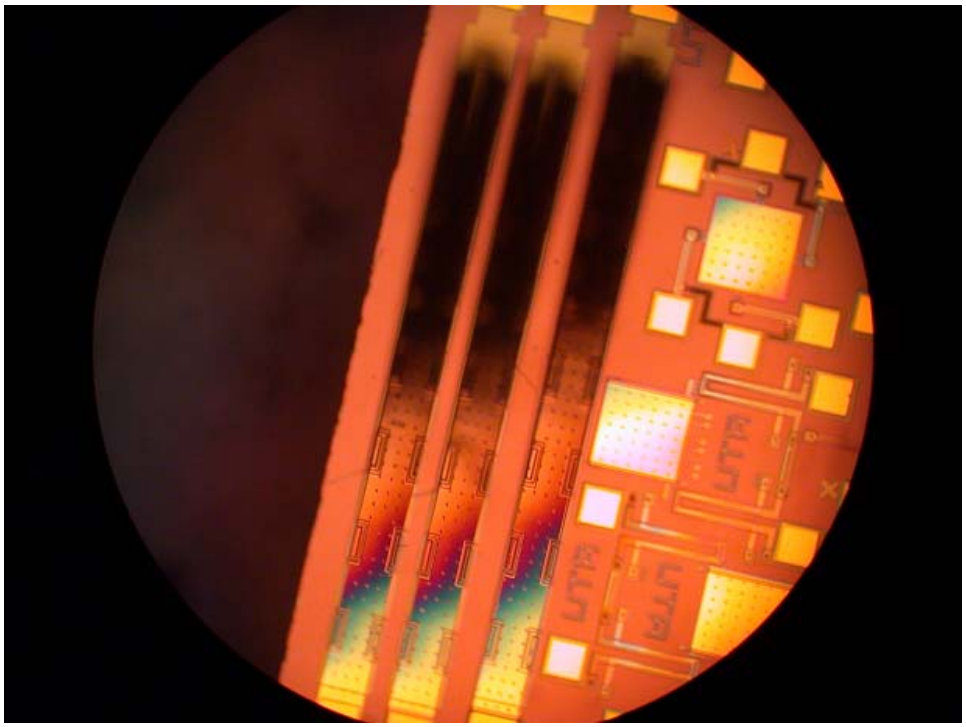

Figure 4.15 Microphotograph of 3 released and curved actuators (top view). The photograph is taken as focused on the middle part of the actuators. Hence, the curved tips and structures on the substrate are out-of-focusing and blurred.

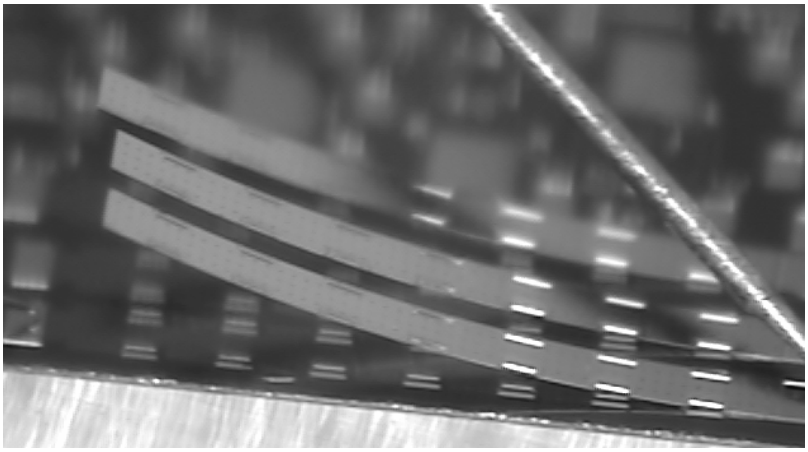

Figure 4.16 Microphotograph of the side view of the zipper actuators.

A more detailed analysis on the deformation of the composite bilayer cantilever has been done in order to help the synthesis of the actuator design.

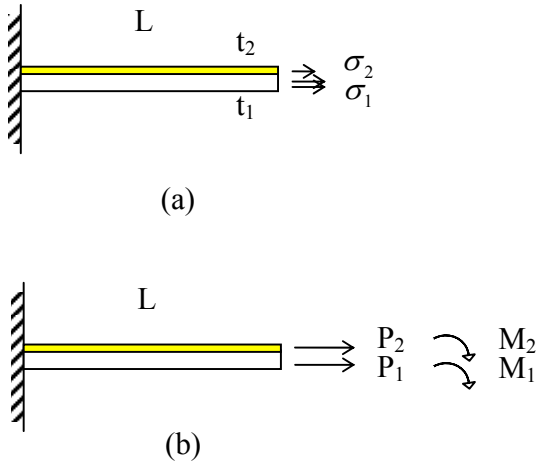

Figure 4.17 (a) A bilayer cantilever under uniform residual stresses σ_1 and σ_2. (b) The loadings applied on the bilayer cantilever after the release of the residual stresses.

In the actuator design, layer 1 (bottom layer) is the poly crystalline silicon (Poly2), layer 2 (top layer) is the gold layer. t_1=1.5μm, and t_2=0.5μm are the thicknesses of Poly2 and gold. After the PolyMUMPs fabrication processes, residual

stresses exist in the layers of gold and Poly2. The residual stress in gold is compressive stress, while the stress in Poly2 is tensile stress.

After releasing, due to the different residual strains ε_1 and ε_2 of the thin films, the bilayer cantilever experiences a bending moment by the residual stresses. Hence, there are resultant normal forces P_i and moments M_i applied on each thin film as shown in Figure 4.17 (b).

Since there are no external forces and moments acting over the films, this composite bilayer cantilever must satisfy $\sum P = 0$, and $\sum M = 0$.

$$P_1 + P_2 = 0 \quad \Rightarrow \quad P_2 = -P_1 = P \tag{4-1}$$

$$M_1 + M_2 = P_1 \frac{t_1}{2} + P_2\left(t_1 + \frac{t_2}{2}\right) \quad \Rightarrow \quad M_1 + M_2 = P\left(\frac{t_1 + t_2}{2}\right) \tag{4-2}$$

From the beam theory,

$$M_1 = \frac{E_1 I_1}{r}, \quad M_2 = \frac{E_2 I_2}{r} \tag{4-3}$$

where r is the radius of the curvature of the bilayer cantilever, E is the biaxial elastic modulus, and I is the moment of inertia. For the biaxial elastic modulus, $E = E_f/(1-\upsilon_f)$, where E_f is elastic modulus and υ_f is the Poisson's ratio of the thin film.

According to the compatibility equation, the total strain for film 1 and film 2 must be equal at the interface:

$$\frac{\sigma_1}{E_1} + \frac{P}{E_1 t_1 b} + \frac{t_1}{2r} = \frac{\sigma_2}{E_2} - \frac{P}{E_2 t_2 b} - \frac{t_2}{2r} \tag{4-4}$$

There are two equations for two unknowns P and r. The expression for the curvature, $k = 1/r$, is derived in [4.10]:

$$k = \frac{1}{r} = \frac{6b^2 E_1 E_2 t_1 t_2 (t_1 + t_2)(\frac{\sigma_2}{E_2} - \frac{\sigma_1}{E_1})}{(bE_1 t_1^2)^2 + (bE_2 t_2^2)^2 + 2b^2 E_1 E_2 t_1 t_2 (2t_1^2 + 3t_1 t_2 + 2t_2^2)} \tag{4-5}$$

or

$$r = \left(\frac{-\frac{1/m + n^3}{6(n + n^2)} - \frac{1 + mn^3}{6(1+n)} - \frac{n}{2} - \frac{1}{2}}{\sigma_1 - \frac{\sigma_2}{m}} \right) E_1 t_1 \tag{4-6}$$

where $m = E_2 / E_1$, $n = t_2 / t_1$.

Judy has built another model to solve the relationship between the cantilever deformation and residual stresses [4.11]. Instead of calculating the forces P_1, P_2, and moment M_1, M_2, for each material, an equivalent beam strength E_{eq} is calculated as:

$$E_{eq} = K \frac{E_2 b t_2^3}{12(1 + mn)} \tag{4-7}$$

where

$$K = 1 + 4mn + 6mn^2 + 4mn^3 + m^2 n^4 \tag{4-8}$$

$$m = \frac{E_1}{E_2} \quad and \quad n = \frac{t_1}{t_2}$$

Thus, a relation between stress-introduced internal force, P, and cantilever curvature, r, is obtained by

$$P = 2 \frac{E_{eq}}{tr} \tag{4-9}$$

where $t = t_1 + t_2$.

Substitute P into Eq. (4-4), we get

$$k = \frac{1}{r} = \frac{6(m\sigma_2 - \sigma_1)}{tE_2\left(3m + \frac{K}{n(1+n)^2}\right)} \tag{4-10}$$

With the curvature of the beam known, the tip deflection of the cantilever can be calculated from trigonometry. Therefore, the end deflection for a composite bilayer cantilever due to residual stresses is give by

$$\delta = r[1 - \cos(L/r)] \tag{4-11}$$

Table 4.1 List of symbols for bilayer cantilever model.

Symbol	Meaning
σ_1	Residual stress of Poly2
σ_2	Residual stress of gold
E_1	Biaxial elastic modulus of Poly2
E_2	Biaxial elastic modulus of gold
I_1	Moment of inertia of Poly2
I_2	Moment of inertia of gold
t_1	Thickness of Poly2
t_2	Thickness of gold
L	Length of the composite bilayer cantilever
b	Width of the composite bilayer cantilever

Table 4.2 Material properties of Poly2 and gold [4.10].

Property	Poly2	Gold
Young's modulus (GPa)	165	78
Poisson's ratio	0.23	0.35
Residual stress (MPa)	-8 (Tensile)	57 (Compressive)
Coefficient of thermal expansion (1/*K*)	2.8×10^{-6}	14.2×10^{-6}

For a cantilever beam length of 600 μm, and width of 240 μm, the calculated tip deflection of the cantilever are 41.5 μm and 41.2 μm according to Eq. (4-5) and Eq. (4-10), respectively.

For a tunable filter design, a large curvature is preferred after releasing the bilayer cantilever, because a wide actuation range of the actuator enables more capability of pass-band shifting of the filter. Pamula addressed the process of curing the bilayer cantilever at high temperatures to get a large curvature [4.11]. After putting the actuator in an oven at a high temperature for enough time, and upon returning to room temperature, the cantilever will be curled up more than its initial value. Hence, for a 600 μm long and 240 μm wide bilayer (Poly2 and gold) cantilever, although the initial tip deflection after releasing is around 40 μm, after curing it at a higher temperature, the tip deflection could be greater than 40 μm. Eq. (4-12) shows the temperature induced curvature as a function of cantilever geometry, material properties, and temperature difference between curing and room temperature [4.10].

$$k = \frac{1}{r} = \frac{6b^2 E_1 E_2 t_1 t_2 (t_1 + t_2)(\alpha_2 - \alpha_1)\Delta T}{(bE_1 t_1^2)^2 + (bE_2 t_2^2)^2 + 2b^2 E_1 E_2 t_1 t_2 (2t_1^2 + 3t_1 t_2 + 2t_2^2)} \quad (4\text{-}12)$$

where α_1 and α_2 are coefficient of thermal expansion of Poly2 and gold, respectively.

Taking the curing temperature as 114°C, and substituting the material properties in Table 4.2 into Eq. (4-12), we can get *k*=447. Hence, corresponding tip deflection is around 80 μm, which is most double of that before curing.

An HFSS model is used to simulate the performance of a tunable iris waveguide filter, in which PolyMUMPs fabricated zipper actuators are used. The 2-order bandpass filter is designed according to the section 2.3.1.2.

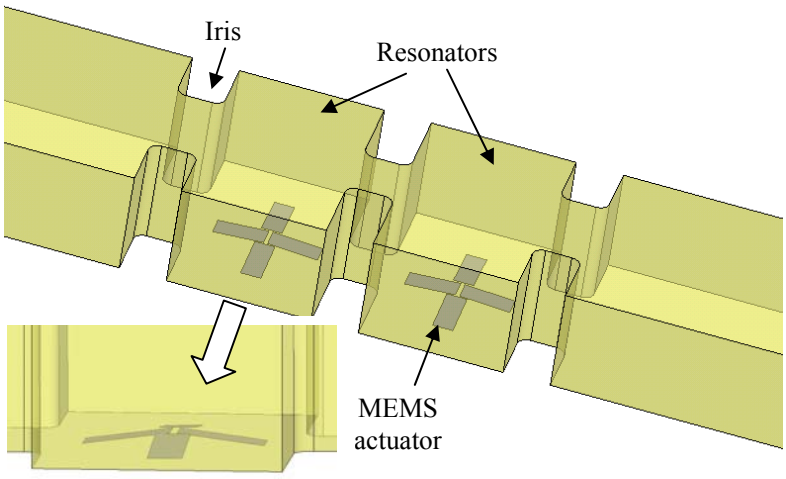

Figure 4.18 A 3-D view of the HFSS model of the tunable filter.

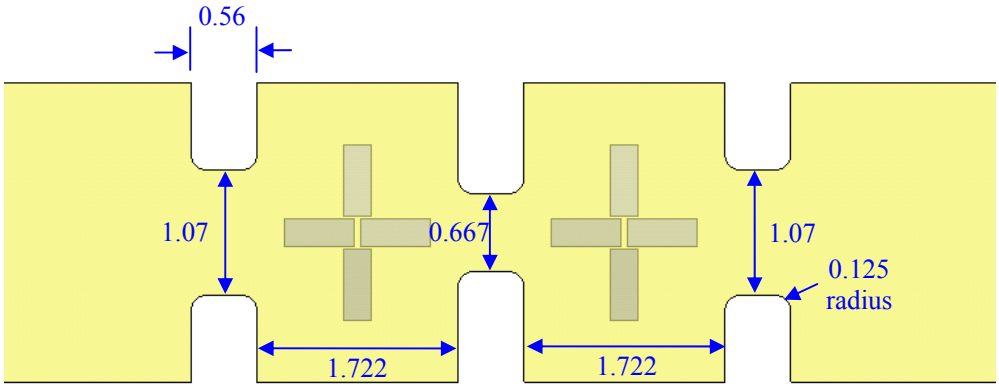

Figure 4.19 Top view of the model. All dimensions are in millimeter.

The tunable filter is designed for W-band. The opening of the waveguide is 2.54 mm x 1.27 mm for a standard WR-10 rectangular waveguide. All the MEMS actuators in the model have the same length of 600 µm and width of 240 µm. Figure 4.20 and Figure 4.21 show the performance of this tunable filter given different deflections of 40 µm and 80 µm.

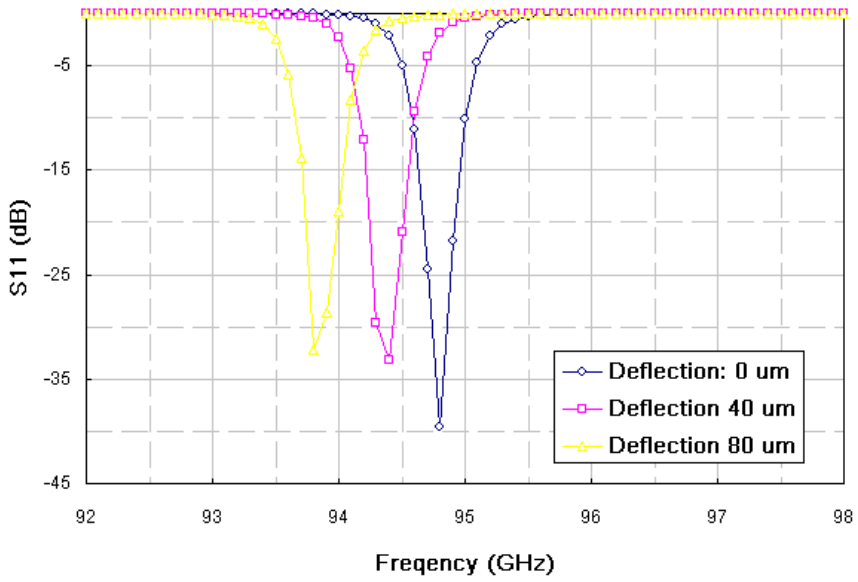

Figure 4.20 Simulated return loss of the tunable filter.

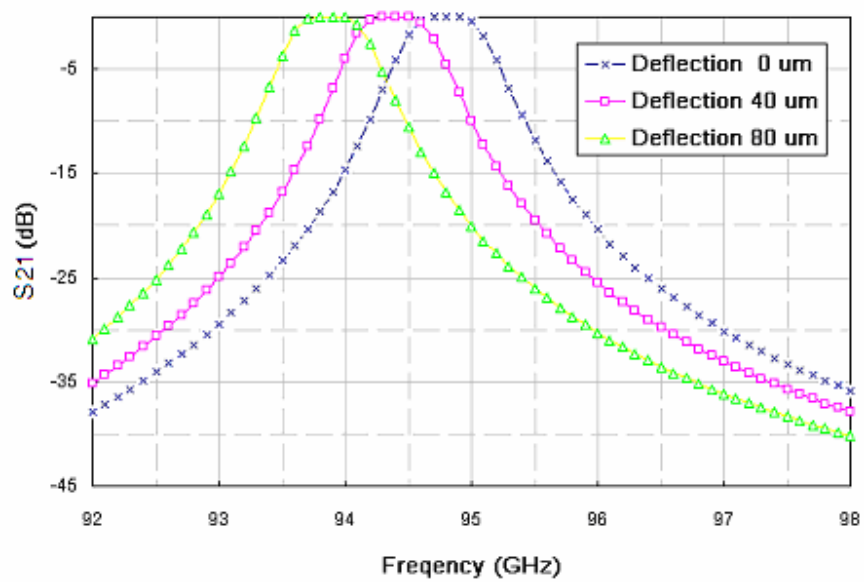

Figure 4.21 Simulated insertion loss of the tunable filter.

The return loss and insertion loss shown in Figure 4.20 and Figure 4.21 illustrate that with the increase of actuator tip deflection from 0 μm to 40 μm and to 80 μm, the bandpass filter center frequency is shifted from 94.8 GHz to 94.4 GHz and to 93.8 GHz. When the actuator deflection increases, the return loss in the pass-band increases as well due to the reflections caused by the curled actuators.

4.2 Utilizing BCB in Hybrid Substrate Structure

Millimeter-wave module usually consists of Si, GaAs, and InP devices on a single substrate with embedded passive components. In Chapter 3, the multi-step actuator structure is fabricated on a high resistivity (>3000Ω-cm) silicon substrate. However, in different applications, the substrate material might be bulk lossy silicon substrate (<100 Ω-cm) or other materials varying from silicon, quartz, GaAs, to new composite materials. Hence, when considering the integration of plastic micro hot

embossed components, RF MEMS devices with other individual components, the hybrid variation of substrate materials has to be taken into count.

In this dissertation, a new substrate material, BCB (Benzocyclobutene), is presented ([4.12], [4.13]). Its performance is investigated and its application in the integration is discussed.

Using BCB as the substrate material has many attractive properties. It has been demonstrated that the BCB polymer presented low insertion losses and loss tangent [4.14] at millimeter-wave frequencies. Without nitride as an isolation layer, BCB does not have the ion-drifting problem connected with copper as a conductive layer [4.15]. The lower processing temperature makes it possible for low thermal budget applications, such as existing CMOS processes. It is easy and cost-effective to control its thickness through the spin-on processes. Its resistance to common chemical agents, such as acids, makes the BCB processing compatible with most existing IC fabrication technologies. Further, the BCB material is versatile in micromachining techniques either as sacrificial layers [4.16] or mechanical structures. With all these advantages, BCB can potentially replace expensive low-doped or non-doped silicon wafers.

Many MEMS devices, such as varactors, switches, phase shifters, impedance tuners, and filters are based on CPW line. Hence, CPW lines with different lengths have been designed and fabricated on BCB to demonstrate the feasibility of using BCB as a RF MEMS device substrate. First, a 30-μm thick BCB layer is spun-on a low resistivity silicon substrate by an repeated spin-on process. Then a 1.5-μm thick copper layer is deposited on top of the BCB layer and patterned to define a CPW line as shown

in Figure 4.22. The center conductor width and air gap of the CPW line are fixed at 20 μm and 70 μm, respectively. The measured results are shown in Figure 4.23.

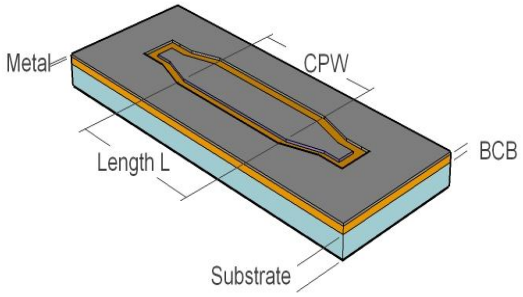

Figure 4.22 A CPW line on top of a 30-μm thick BCB layer.

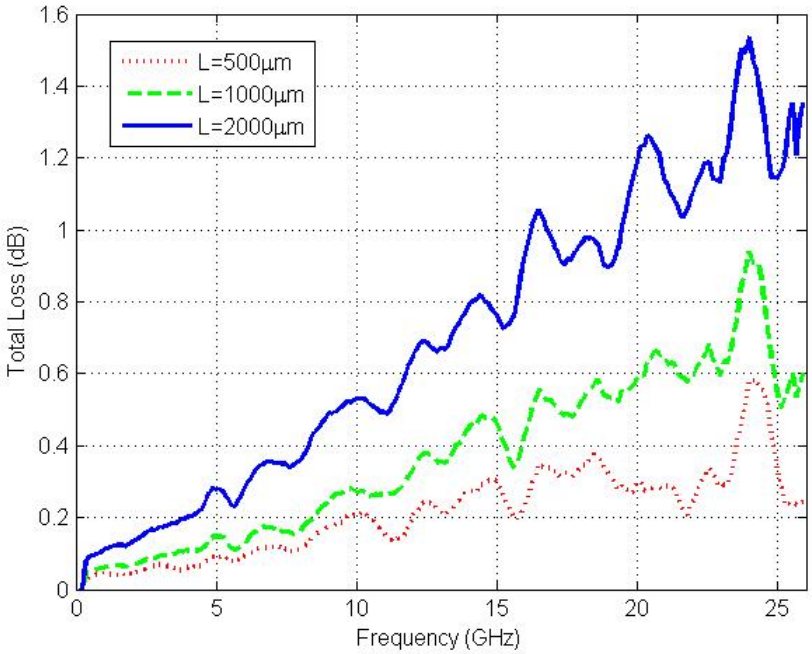

Figure 4.23 The performances of CPW lines on a 30-μm thick BCB layer with different lengths.

In this case, the measurement covers the frequency range from DC to 26 GHz. Grenier *et al.* investigated the performance of a CPW line on BCB from 0.4 GHz to 40 GHz [4.17]. Both ours and Grenier's work have demonstrated that BCB spun on other substrate materials forming a hybrid substrate can achieve good performance over a broad frequency range. Hence, the thick BCB layer can be used in the integrated system as shown in Figure 4.24.

After the active devices are fabricated on a substrate, which could be high/low resistivity silicon, quartz, GaAs, *etc.*), a thick BCB layer is spun on top of the substrate to form a hybrid substrate. Vias are fabricated to connect the active devices with other circuits within or on top of BCB. CPW lines and CPW based RF MEMS devices can be fabricated on top of the thick BCB layer no matter what the original substrate material is.

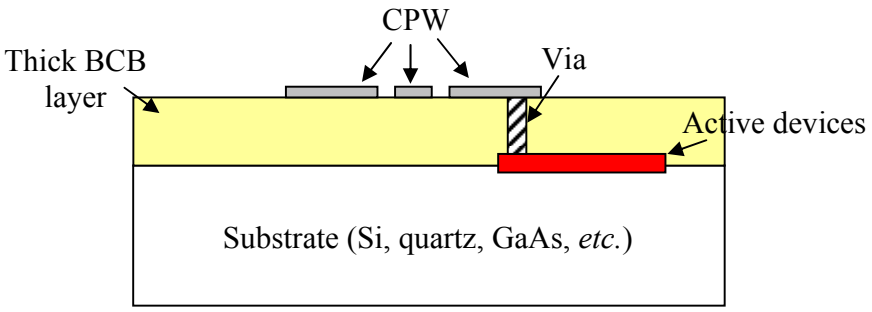

Figure 4.24 BCB utilized as a hybrid substrate material for integration purpose.

The integration mechanism illustrated in Figure 4.24 is significant to the integration of micro hot embossed components, RF MEMS devices, and other individual components, which will be discussed in Chapter 5.

4.3 CPW to Waveguide Transition

A large number of monolithic microwave integrated circuits (MMICs) for microwave and millimeter-wave systems require the transition between rectangular waveguides and different types of transmission lines. Generally, there are three different types of conversions: an E-plane probe transition [4.18], a ridge transition that is disclosed in U.S. Patent Nos. 2,825,876, 3,969,691, and 4,754,239, and the last type of conversion that was first reported in [4.19].

Among all these transitions, the ridge transition [4.20] is easier to be implemented by micro hot embossing and is more feasible to integrate CPW based MEMS devices.

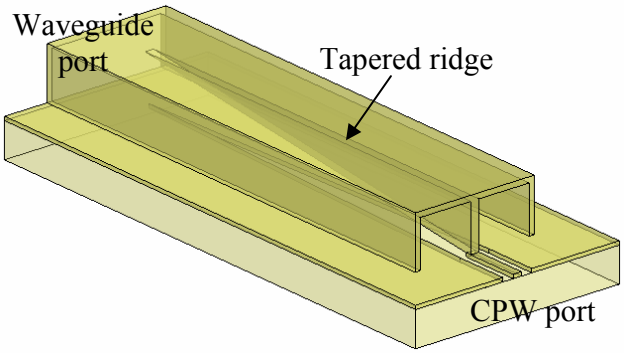

Figure 4.25 A transition from coplanar waveguide to rectangular waveguide.

Figure 4.25 is a schematic drawing of the transition from a coplanar waveguide to a rectangular waveguide. The tapered ridge protrudes from the top wall of the waveguide and extends down to the CPW metallization at the end of the taper. The ridge width is equal to the width of the CPW center strip conductor, *S*. As shown in Figure 4.26, on the planar circuitry, a non-radiating slot is etched which gradually tapers

to a width of $S+2W$, where S and W are the width of the CPW signal trace and space between signal trace and ground, respectively. The length of this non-radiating slot is exactly the same as that of the tapered ridge above it.

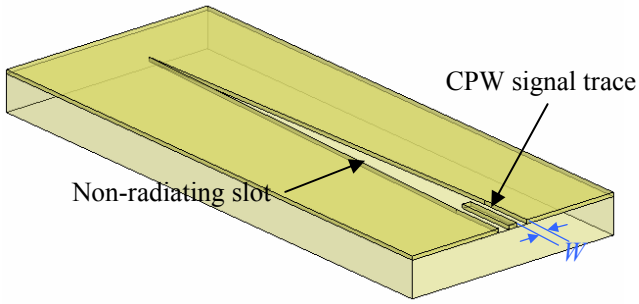

Figure 4.26 The non-radiating slot and the CPW line.

A FDTD model has been built to test the feasibility of this CPW to rectangular waveguide transition in the K-band. The simulation result is depicted in Figure 4.27.

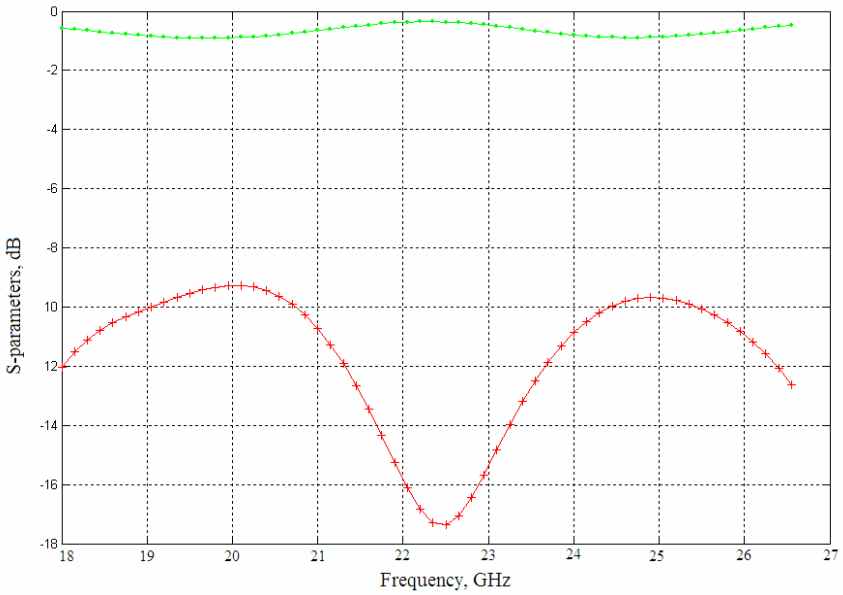

Figure 4.27 Simulated results of a CPW to rectangular waveguide transition.

Utilizing the designed CPW to rectangular waveguide transition, the integration of CPW based RF MEMS devices and micro hot embossed can be implemented as Figure 4.28 shown.

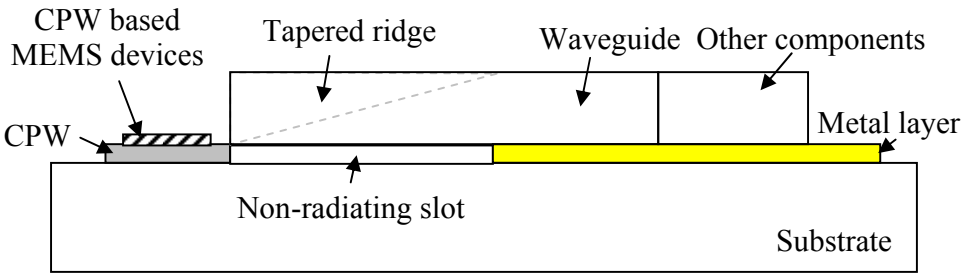

Figure 4.28 The transition from a CPW to a rectangular waveguide is utilized to integrate CPW based RF MEMS devices and micro hot embossed components.

Figure 4.28 depicts the application of the CPW to waveguide transition of integration. First, on the substrate, CPW, non-radiating slot, and metal layer as bottom wall of waveguide are patterned. Then CPW based RF MEMS devices are micromachined by surface micromachining techniques. Meanwhile, tapered ridge, waveguide, and other components such as iris waveguide filter, coupler, or slotted waveguide antenna are micro hot embossed together. Finally, the hot embossed part is bonded to the substrate. In this integration, the transition from CPW to waveguide plays a key role to transfer the signals from the planar circuit to the waveguide cavity.

In this chapter, the integration of micro hot embossed components, RF MEMS devices, and other individual devices is the main concern. Different integration means, mechanisms, and structures have been developed and investigated. A prototype tunable W-band filter has been developed and characterized to demonstrate the feasibility of direct integration of micro hot embossed components and MEMS actuators.

PolyMUMPs fabricated zipper actuators have been implemented to realize an electrically controlled tunable filter. BCB as a good substrate material is utilized in a hybrid substrate structure to integrate RF MEMS devices with other IC circuits. Finally an integration structure using a transition from a CPW to a rectangular waveguide has been developed, which can integrate CPW based RF MEMS devices with micro hot embossed component easily.

CHAPTER 5

FUTURE WORK

The front-end millimeter-wave components such as antennas and waveguides demand small feature sizes with smooth surfaces. This is difficult and expensive to make using traditional mechanical manufacturing techniques. Recently, with the fast development of semiconductor industry, micromachining processes have been employed to make components for millimeter-wave systems. Although many micromachined millimeter-wave components have been successfully demonstrated, they were not integrated systems. Therefore, integrated manufacturing for millimeter-wave systems becomes a great challenge. Compared to traditional systems, the integrated system has the advantages of low manufacturing and assembly cost, compact size, light weight, low loss, and low power consumption.

In Chapter 4, several integrated devices and integrated structures are developed and discussed. However, further integration is possible.

In this Chapter, a three-physical-layer architecture is presented, which provides a platform for system integration and batch processing. The architecture of a completely integrated millimeter-wave system has three layers: antenna layer, transmission line layer, and circuit layer. The antenna layer includes antennas, waveguides, splitters and other metallic components. This top passive front-end

antenna layer can be fabricated by the plastic micro hot embossing and electroplating technology. In the previous chapter, the advantages of the micro hot embossing technique for manufacturing millimeter-wave components have been demonstrated by successfully fabricated a waveguide, a waveguide filter, and a horn antenna. The transmission line layer will have CPW lines or microstrip lines for lower frequency range applications. This layer includes transmission line based RF MEMS components as well. These RF MEMS components include impedance tuners, phase shifters, varactors, switches, and filters. RF MEMS components can greatly improve system performance and cut down system power consumption. The bottom layer is the circuit layer in which the communication, data processing, and driver. Hybrid devices such as A/D, D/A, SAW etc are integrated to this circuit layer by using the flip-chip technology.

The batch processes to fabricate this 3-physical-layer integration architecture is illustrated from Figure 5.1 to Figure 5.5. First, the circuit layer in which the communication, data processing, driver, and IF circuits are fabricated on the substrate as shown in Figure 5.1. The substrate materials could be glass, quartz, silicon, GaAs, polymers etc.

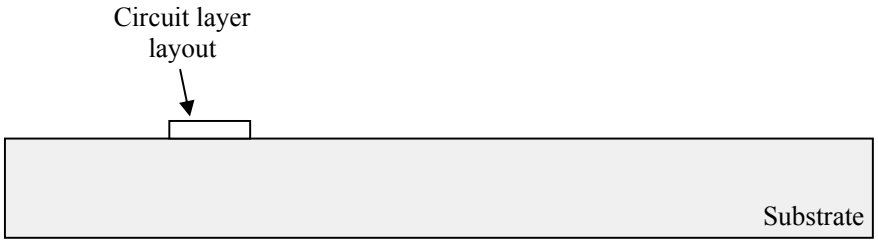

Figure 5.1 Circuit layer is first fabricated on the substrate.

Next, a thick layer of BCB is spun on the board and patterned. In order to introduce the RF waves and control signals to the devices which will be fabricated on and in the BCB, via holes/connections are manufactured (shown in Figure 5.2).

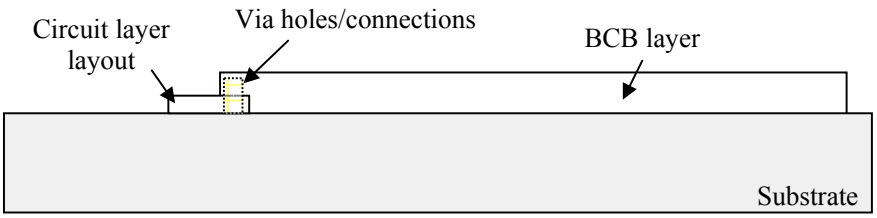

Figure 5.2 Spin-on BCB layer can be applied on variable substrate materials.

Figure 5.3 shows schematic structure of the transmission line layer. As defined previously, this layer includes transmission lines such as CPW lines, microstrip lines, and other transmission line based RF MEMS components. These RF MEMS components include surface micromachined MEMS capacitor [5.1], varactor [3.5], impedance tuner [5.2], filter [4.3], switch [5.3], and phase shifter [5.4]. Bulk micromachined RF MEMS components will be fabricated on the BCB as well. Meanwhile, the metal layout for CPW to waveguide transition as shown in Figure 4.26 will be patterned at the same time.

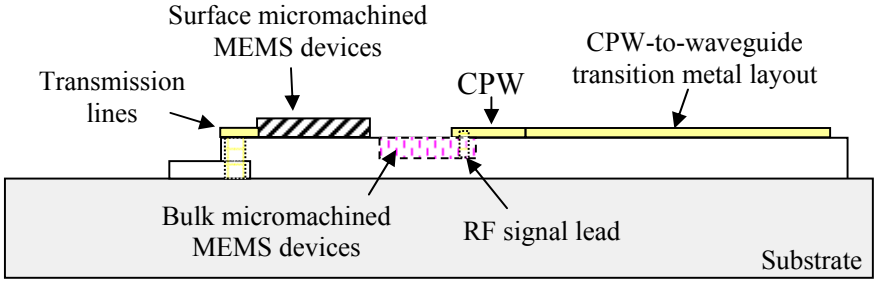

Figure 5.3 Schematic structure of transmission line layer.

Separately integrated manufactured front-end will be bonded to the board, as shown in Figure 5.4. The waveguide feed subsystem might include a waveguide splitter, a coupler, a circulator, a mixer, and a multiplexer etc. All the cavity based components including horn antenna or slotted waveguide antenna will be hot embossed at one time to get an integrated front-end.

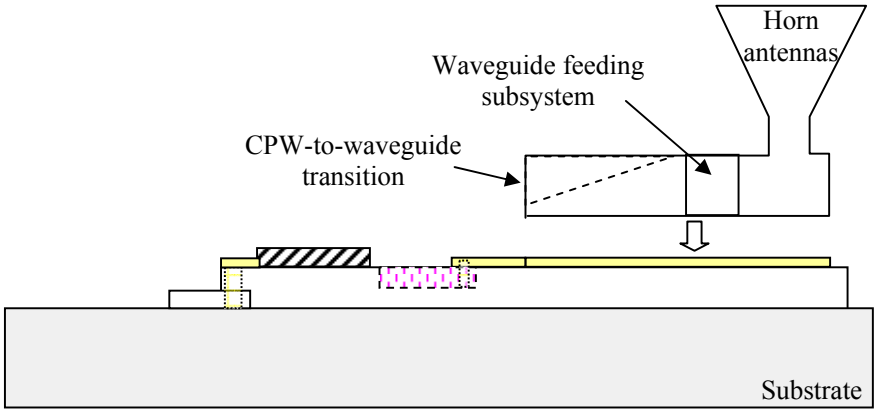

Figure 5.4 Antenna layer and its feeding subsystem are integrated into the system.

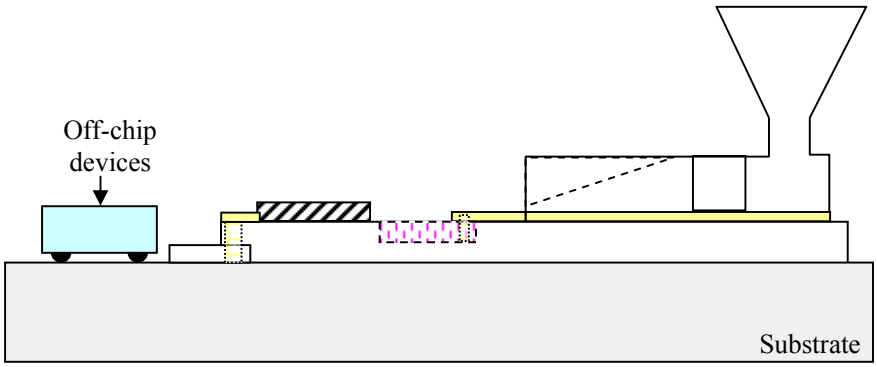

Figure 5.5 Off-chip devices are integrated using flip-chip technologies.

Finally, all off-chip devices are bonded by using flip-chip technologies. Figure 5.5 gives the whole schematic view of the integrated millimeter-wave system.

From Figure 5.1 to Figure 5.5, the main batch fabrication processes are depicted. However, the manufacturing details of each step are not specified. Hence, the future work should focus on the batch fabrication of the 3-physical-layer structure. A real application will be implemented to demonstrate the capability of this architecture for system integration.

APPENDIX A

TIP DEFLECTION CALCULATIONS OF A BILAYER CANTILEVER

Appendix A Content

MATLAB files used to calculate the composite bilayer cantilever tip deflection according to Eq. (4-5).

```
%-------------------------------------------
% Bilayer Cantilever Curvature Calculation
% Reference: Mechanical property measurement of thin-film gold
%                    using thermally actuated bimetallic cantilever beams

close all;
clear all;
clc;

format long;

%----------------------------------------
% film1: Poly2
% film2: gold

t1 = 1.5e-6;        % Poly2 thickness: 1.5 um
t2 = 0.5e-6;        % Gold thickness:  0.5 um
L = 600e-6;         % Cantilever length: 600 um
b = 240e-6;         % Cantilever width:  240 um

sigma1 = -8e6;     % Residual stress in Poly2: -8 MPa
sigma2 = 57e6;     % Residual stress in gold: 57 MPa

E1 = 165e9;     % Young's modulus of Poly2: 165 GPa
E2 = 78e9;      % Young's modulus of gold: 78 GPa

v1 = 0.23;    % Poisson's ratio of Poly2: 0.23
v2 = 0.35;    % Poisson's ratio of gold: 0.35

E1 = E1 / (1 - v1);
E2 = E2 / (1 - v2);

Numerator = 6*(b^2)*E1*E2*t1*t2*(t1+t2)*(sigma2/E2-sigma1/E1);
Denominator =
(b*E1*(t1^2))^2+(b*E2*(t2^2))^2+2*(b^2)*E1*E2*t1*t2*(2*t1^2+3*t1*t2+2*t2^2);
k = Numerator / Denominator   % Curvature of the cantilever
r = 1 / k     % Radius of the cantilever

delta = r * ( 1 - cos( L / r ))     % Tip deflection of the cantilever
```

```
%----- Results ------
%>>
%k =
%
%    2.311257507541106e+002
%
%
%r =
%
 %  0.00432664900703
%
%
%delta =
%
 %   4.153600658371096e-005
```

MATLAB files used to calculate the composite bilayer cantilever tip deflection according to Eq. (4-10).

```
%-------------------------------------------
% Bilayer Cantilever Curvature Calculation
% Reference: Self-adjusting microstructures (SAMS)
% Reference: Mechanical property measurement of thin-film gold
%                    using thermally actuated bimetallic cantilever beams

close all;
clear all;
clc;

format long;

%----------------------------------------
% film1: Poly2
% film2: gold

t1 = 1.5e-6;        % Poly2 thickness: 1.5 um
t2 = 0.5e-6;        % Gold thickness:  0.5 um
L = 600e-6;         % Cantilever length: 600 um
b = 240e-6;         % Cantilever width:  240 um

sigma1 = -8e6;     % Residual stress in Poly2: -8 MPa
sigma2 = 57e6;     % Residual stress in gold: 57 MPa
```

```
E1 = 165e9;     % Young's modulus of Poly2: 165 GPa
E2 = 78e9;      % Young's modulus of gold: 78 GPa

v1 = 0.23;    % Poisson's ratio of Poly2: 0.23
v2 = 0.35;    % Poisson's ratio of gold: 0.35

m=E1/E2;
n=t1/t2;
K=1+4*m*n+6*m*n^2+4*m*n^3+m^2*n^4;

Eeq = E2 * b * t2 ^ 3 * K / 12 / ( 1 + m * n );

r = (t1+t2)*E2*(3*m+K/(n*(1+n)^2))/(6*(m*sigma2-sigma1))    % Radius of the
cantilever

delta = r * ( 1 - cos( L / r ))     % Tip deflection of the cantilever

%----- Results ------
%>>
%r =
%
%   0.00436509746734
%
%
%delta =
%
%   4.117130850750301e-005
```

REFERENCES

[1.1] M.A. Alhaider, and A.A. Ali, "Experimental studies on millimeterwave and infrared propagation in arid land: the effect of sand storms," *Sixth International Conference on Antennas and Propagation, ICAP 89*, Vol. 2, No. 301, pp. 268-270, April 1989.

[1.2] F.T. Ulaby, T.F. Haddock, J.R. East, and M.W. Whitt, "A millimeterwave network analyzer based scatterometer," *IEEE Transactions on Geoscience and Remote Sensing*, Vol. 26, No. 1, pp. 75-81, Jan. 1988.

[1.3] J. P. Becker, Y. Lee, J. R. East, and L. P. B. Katehi, "A Finite Ground Coplanar Line-to-Silicon Micromachined Waveguide Transition," *IEEE Transactions of Microwave Theory and Techniques*, vol. 49, no. 10, pp. 1671-1676, October 2001.

[1.4] J. L. Hesler, K. Hui, R. K. Dahlstrom, R. M. Weikle, T. W. Crowe, C. M. Mann, and H. B. Wallace, "Analysis of an Octagonal Micromachined Horn Antenna for Submillimeter-Wave Applications," *IEEE Transactions on Antennas and Propagation*, vol. 49, no. 6, pp. 997-1001, June 2001.

[1.5] B. Shenouda, L. W. Pearson, and J. E. Harriss, "Etched-SIlicon Micromachined W-Band Waveguides and Horn Antennas," *IEEE Transactions on Microwave Theory and Techniques*, vol. 49, no.4, pp. 724-727, April 2001.

[1.6] J. W. Digby, C. E. McIntosh, G. M. Parkhrust, B. M. Towlson, S. Hadjiloucas, J. W. Bowen, J. M. Chamberlain, R. D. Pollard, R. E. Miles, D. P. Steenson, L. S. Karatzas, N. J. Cronin, and S. R. Davies, "Fabrication and Characterization of Micromachined Rectagular Waveguide Components for Use at Millimeter-Wave and Tetrahertz Frequencies," *IEEE Transactions on Microwave Theory and Techniques*, vol. 48, no. 8, pp. 1293-1302, August 2000.

[1.7] J. A. Wright, S. Tacic-Lucic, Y. C. Tai, W. R. McGrath, B. Bumble, and H. LeDuc, "Integrated Silicon Micromachined Waveguide Circuits For Submillimeter Wave Applications," *Symposium Proceedings: Sixth International Symposium on Space Tetrahertz Technology*, Pasedena, CA, pp. 387-396, March 1995.

[2.1] M. Krishnan, V. Namasivayam, R. Lin, R. Pal, and M. Burns, "Microfabricated reaction and separation systems," *Current Opinion in Biotechnology*, vol. 12, pp. 92-98, 2001.

[2.2] T. Schulte, R. Bardell, B. Weigl, "Sample acquisition and control on-chip microfluidic sample preparation," *JALA*, vol. 5, no. 4, September 2000.

[2.3] H. Schift, L. J. Heyderman, M. Auf der Maur, and J. Gobrecht, "Pattern formation in hot embossing of thin polymer films," *Institute of Physics Publishing, Nanotechnology*, vol. 12, pp. 173-177, 2001.

[2.4] G. B. Lee, S. H. Chen, G. R. Huang, W. C. Sung, Y. H. Lin, "Microfabricated plastic chips by hot embossing methods and their applications for DNA separation and detection," *Sensors and Actuators B: Chemical*, Volume 75, pp.142-148, April 2001.

[2.5] Jianqun Wang, Ying Cai and J.-C. Chiao, “A coplanar waveguide line based on polymer substrate,” *2005 TexMEMS, The VII International Conference on Micro Electro Mechanical Systems*, El Paso, TX, USA and Ciudad Juárez, Mexico. Sept. 21-22, 2005.

[2.6] W. R. McGrath, C. Walker, M. Yap, and Y. C. Tai, “Silicon micromachined waveguides for millimeter-wave and submillimeter-wave frequencies,” *IEEE Microwave and Guided Wave Letters*, vol. 3, no. 3, pp. 61-63, March 1993.

[2.7] J. W. Digby, C. E. McIntosh, G. M. parkhurst, *et al*., S. R. Davies, “Fabrication and Characterization of micromachined rectangular components for use at millimeter and terahertz frequencies,” *IEEE Transactions on Microwave Theory and Techniques*, vol. 48, no. 8, pp. 1293-1302, August 2000.

[2.8] B. A. Shenouda, L. W. Pearson, and J. E. Harriss, “Etched-silicon micromachined W-band waveguides and horn antennas,” *IEEE Transactions on Microwave Theory and Techniques*, vol. 49, no. 4, pp. 724-727, April 2001.

[2.9] J. P. Becker, J. R. East, and L. P. B. Katehi, “Performance of silicon micromachined waveguide at W-band,” *Electronics Letters*, vol. 38, no. 13, June 2002.

[2.10] Kraus Fleisch, *Electromagnetics with Application*, McGraw-Hill, 1999, pp. 456-468.

[2.11] Li-Wei Pan and Liwei Lin, “Batch transfer of LIGA microstructures by selective electroplating and bonding,” *Proceedings of IEEE Micro Electro Mechanical Systems Workshop*, pp. 259-264, Miyazaki, Japan, January 2000.

[2.12] G. L. Matthaei, L. Young, and E. M. T. Jones, *Microwave Filters, Impedance-Matching Networks, and Coupling Structures*, Artech House, 1980.

[2.13] N. Marcuvitz, *Waveguide Handbook*, Polytechnic Institute of New York, New York, 1986.

[2.14] G. V. Eleftheriades, G. M. Rebeiz, "High-Gain Step-Profiled Integrated Diagonal Horn-Antennas," *IEEE Transactions on Microwave Theory and Techniques,* vol. 40, no. 5, May 1992.

[2.15] Bassem Shenouda, "Etched-Silicon Micromachined W-Band Waveguides and Horn Antennas," Dissertation presented to the Graduate School of Clemson University, May, 1999.

[2.16] David M. Pozar, *Microwave Engineering*, Second Edition, John Wiley & Sons, INC. 1998.

[3.1] G. Rebeiz, *RF MEMS: Theory, Design, and Technology*, John Wiley & Sons, Inc., 2003.

[3.2] D.J. Young, B.E. Bover, "A Micromachined Variable Capacitor For Monolithic Low-noise VCO's," *IEEE Proceedings of the International Conference on Solid-state Sensors and Actuators*, Washington, DC, 86-89, 1996.

[3.3] A. Dec, K. Suyama, "Micromachined Varactor With Wide Tuning Range," *Electronics Letters*, Volume 33, Issue 11, Pages:922 – 924, 22 May 1997.

[3.4] J. Zou, C. Liu, and J. Schutt-Aine, "Development of A Wide Tuning-range Two-parallel-plate Tunable Capacitor For Integrated Wireless Communication Systems," *Int. J. RF Microw. Comput. Aided Des.*, vol. 11, pp. 322–329, Aug. 2001.

[3.5] J. Brank *et al*., "RF-MEMS Based Tunable Filters," *Int. J. RF Microw.Comput. Aided Des.*, vol. 11, pp. 276–284, Sept. 2001.

[3.6] L. Dussopt, G.M. Rebeiz, "An X- to Ku-band 3-bit Digital MEMS Varactor," *IEEE Microwave and Wireless Components Letters*, Volume 13, Issue 9, Page(s):361 – 363, Sept. 2003.

[3.7] Xiaobin Yuan, James C.M. Hwang, David Forehand, and Charles L Goldsmith, "Modeling and Characterization of Dielectric-Charging Effects in RF MEMS Capacitive Switches," *2005 IEEE MTT-S International Microwave Symposium Digest,* pp. 753- 756, 12-17 June 2005.

[3.8] S. Melle, D. Dubuc, K. Grenier, O. Vendier, J.L. Muraro, J.L. Cazaux, R. Plana, "Dynamic analysis of capacitive RF MEMS failure mode," Rapport LAAS N06032, Jan. 2006.

[3.9] D. Peroulis, S.P. Pacheco, L.P.B. Katehi, "RF MEMS Switches With Enhanced Power-handling Capabilities," *IEEE Transactions on Microwave Theory and Techniques*, Volume 52, Issue 1, Part 1, pp.59 – 68, Jan. 2004.

[3.10] K. Grenier, D. Dubuc, B. Ducarouge, etc., "High Power Handling RF MEMS Design And Technology," *18th IEEE International Conference on Micro Electro Mechanical Systems, 2005. MEMS 2005.* Pages:155 – 158, 30 Jan.-3 Feb. 2005.

[3.11] E. Saucedo-Flores, R. Ruelas, M. Flores, Y. Cai and J.-C. Chiao, "Dynamic Behavior Modeling of MEMS Parallel Plate Capacitors," *IEEE 2004 PLANS, Position Location and Navigation Symposium*, pp. 15-19, Monterey, CA. April 26-29, 2004.

[3.12] Clifford Fung, “Industry Study on Issues of MEMS Reliability and Accelerated Lifetime Testing,” *Microwave Journal*, Sep. 01, 2005.

[3.13] D. Girbau, N. Otegi, L. Pradell, A. Lazaro, “A MEMS Capacitor With Improved RF Power Handling Capability,” *2005 European Microwave Conference*, Vol. 3, pp. 1447-1450, Oct. 2005.

[3.14] B. Pillans, S. Eshelman, A. Malczewski, J. Ehmke, and C. Goldsmith, “Ka-band RF MEMS phase shifters,” *IEEE Microwave and Guided Wave Letters*, vol. 9, no. 12, pp. 520-522, 1999.

[3.15] M. Kim, J. hacker, R. Mihailovich, and J. DeNatale, “A DC-to-40 GHz four-bit RF MEMS true-time delay network,” *IEEE Microwave and Wireless Components Letters,* vol. 11, no. 2, pp. 56-58, Feb. 2001.

[3.16] G. L. Tan, R. Mihailovich, J. Hacker, J. DeNatale, and G. Rebeiz, “A Very-Low-Loss 2-bit X-band RF MEMS Phase Shifter,” in *Internation Microwave Symposium Digest. IEEE,* pp. 333-335, June 2002.

[3.17] A. Malczewski, S.E.B. Pillans, J. Ehmke, and C. Goldsmith, “X-band RF MEMS phase shifters for phased array applications,” *IEEE Microwave and Guided Wave Letters,* vol. 9, no. 12, pp. 517-519, Dec. 1999.

[3.18] N. Barker and G. Rebeiz, “Distributed MEMS True-Time Delay Phase Shifters and Wide-Band Switches,” *IEEE Transaction on Microwave Theory and Guided Wave Technology*, vol. 46, no. 11 part-2, pp. 1881-1890, Nov. 1998.

[3.19] J. Hayden and G. Rebeiz, “Low-Loss Cascadable MEMS Distributed X-Band Phase Shifters,” *IEEE Microwave and Guided Wave Letters*, vol. 10, no. 4, pp. 142-144, Apr. 2000.

[3.20] Hong-Teuk Kim; Jae-Hyoung Park; Sanghyo Lee; Seongho Kim; Jung-Mu Kim; Yong-Kweon Kim; Youngwoo Kwon, “V-band 2-b and 4-b low-loss and low-voltage distributed MEMS digital phase shifter using metal-air-metal capacitors,” *IEEE Transactions on Microwave Theory and Techniques*, Volume 50, Issue 12, Page(s):2918 – 2923, Dec. 2002.

[3.21] M. J. W. Rodwell, S. T. Allen, R. Y. Yu, M. G. Case, U. Bhattacharya, M. Reddy, E. Carman, M. Kamegawa, Y. Konishi, J. Pusl, and R. Pullela, “Active and nonlinear wave propagation devices in ultrafast electronics and optoelectronics,” *Proceedings of the IEEE*, vol. 82, no. 7, pp. 1037-1059, July 1994.

[3.22] N. S. Barker, “Distributed MEMS Transmission Line,” Dissertation of PhD in the University of Michigan, 1999.

[4.1] F. Sammoura, Liwei Lin, “A plastic tunable W-band fitlter,” *IEEE MTT-S International Microwave Symposium Digest 2006,* June 2006.

[4.2] I. C. Hunter and J. D. Rhodes, “Electronically tunable microwave bandpass filters,” *IEEE Transactions on Microwave Theory and Techniques*, vol. MMT-30, no. 9, pp. 1354-1360, September 1982.

[4.3] Y. Liu, A. Borgioli, A. S. Nagra, and R. A. York, “Distributed MEMS transmission lines for tunable filter applications,” *International Journal of RF and Microwave Compueter-Aided Engineering,* vol. 11, no. 5, pp. 254-260, September 2001.

[4.4] K. Entesari and G. Rebeiz, “A 12-18-GHz three-pole RF MEMS tunable Filter,” *IEEE Transactions on Microwave Theory and Techniques*, vol. 53, no. 8, pp. 2566-2571, August 2005.

[4.5] K. Entesari and G. Rebeiz, “A differential 4-bit 6.5—10-GHz RF MEMS tunable filter,” *IEEE Transactions of Microwave Theory and Techniques*, vol. 53, no. 3, pp. 1103-1110, March 2005.

[4.6] S. Lee, J. M. Kim, Y. K. Kim, and Y. Kwon, “Millimeter-wave MEMS tunable low pass filter with reconfigurable series inductors and capacitive switches,” *IEEE Microwave and Wireless Components Letters*, vol. 14, no. 10, pp. 691-693, October 2005.

[4.7] F. Sammoura, Y. Cai, C. Y. Chi, T. Hirano, L. W. Lin, and J. C. Chiao, “A micromachined W-band iris filter,” *The 13th International Conference on Solid-State Sensors, Actuators and Microsystems,* pp. 1067-1070, Seoul, Korea, June 5-9, 2005.*IEEE MTT-S International Microwave Symposium Digest,* vol.3, pp.1543-1546, New York 1995.

[4.8] Y. Cai, F. Sammoura, C.-Y. Chi, L. Lin, and J.-C. Chiao, “Micro Hot Embossed Plastic Millimeter-Wave Systems," *SPIE International Symposium on Microelectronics, MEMS, and Nanotechnology*, Australia, December 11 - 15, 2005.

[4.9] Daneshmand, M.; Mansour, R.R.; “Multi-port RF MEMS waveguide switch,” *IEEE MTT-S International Microwave Symposium Digest, 2005*, Page(s):935 – 938, 12-17 June 2005.

[4.10] V. K. Pamula, A. Jog, and R. B. Fair, “Mechanical property measurement of thin-film gold using thermally actuated bimetallic cantilever beams,” *Model. Simulation Microsyst.*, pp. 410-413, 2001.

[4.11] Judy, M.W.; Cho, Y.-H.; Howe, R.T.; Pisano, A.P., “Self-adjusting microstructures (SAMS),” *Micro Electro Mechanical Systems, 1991, MEMS '91, IEEE Proceeding,. 'An Investigation of Micro Structures, Sensors, Actuators, Machines and Robots'*. Page(s):51 – 56, 30 Jan.-2 Feb. 1991.

[4.12] J. Wang, Y. Cai and J.-C. Chiao, “A Coplanar Waveguide Line based on Polymer Substrate,” *2005 TexMEMS, The VII International Conference on Micro Electro Mechanical Systems*, El Paso, TX, USA and Ciudad Juárez, Mexico. Sept. 21-22, 2005.

[4.13] J. Wang, Y. Cai, T. Ativanichayaphong, M. Chiao and J.-C. Chiao, “Fabrication Techniques for RF Transmission Lines on Polymer Substrates,” *SPIE Microelectronics, MEMS, and Nanotechnology Symposium, Microelectronics, Design, Technology, and Packaging Conference*, Brisbane Australia, Dec. 11-14, 2005.

[4.14] P.B. Chinoy and J. Tajadod, “Processing and microwave characterization of multilevel interconnects using benzocyclobutene dielectric,” *IEEE Transactions on Components, Hybrids, and Manufacturing Technology*, Vol. 16, Issue 7, pp.714-719, Nov. 1993.

[4.15] A.L.S. Loke, J.T. Wetzel, Changsup Ryu, Won-Jun Lee, and S.S. Wong, “Copper drift in low-K polymer dielectrics for ULSI metallization,” *1998 Symposium of VLSI Technology*, pp.26 -27, June 1998.

[4.16] Zhimin Yao and Noel C. MacDonald, “Single crystal silicon supported thin film micromirrors for optical applications,” Optical Engineering, Volume 36, Issue 5, pp. 1408-1413, May 1997.

[4.17] K.Grenier, V.Lubecke, F.Bouchriha, L.Rabbia, D.Dubuc, P.Pons, R.Plana “Polymers in RF and millimeterwave applications,” *1st Symposium on Microtechnologies for the New Millennium 2003, Proceedings of SPIE 'Smart Sensors, Actuators, and MEMS'*, vol. 5116, pp. 502-513, May 19-21, 2003.

[4.18] T.Q. Ho, Y. Shih, “Spectral-domain analysis of E-plane waveguide to microstrip transitions,” *IEEE Trans. Microwave Theory Tech.*, Volume 37, pp. 388-392, Feb. 1989.

[4.19] W. Simon, M. Werthen, I. Wolff, “A novel coplanar transmission line to rectangular waveguide,” *IEEE MTT-S International Microwave Symposium Digest*, vol. 1, pp. 257-260, June 7-12, 1998.

[4.20] Ponchak, G.E.; Simons, R.N., “A new rectangular waveguide to coplanar waveguide transition,” *IEEE MTT-S International Microwave Symposium Digest, 1990,* vol.1, Page(s):491 – 492, 8-10 May, 1990.

[5.1] Rizk, J.B.; Rebeiz, G.M.; “Digital-type RF MEMS switched capacitors,” *IEEE MTT-S International Microwave Symposium Digest, 2002*, Volume 2, Page(s):1217 – 1220, 2-7 June 2002.

[5.2] Deve, N.; Kouki, A.B.; Nerguizian, V.; “A compact size reconfigurable 1-3 GHz impedance tuner suitable for RF MEMS applications,” *The 16th International Conference on Microelectronics, 2004. ICM 2004 Proceedings*. Page(s):101 – 104, 6-8 Dec. 2004.

[5.3] Goldsmith, C.L.; Zhimin Yao; Eshelman, S.; Denniston, D.; "Performance of low-loss RF MEMS capacitive switches," *IEEE Microwave and Guided Wave Letters, [see also IEEE Microwave and Wireless Components Letters]*, Volume 8, Issue 8, Page(s):269 – 271, Aug. 1998.

[5.4] Hayden, J.S.; Rebeiz, G.M.; "Low-loss cascadable MEMS distributed X-band phase shifters," *IEEE Microwave and Guided Wave Letters, [see also IEEE Microwave and Wireless Components Letters]* Volume 10, Issue 4, Page(s):142 – 144, April 2000.

BIOGRAPHICAL INFORMATION

The author was born in Chengdu, Sichuan Province, China, in 1974. He received his B.S. degree from Automation Department, Tsinghua University, Beijing, China in 1998. He obtained his M.S. degree from the same department and same school, in 2001. He got his Ph.D. degree from The University of Texas at Arlington in 2006 in Electrical Engineering from Electrical Engineering Department. His current research interests are focused on Microsystems, including micromachining, MEMS, millimeter-wave imaging, and sensing systems.